A Solid-State ^{11}B NMR and Computational Study of Boron Electric Field Gradient and Chemical Shift Tensors in Boronic Acids and Boronic Esters

Joseph W. E. Weiss

A thesis submitted to the Faculty of Graduate and Postdoctoral Studies in partial fulfillment of the requirements for the degree of

Master of Science

at the Ottawa-Carleton Chemistry Institute

Department of Chemistry, University of Ottawa

uOttawa

L'Université canadienne
Canada's university

Université d'Ottawa · University of Ottawa

Candidate Supervisor

Joseph W. E. Weiss Professor D. L. Bryce

Acknowledgements

I can now take a deep breath and prepare myself for departure from the womb that is graduate school! There are many people at the University of Ottawa who made my experience here a wonderful one, and who contributed greatly to my learning experience and the development of my career. Becky Chapman would always have helpful videos to show us in the office such as: a cat eating spaghetti, cats on a treadmill, or “double rainbow guy”. She was always extremely helpful and would assist me with any questions I ever had for her. But perhaps most importantly, she introduced me to Tuckers Marketplace. Cory Widdifield, lab super-genius, is the Chuck Norris of NMR. He introduced me to some of the world’s most extraordinary beverages such as Samichlaus and scotch. Cory could figure out any complicated problems I ever had, and was always able to answer any question I ever had for him; especially if it was related to wrestling or baseball. Dr. Andy Lo, Bryce Nation’s post-doc, I will miss all of the random Chinese ring tones that played throughout the day on your cell phone. Congrats on your new job! It’s about time. James Hooper, Woo lab drop-in, it was fun having you as an honorary lab member. Congrats on submitting before me. Titel Jurca, who I’ve known since the beginning of undergrad, thanks for being my personal motivator. I will miss the daily lunches and coffee breaks. I wish you continued success so that you can earn enough income to expand your Cadillac collection, and eventually retire to Del Boca Vista, Florida. Dr. Glenn Facey, manager of the NMR facility, never ceased to make fun of me on Facebook whenever he had the opportunity. Although I must say, he’s definitely the best NMR facility manager out there. Anytime something went wrong on the spectrometer, he was there right away to fix it, and solved every problem I ever went to

him with. Thanks Glenn. I would also like to extend a big thank you to Victor Terskikh and Eric Ye from the National Ultrahigh-Field NMR Facility for Solids. You were both incredibly helpful and assisted me greatly in my research. I am honored to have been given the opportunity to work at such an impressive facility. Thank you to Dr. Ilia Korobkov for acquiring the crystal structures of many of my boron-containing compounds. Even when my crystals were too small and I wasn't sure if they were suitable for X-ray analysis, Ilia was always able to mount any crystal! Dr. Kenneth Maly was extremely instrumental in the production of this thesis. His lab synthesized all of the compounds analyzed in Chapter 4, and he always made himself available for the many useful discussions we had regarding this boron study. Thanks Ken for offering guidance and advice regarding "next-steps" on the progression of this project.

Of course I must also thank my family for all of their support. I consider myself lucky to live in the same city as all of my immediate family. Their continuing support and weekly dinners were important to my development and delicious, respectively. Thanks to my mom for being the one person who always stood behind me and supported me in absolutely everything I've done, and every decision I've made without question. You've had a huge impact on me and have been instrumental in me ending up where I am now. My dad also encouraged me along the way and he always had my best interest in mind with any advice he's ever given me. He's also the reason I began to work hard and realize my potential in University. While I tried to figure out what to do with my life, Tom was on the front line of having to put up with all my indecision and living with me while I was undoubtedly overly-stressed and difficult to live with. Thanks for being completely supportive, always being there for me, and teaching me important Mandarin phrases. Of

course the remainder of my extended family was also supportive and encouraging and I love all of you too. Our family dinners are certainly entertaining and I love every minute of them (especially at Montana's). We are proof that what you see in Seinfeld and Curb Your Enthusiasm happens in real life.

Most importantly, thanks to my supervisor Dr. David Bryce for taking me on as a master's student and being such an amazing professor to work with. I never once saw him get angry or lose his cool. No matter what the situation, he is always constructive and positive. He is quick to praise when you do well, and remains encouraging when things aren't going according to plan. He is always there to offer guidance whenever it is needed or wanted. It is extremely helpful to have a supervisor who replies to your emails in less than 90 seconds. He encourages you to work hard and get excellent results, but never forgets to also have fun and take his students out for a pint.

Finally, thanks to the Natural Sciences and Engineering Research Council of Canada and the University of Ottawa for their financial support and facilitating all of my research.

Contents

Acknowledgements I

Table of Contents IV

List of Figures V

List of Tables IX

List of Abbreviations XI

Abstract 1

Chapter 1 Introduction

1.1 Conventions and Background 3
1.2 ^{11}B Solid-State NMR 15
1.3 Objectives and Scope 20

Chapter 2 Relating ^{11}B NMR Parameters to Molecular and Electronic Structure

2.1 Introduction 22
2.2 Results and Discussion 25
2.3 Experimental 72

Chapter 3 Signal Enhancement Using Double Frequency Sweeps and the Quadrupolar Carr-Purcell-Meiboom-Gill Pulse Sequence

3.1 Introduction 76
3.2 Results and Discussion 80
3.3 Experimental 89

Chapter 4 Limitations of Relating ^{11}B NMR Parameters to Structure

4.1 Introduction 91
4.2 Results and Discussion 97
4.3 Experimental 139

Chapter 5 Conclusion 142

Appendices 148

References 173

List of Figures

Figure 1.1: Illustration of the Zeeman interaction for a spin 3/2 system 4

Figure 1.2: Illustration of the lineshapes a spin ½ nucleus with varying skew values 9

Figure 1.3: Illustration of second-order CT lineshapes for a half-integer spin quadrupolar nucleus with varying asymmetry parameter values.....12

Figure 1.4: Euler angles relating one coordinate system, the EFG PAS to another coordinate system, the CS PAS 13

Figure 1.5: Magic angle spinning depicting a rotor which is rotating at an angle of 54.74^{o} relative to the magnetic field 17

Figure 2.1: Structures of the boronic acids (**1** to **5**) and boronic esters (**6** to **10**) used in this study.....24

Figure 2.2: Solid-state boron-11 NMR spectroscopy of **8** 26

Figure 2.3: Solid-state boron-11 NMR spectroscopy of **1** 28

Figure 2.4: Solid-state boron-11 NMR spectroscopy of **2** 29

Figure 2.5: Solid-state boron-11 NMR spectroscopy of **3** 31

Figure 2.6: Solid-state boron-11 NMR spectroscopy of **4** 32

Figure 2.7: Solid-state boron-11 NMR spectroscopy of **5** 33

Figure 2.8: Solid-state boron-11 NMR spectroscopy of **6** 34

Figure 2.9: Solid-state boron-11 NMR spectroscopy of **7** 36

Figure 2.10: Solid-state boron-11 NMR spectroscopy of **9** 37

Figure 2.11: Solid-state boron-11 NMR spectroscopy of **10** 38

Figure 2.12: Calculated and experimental boron C_Q for boronic acids and boronic esters studied **1** – **10**.....39

Figure 2.13: Calculated and experimental boron **Ω** values for boronic acids and boronic esters studied **1** – **10**.....40

Figure 2.14: Solid-state boron-11 NMR spectroscopy of **3** and **8**, showing the effects of CSA on lineshape.....41

Figure 2.15: Solid-state boron-11 NMR spectroscopy of **1**, showing the effects of CSA on lineshape 42

Figure 2.16: Solid-state boron-11 NMR spectroscopy of **2**, showing the effects of CSA on lineshape 42

Figure 2.17: Solid-state boron-11 NMR spectroscopy of **4**, showing the effects of CSA on lineshape 43

Figure 2.18: Solid-state boron-11 NMR spectroscopy of **5**, showing the effects of CSA on lineshape 44

Figure 2.19: Solid-state boron-11 NMR spectroscopy of **6**, showing the effects of CSA on lineshape 44

Figure 2.20: Solid-state boron-11 NMR spectroscopy of **7**, showing the effects of CSA on lineshape 45

Figure 2.21: Solid-state boron-11 NMR spectroscopy of **9**, showing the effects of CSA on lineshape 46

Figure 2.22: Solid-state boron-11 NMR spectroscopy of **10**, showing the effects of CSA on lineshape 46

Figure 2.23: Graphical representation of experimental Ω values for the compounds being studied (**1** – **10**) and different borate and borane compounds.....47

Figure 2.24: Correlation between the calculated GGA revPBE and experimental span values and correlation between calculated total isotropic shielding and experimental isotropic chemical shift values measured in the solid state for each boronic acid and ester studied (**1** – **10**).....55

Figure 2.25: Correlation between the calculated Ω values and ϕ_{CCBO} for monomeric and dimeric forms of phenylboronic acid.....57

Figure 2.26: Occupied orbital 33 (HOMO -7) and virtual orbital 65 (LUMO +24) for compound **6** 61

Figure 2.27: Correlation between the GGA revPBE calculated total magnetic shielding tensor components, total isotropic σ_{para} tensor components, and ϕ_{CCBO} for phenylboronic acid.....65

Figure 2.28: A molecular diagram showing the structure of compound **7** as well as the orientations of the chemical shift tensors. δ_{33} and δ_{22} are both in the plane of the page, and δ_{11} is perpendicular to the plane of the page. 66

Figure 3.1: A graphical illustration depicting the QCPMG pulse sequence 76

Figure 3.2: A graphical illustration of a double frequency sweep in the time domain....77

Figure 3.3: An illustration of how signal enhancement is achieved using DFS....78

Figure 3.4: An ^{87}Rb QCPMG SSNMR spectrum of $RbClO_4$....79

Figure 3.5: Solid-state boron-11 QCPMG NMR spectroscopy of **9** and **3** 80

Figure 3.6: Solid-state boron-11 QCPMG NMR spectroscopy of **1** 81

Figure 3.7: Solid-state boron-11 QCPMG NMR spectroscopy of **2** 82

Figure 3.8: Solid-state boron-11 QCPMG NMR spectroscopy of **5** 84

Figure 3.9: Solid-state boron-11 QCPMG NMR spectroscopy of **8** 85

Figure 3.10: Solid-state boron-11 QCPMG NMR spectroscopy of **10** 86

Figure 4.1: Structures of the boronic acids (**11** to **16**) and boronic acid catechol cyclic esters (**17** to **25**) used in this study 96

Figure 4.2: Solid-state boron-11 NMR spectroscopy of **11** 99

Figure 4.3: Solid-state boron-11 NMR spectroscopy of **12** 100

Figure 4.4: Solid-state boron-11 NMR spectroscopy of **13** 101

Figure 4.5: Solid-state boron-11 NMR spectroscopy of **14** 102

Figure 4.6: Solid-state boron-11 NMR spectroscopy of **15** 104

Figure 4.7: Solid-state boron-11 NMR spectroscopy of **16** 105

Figure 4.8: Solid-state boron-11 NMR spectroscopy of **17** 106

Figure 4.9: Solid-state boron-11 NMR spectroscopy of **18** 107

Figure 4.10: Solid-state boron-11 NMR spectroscopy of **19** 109

Figure 4.11: Solid-state boron-11 NMR spectroscopy of **20** 110

Figure 4.12: Solid-state boron-11 NMR spectroscopy of **21** 111

Figure 4.13: Solid-state boron-11 NMR spectroscopy of **22** 112

Figure 4.14: Solid-state boron-11 NMR spectroscopy of **23** 114

Figure 4.15: Solid-state boron-11 NMR spectroscopy of **24** 115

Figure 4.16: Solid-state boron-11 NMR spectroscopy of **25** 116

Figure 4.17: A plot of experimental C_Q values versus the type of compound being studied: boronic acids and boronic acid catechol cyclic esters 117

Figure 4.18: Solid-state boron-11 NMR spectroscopy of **16** before and after recrystallization. 120

Figure 4.19: ORTEP diagram depicting the crystal structure for compound **11** 121

Figure 4.20: ORTEP diagram depicting the crystal structure for compound **12** 121

Figure 4.21: ORTEP diagram depicting the crystal structure for compound **21** 122

Figure 4.22: ORTEP diagram depicting the crystal structure for compound **22** 122

Figure 4.23: Correlation between the calculated GGA revPBE and experimental total isotropic shielding and isotropic chemical shift values measured in the solid state for each boronic acid and boronic acid catechol cyclic ester studied (**11** – **25**) 130

Figure 4.24: Correlation between the calculated GGA revPBE and experimental span values measured in the solid state for each boronic acid and boronic acid catechol cyclic ester studied (**11** – **25**) 131

Figure 4.25: Correlation between the calculated Ω values and ϕ_{CCBO} for compounds **11** – **25** 133

Figure 4.26: Structures of the boron compounds with varying ring systems (**26** – **36**) used in this study 135

List of Tables

Table 2.1: Experimental ^{11}B EFG and CS tensor parameters for compounds **1** to **10** 27

Table 2.2: Calculated EFG and CS tensor parameters for compounds **1** to **10** (6-311+G* basis set on all elements for DFT and RHF calculations) 49

Table 2.3: Calculated magnetic shielding tensor skew and Euler angles for compounds **1** to **10** (6-311+G* basis set on all elements for DFT and RHF calculations) 50

Table 2.4: Calculated ^{11}B EFG parameters and CSA for compounds **1** to **10** (6-31G* basis set on all first and second row elements, and the aug-cc-pVTZ basis set on all heavier elements for DFT and RHF calculations) 52

Table 2.5: Calculated magnetic shielding tensor skew and Euler angles for compounds **1** to **10** (6-31G* basis set on all first and second row elements, and the aug-cc-pVTZ basis set on all heavier elements for DFT and RHF calculations) 53

Table 2.6: Calculated magnetic shielding tensor components and Ω for phenylboronic acid monomer and dimer as the dihedral is varied from 0 to 90º 59

Table 2.7: Calculated magnetic shielding tensor components with the largest contribution to total isotropic σ_{para} for a given set of occupied and virtual MOs for compounds **1** to **10** 63

Table 2.8: Calculated magnetic shielding tensor components with the largest contribution to total isotropic σ_{para} for a given set of occupied and virtual MOs for phenylboronic acid 64

Table 2.9: Calculated magnetic shielding tensor components for compounds **1** to **10** 67

Table 2.10: Calculated magnetic shielding tensor components for phenylboronic acid 68

Table 2.11: Calculated Ω and magnetic shielding tensor components for a series of steric, electron donating, and electron withdrawing groups substituted on phenylboronic acid 70

Table 4.1: Experimental ^{11}B EFG and CS tensor parameters for compounds **11** to **25**. 98

Table 4.2: Calculated EFG and CS tensor parameters for compounds **11** to **25** (DFT calculations using the 6-311+G* basis set on all elements).....125

Table 4.3: Calculated EFG and CS tensor parameters for compounds **11** to **25** (ADF calculations using the TZP basis set on all elements) 126

Table 4.4: Calculated EFG and CS tensor parameters for compounds **11** to **25** (ADF calculations using the TZ2P basis set on all elements and the VWN LDA) 128

Table 4.5: Calculated EFG and CS tensor parameters for compounds **26** to **36**.....137

List of Abbreviations

ADF	Amsterdam density functional
B3LYP	Becke 3-parameter (exchange), Lee, Yang, and Parr (a hybrid density functional)
COF	covalent organic framework
CS	chemical shift
CSA	chemical shift anisotropy
CT	central transition
DFS	double frequency sweep
EFG	electric field gradient
EM	electromagnetic
FID	free induction decay
GGA	generalized gradient approximation
HOMO	highest occupied molecular orbital
LDA	local density approximation
LUMO	lowest unoccupied molecular orbital
MAS	magic angle spinning
MOF	metal organic framework
MQMAS	multiple quantum magic angle spinning
N.A.	natural abundance
NMR	nuclear magnetic resonance
ORTEP	Oak Ridge thermal ellipsoid plot program
PAS	principal axis system

QCPMG	quadrupolar Carr-Purcell-Meiboom-Gill
QI	quadrupolar interaction
revPBE	revised Perdew-Burke-Ernzerhof (a density functional)
RF	radio frequency
RHF	restricted Hartree Fock
SSNMR	solid-state nuclear magnetic resonance
ST	satellite transition
THF	tetrahydrofuran
VT	variable temperature
VWN	Vosko-Wilk-Nusair

Abstract

The results of a solid-state ^{11}B NMR study of a series of boronic acids, boronic esters, and boronic acid catechol cyclic esters with aromatic substituents are reported in this thesis. Boron-11 electric field gradient (EFG) and chemical shift (CS) tensors obtained from analyses of spectra acquired in magnetic fields of 9.4 T and 21.1 T are demonstrated to be useful for gaining insight into the molecular and electronic structure about the boron nucleus. Data collected at 21.1 T for the boronic acid and boronic ester compounds in Chapter 2 clearly show the effects of boron chemical shift anisotropy (CSA), with tensor spans (Ω) on the order of 10 to 40 ppm (Chapter 2). For the compounds studied in Chapter 3, signal enhancements of up to 2.95 were achieved with a DFS-modified QCPMG pulse sequence. To better understand the relationship between the NMR interaction tensors and the local structure, calculations of the ^{11}B EFG and magnetic shielding tensors for these compounds were conducted. The best agreement was found between experimental results and those obtained from GGA-revPBE DFT calculations. For the compounds discussed in Chapter 2, a positive correlation was found between Ω and the dihedral angle (ϕ_{CCBO}), which describes the orientation of the boronic acid/ester functional group relative to an aromatic system bound to boron. The small boron CSA is discussed in terms of paramagnetic shielding contributions as well as diamagnetic shielding contributions. Although there is a region of overlap, both Ω and the ^{11}B quadrupolar coupling constants tend to be larger for boronic acids than for the esters. In the case of boronic acids and boronic acid catechol cyclic esters in Chapter 4, the ^{11}B quadrupolar coupling constants are always larger for boronic acids than for the boronic acid catechol cyclic esters. It can be concluded that when adequate electronic

variation is present in the compounds being studied, Ω is generally the most characteristic boron NMR parameter of the molecular and electronic environment for boronic acids and esters. Importantly, these data are only reliably accessible in ultrahigh magnetic fields. The experimental Ω values result from a delicate interplay of several competing factors, including hydrogen bonding, the value of ϕ_{CCBO}, the type of aromatic ring system present, and the electron-donating or withdrawing substituents bound to the aromatic ring. When there is little electronic variation amongst the compounds, the change in the NMR parameters is negligible. Sufficient structural variations, such as those found in the ring system bound to the boron atom, are required in order to observe a substantial change in the NMR parameters.

Chapter 1

Introduction

1.1 Conventions and Background

This chapter provides a basic overview and description of the relevant interactions that are present in the observation of solid-state nuclear magnetic resonance (SSNMR), as well as the NMR parameters which can be used to simulate an acquired NMR spectrum. In the first section the Zeeman, magnetic shielding, and quadrupolar interactions are defined and discussed. These are all important interactions to which a quadrupolar nucleus is subject when exposed to an external magnetic field. These interactions will lead to unique lineshapes in the acquired SSNMR spectrum, which can typically be simulated using analytical methods, a process which allows one to quantify the above interactions using the NMR parameters discussed below. In section 1.2, ^{11}B SSNMR is discussed in some detail. Properties of the boron-11 nucleus, such as the electric quadrupole moment, the natural abundance, and the nuclear spin are given. In addition, the relevant NMR interactions present for the boron-11 nucleus are discussed. Finally, section 1.3 provides a description of the objectives and scope of this thesis.

In addition to the Zeeman interaction, the ^{11}B SSNMR spectra presented here are primarily affected by nuclear magnetic shielding (σ), the quadrupolar interaction between the quadrupole moment (eQ), and the electric field gradient (EFG) at the nucleus. The Hamiltonian operator for the ^{11}B nucleus in a magnetic field may be expressed as:[1,2]

$$\hat{H} = \hat{H}_{\mathrm{Z}} + \hat{H}_{\mathrm{Q}} + \hat{H}_{\sigma} + \hat{H}_{\mathrm{DD}} + \hat{H}_{\mathrm{J}}, \qquad (1)$$

where the first term on the right hand side of the equation represents the Zeeman interaction, the second represents the quadrupolar interaction, the third represents the

magnetic shielding interaction, the fourth represents the direct dipolar interactions, and the fifth represents the indirect nuclear spin-spin interaction.

The Zeeman interaction (Figure 1.1) is due to the interaction between a nuclear spin system and the external magnetic field. Nuclear spin (*I*) represents the total angular momentum of a given nucleus, which can be related to the nuclear magnetic moment. The magnetic moment can interact with the external environment, and in the case of NMR, the magnetic moment of the nucleus aligns along a cone about the same axis that the external magnetic field ($\mathbf{B}_0$) is oriented along while the net magnetization lies along $\mathbf{B}_0$. The total angular momentum describes the state of the nucleus, namely, the sum of the angular momenta of all the protons and neutrons contained within the nucleus, where the angular momentum is represented in vector space. Although the energy states of a quadrupolar nucleus are not degenerate in the absence of an external magnetic field due to the interaction between the quadrupole moment of the nucleus and the EFG, for simplicity, let us consider the situation where the nuclear energy states are degenerate outside the presence of an external magnetic field. The Zeeman interaction leads to the observed NMR signal. Shown below is the effect of this interaction on the spin state energies of a spin-3/2 ($I = 3/2$) quadrupolar nucleus.

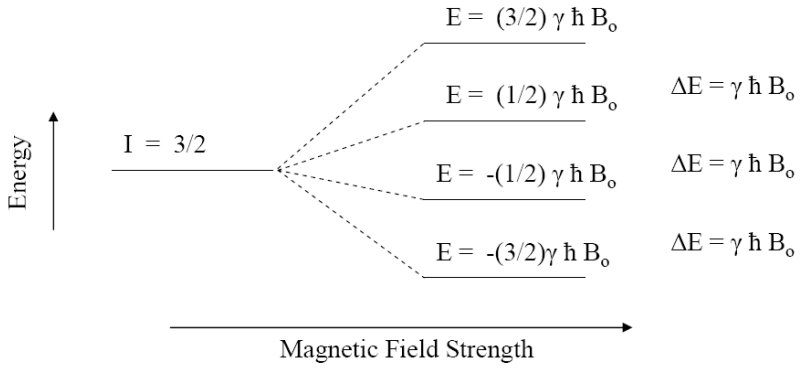

Figure 1.1: Illustration of the Zeeman interaction for a spin-3/2 system.

In the absence of an external magnetic field, all of the spin states for a given nucleus are degenerate (except when a nuclear quadrupole moment is interacting with the EFG). However, in the presence of an external magnetic field, the nuclear spin states are no longer degenerate and, if one ignores all other potential interactions, are separated by a change in energy related to the magnetogyric ratio (γ) of the nucleus, the magnitude of the external magnetic field, and Planck's constant/2π ($\hbar$). Relative to the case where the nucleus is isolated, the energy of a given spin state is simply equal to a constant (spin number for that state) multiplied by the product of γ, $\hbar$, and $\mathbf{B}_0$. Energy and frequency are related by the equation

$$\Delta E = h\nu, \tag{2}$$

and the energy difference between adjacent spin systems for a given nucleus can be expressed as a frequency,

$$\nu_{\mathrm{L}} = \frac{\gamma \mathbf{B}_0}{2\pi}, \tag{3}$$

where ν_{L} represents the nuclear Larmor frequency of the transition. To induce these transitions, electromagnetic (EM) radiation is applied to the system with energy equal to ΔE. This radiation is usually applied in the form of a radio-frequency (RF) pulse. Using eq. 3, the RF pulse is applied at the nuclear Larmor frequency. The time-domain response of the system subjected to this RF pulse can subsequently be analyzed using Fourier analysis. The bandwidth of the frequency of the pulse however, is much less than the nuclear Larmor frequency, usually on the order of tens of kHz. Long pulses can uniformly excite narrow frequency ranges, while short pulses are able to excite wider

frequency ranges. This is due to the inverse relationship between the time and frequency domains when they are related using Fourier analysis.

Consider an isolated spin 3/2 system. In the absence of an external magnetic field, while ignoring other interactions, the four allowed states of the nuclear spin system are degenerate. In bulk materials, however, a Boltzmann distribution adequately describes the population ratio between the four spin states, where the energy difference between these four states is far less than thermal energy. Hence the populations of the four states are nearly identical. However, in a magnetic field, the energy gap between these four spin states is no longer degenerate. The following equation defines the Boltzman factor relating the probability (p) of occupying an energy state (E) at a particular temperature (T):

$$\frac{p_{+1/2}}{p_{-1/2}} \propto e^{\left(\frac{-\Delta E}{kT}\right)} = e^{\left(\frac{-\gamma \mathbf{B}_0 \hbar}{kT}\right)}. \qquad (4)$$

Therefore, the population difference between the two spin states is directly proportional to the magnetogyric ratio of the nucleus and the external magnetic field strength, and inversely proportional to the temperature. The sensitivity of an NMR experiment depends on the population difference between these two energy states. Hence, sensitivity increases with increasing γ and $\mathbf{B}_0$, and decreasing T. Assuming an electronically diamagnetic material, if the populations of the two energy states were equal, there would be no net magnetization in a magnetic field. Hence, it is this population difference that leads to a net magnetization in the external magnetic field. If a static magnetic field is applied along a particular axis only, the net magnetization due to the sample builds up along the same axis as the static magnetic field. When the sample is subjected to a pulse of EM radiation which oscillates at the Larmor frequency and is directed orthogonally to

the static field, the net magnetization is diverted from the axis of the static magnetic field and towards the orthogonal plane. The spectrometer measures the time dependant magnetization in the plane. This is referred to as transverse magnetization. The change in magnetization in the transverse plane after the RF pulse is applied induces a time dependant voltage in the coil around the sample in the spectrometer. It is this signal which is referred to as the free induction decay (FID). The Fourier transform of this time dependant signal leads to an NMR spectrum in the frequency domain.

Magnetic shielding is responsible for altering the effective magnetic field experienced at the nucleus. This is due to the motions and presence of electrons surrounding the nucleus. Magnetic shielding may be generally represented by a second-rank tensor, $\boldsymbol{\sigma}$. The magnetic shielding tensor can be separated into three components: isotropic (zero-rank), symmetric (second-rank), and antisymmetric (first-rank). Diagonalization of the symmetric portion of $\boldsymbol{\sigma}$ yields the orientation of its principal axis system (PAS) relative to an external axis system. In its PAS, the three principal components (i.e., the diagonal matrix elements) of the symmetric $\boldsymbol{\sigma}$ are ordered as follows: $\sigma_{11} \leq \sigma_{22} \leq \sigma_{33}$.

The experimentally observed δ (chemical shift) may be defined in terms of magnetic shielding if a suitable shielding reference exists:

$$\delta_{ii,\text{sample}} = \frac{\sigma_{\text{iso,ref}} - \sigma_{ii,\text{ sample}}}{1 - \sigma_{\text{iso,ref}}} \approx \sigma_{\text{iso,ref}} - \sigma_{ii,\text{sample}}, \tag{5}$$

where ii = 11, 22, 33, and $\sigma_{\text{iso,ref}}$ represents the isotropic shielding value for a reference compound. Under practical application in an experiment, one measures the difference in frequency, in ppm, between a given compound and a reference sample such that:

$$\delta = \frac{\upsilon - \upsilon_{\text{ref}}}{\upsilon_{\text{ref}}} \times 10^6 . \tag{6}$$

The three principal components of the chemical shift (CS) tensor are ordered as follows: $\delta_{11} \geq \delta_{22} \geq \delta_{33}$. For both the $\boldsymbol{\sigma}$ and CS tensors, the isotropic value is the average of the three principal components. Here, the Maryland convention will be used for reporting the $\boldsymbol{\sigma}$ and CS tensor parameters.[3] The span (Ω), which measures the chemical shift anisotropy (CSA) is defined as:[3]

$$\Omega = \sigma_{33} - \sigma_{11} \approx \delta_{11} - \delta_{33} , \tag{7}$$

while the skew (κ) is defined as:[3]

$$\kappa = \frac{3(\sigma_{\text{iso}} - \sigma_{22})}{\Omega} \approx \frac{3(\delta_{22} - \delta_{\text{iso}})}{\Omega} . \tag{8}$$

The approximation made in the equation for skew is a result of the approximation that can be made in eq. 5 when defining chemical shift. The chemical shift tensor is referred to as axially symmetric if two of the principal components are equal. The figure below illustrates the effect that skew has on a simulated lineshape.

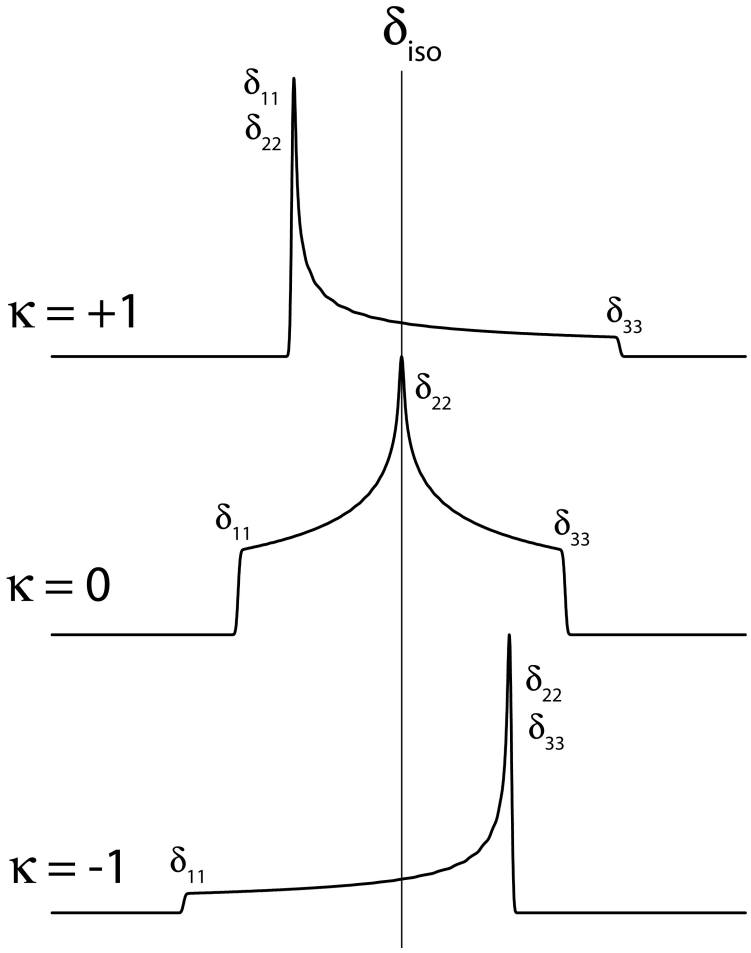

Figure 1.2: Illustration of the lineshapes a spin ½ nucleus with varying skew values. Asymmetric magnetic shielding is observed when $\kappa \neq \pm 1$.

According to Ramsey, nuclear magnetic shielding can be broken down into two contributing components: diamagnetic shielding (σ_{dia}) and paramagnetic shielding (σ_{para}).[4,5,6] Although the diamagnetic contribution depends on the electronic ground state of the molecule, the paramagnetic contribution depends on a sum over all excited states. In the past, molecular orbital theory has been successfully applied to relate electronic structure to magnetic shielding and span. Boron-11 magnetic shielding is discussed in

terms of contributions from σ_{dia} and σ_{para}.[4,5,6] The diamagnetic shielding term is defined as:

$$\sigma_{\alpha\beta}^{d} = \left(\frac{\mu_0}{4\pi}\right)\left(\frac{e^2}{2m}\right)\langle 0|\sum_{k}\frac{r^2\delta_{\alpha\beta} - r_{k\alpha}r_{k\beta}}{r_k^3}|0\rangle \quad (9)$$

where *e* is the charge of an electron, *m* is the mass of an electron, k indicates a sum over k electrons, and r_k is the position vector for electron k relative to the nucleus.

The paramagnetic shielding term may be defined as:

$$\sigma_{\alpha\beta}^{p} = -\left(\frac{\mu_0}{4\pi}\right)\left(\frac{e^2}{2m^2}\right)\times\sum_{n\neq 0}\left[\frac{\langle 0|\sum_k r_k^{-3}\hat{l}_{k\alpha}|n\rangle\langle n|\sum_k \hat{l}_{k\beta}|0\rangle + \langle 0|\sum_k \hat{l}_{k\beta}|n\rangle\langle n|\sum_k r_k^{-3}\hat{l}_{k\alpha}|0\rangle}{^1\varepsilon_n - \varepsilon_0}\right] \quad (10)$$

Where *n* indicates a sum over excited singlet states and $\hat{l}$ is the angular momentum operator. The terms in the numerator represent the degree of orbital mixing between the occupied and virtual orbitals contributing to a particular shielding component (α, β are permuted over *x*, *y*, *z*), and the term in the denominator represents the energy gap between the two wave functions involved in the mixing. Although σ_{dia} and σ_{para} are defined using a wave function basis, they are explained using MOs about the boron nucleus.

When considering a quadrupolar nucleus ($I > 1/2$), the nuclear charge distribution is non-spherical.[7] As a result of this nonspherical charge distribution, the nucleus possesses a quadrupole moment, *eQ* (eq. 11). In a prolate system, *eQ* has a positive value, whereas in an oblate system, *eQ* has a negative value. The nuclear quadrupole moment can interact with the EFG at the nucleus, which leads to the nuclear quadrupolar interaction. Unlike the nuclear magnetic shielding tensor, the EFG tensor only possesses a second-rank (symmetric) contribution. As with the shielding and shift tensors, the EFG

tensor may be diagonalized to provide the principal components of the tensor and the orientation of the PAS. The principal components of the EFG tensor are defined as follows: $|V_{33}| \geq |V_{22}| \geq |V_{11}|$. The magnitude of the EFG tensor is fully specified using two parameters. The first parameter is known as the nuclear quadrupolar coupling constant (C_Q), and is expressed as:

$$C_Q = \frac{eV_{33}Q}{h}, \tag{11}$$

where e is the fundamental charge and h is Planck's constant. Typical perturbation treatments allow the quadrupolar interaction to impose first and second-order corrections to the Zeeman states. Although there are infinite order corrections, it is often sufficiently accurate to stop at the second-order correction. It is first-order term that is averaged under magic angle spinning (MAS) conditions (*vide infra*). The second-order quadrupolar interaction often leads to lineshape broadening in SSNMR. The second parameter, known as the asymmetry of the EFG tensor is defined as:

$$\eta_Q = \frac{V_{11} - V_{22}}{V_{33}}. \tag{12}$$

The EFG tensor is axially symmetric if the asymmetry parameter is equal to zero. The figure below illustrates the effect that an asymmetric EFG has on the observed second-order NMR lineshape. MAS reduces the second-order line broadening by a factor of roughly 3.[8] This effect can also be seen in the figure below, where the MAS spectra are noticeably less broad when compared to the static spectra.

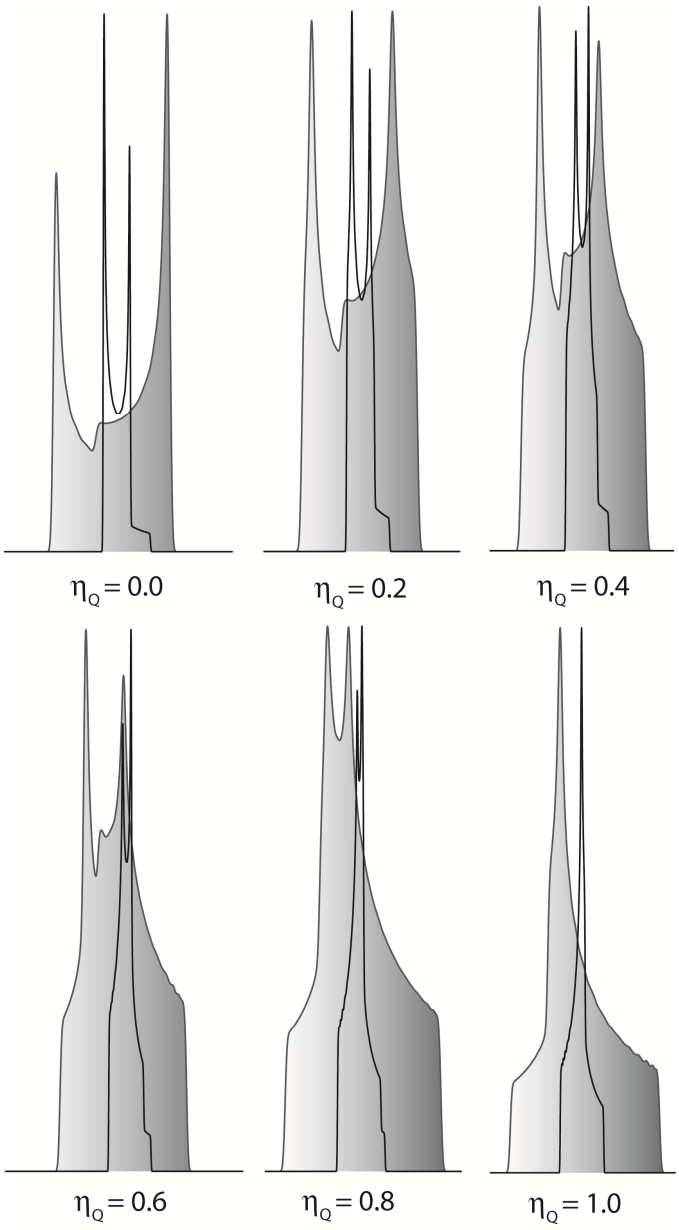

Figure 1.3: Illustration of second-order central transition (CT) lineshapes for a half-integer spin quadrupolar nucleus with varying asymmetry parameter values. Static (grey, broad) and MAS (no colour, narrow) spectra are shown.

Euler angles (α, β, and γ) are used to define the angles between two PASs, and in the case of SSNMR, they specify the relative orientation between the CS and EFG tensor

PASs.[9,10] Shown in Figure 1.4 is the EFG PAS (V_{33}, V_{22}, V_{11}), and the CS PAS (δ_{33}, δ_{22}, δ_{11}); their relative orientations are described through α, β, and γ.

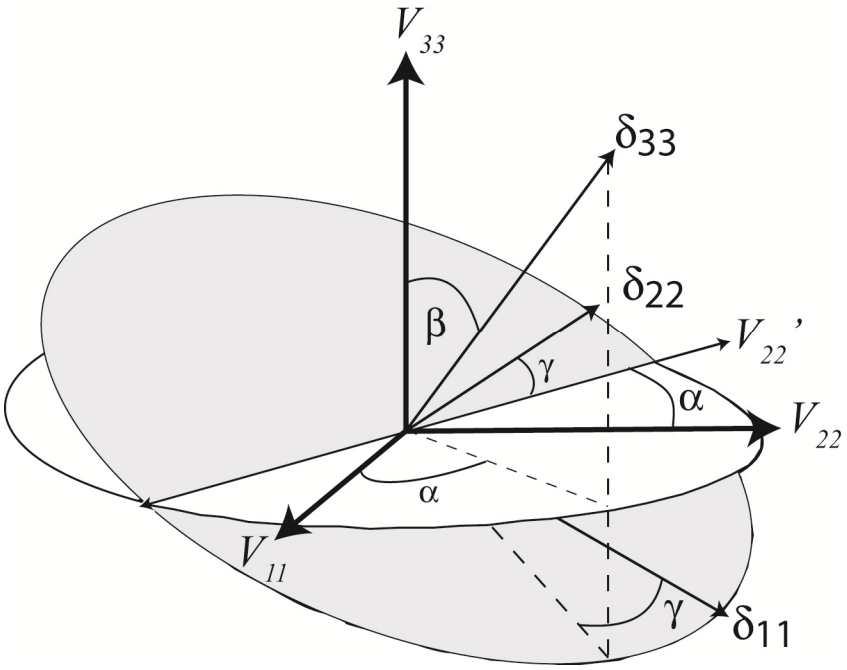

Figure 1.4: Euler angles relating one coordinate system, the EFG PAS (V_{33}, V_{22}, V_{11}) to another coordinate system, the CS PAS (δ_{33}, δ_{22}, δ_{11}).

It is useful to discuss the breadth of the central transition (CT) powder pattern due to the second-order quadrupolar interaction, for a stationary sample, ignoring CSA for the moment:[11]

$$\Delta\nu_{CT} = \frac{(25 + 22\eta_Q + \eta_Q^{\,2})}{144}\left[\frac{(3C_Q)^2}{((2I)(2I-1))^2}\right]\left[\frac{I(I+1)-\frac{3}{4}}{\nu_L}\right]. \qquad (13)$$

From eq. 13, it can be seen that the breadth of the CT ($\Delta\nu_{CT}$) is inversely proportional to the ν_L of the nucleus being studied. Since ν_L is directly proportional to $\mathbf{B}_0$ (eq. 3), the use of a larger $\mathbf{B}_0$ results in a decrease in second-order quadrupolar

broadening as well as the width of the CT in frequency units. Hence, if reduced broadening due to the quadrupolar interaction is desired, higher magnetic field strengths should be used. As CSA scales with the applied field and as broadening due to the quadrupolar interaction is reduced at higher applied fields, the effects due to CSA are potentially more easily analyzed. In the case of a spectrum which is CSA dominated, the broadening due to CSA can be quantified more precisely since quadrupolar broadening is playing a smaller role. For the proper analysis of SSNMR lineshapes where both the quadrupolar interaction (QI) and CSA are the dominant lineshape broadening mechanisms, it is important to acquire all spectra at two or more magnetic field strengths. If a spectrum from one magnetic field is simulated, it is not possible to know with absolute certainty that the extracted NMR parameters are correct. If, however, a spectrum is recorded at a different magnetic field strength and the same NMR parameters provide an appropriate fit to the data, then one can be confident that the simulations have yielded accurate NMR parameters. In addition, any discrepancies between the simulated NMR lineshapes and the experimental data at the two different magnetic field strengths can be used to help estimate experimental error.

1.2 ^{11}B Solid-State NMR Spectroscopy

Solid-state ^{11}B NMR spectroscopy can provide valuable information about structural and electronic properties in boron-containing compounds.[4,5,6] Boron has two NMR-active isotopes which possess quadrupolar nuclei, ^{10}B (I = 3; N.A. = 19.9 %; $\Xi \approx$ 10.744 %) and ^{11}B (I = 3/2; N.A. = 80.1 %; $\Xi \approx$ 32.084 %).[12] Both of these nuclides have small to moderate nuclear electric quadrupole moments, eQ ($Q(^{10}\text{B})$ = 84.59 mb; $Q(^{11}\text{B})$ = 40.59 mb).[13] The ^{11}B nucleus is more receptive to NMR studies due to its higher natural abundance, smaller quadrupole moment, and the availability of a CT (i.e., $m_I = \pm 1/2 \leftrightarrow \pm 1/2$). The CT for a spin 3/2 quadrupolar nucleus can be seen in Figure 1.1. This figure also illustrates the satellite transitions (ST) (i.e., $m_I = \pm 1/2 \leftrightarrow \pm 3/2$, for all $\Delta m_I = 1$). Signal enhancement techniques such as double frequency sweeps (DFS) can increase the population difference between the two energy states of the CT which produces more signal due to increased net magnetization. QCPMG, another signal enhancement technique, can lead to greater signal intensity in fewer scans by producing an echo train and acquiring multiple echoes per scan. These signal enhancement techniques are discussed in more detail in Chapter 3.

When NMR experiments are conducted on solutions, rapid tumbling of the solute molecules leads to an averaging of molecular orientations over the timescale of the experiment. In most cases, this leads to sharp peaks, and isotropic chemical shift data may be obtained. It is well known that such NMR experiments can be applied to help elucidate the structure of the compound being studied, provide data about the chemical environment of the nucleus being studied, provide information about dynamics such as reaction rates, or simply monitor a reaction in progress from initiation to completion.[14]

In powdered samples, the lack of rapid molecular tumbling often corresponds to a static distribution of crystallites, and hence molecular, orientations. This typically leads to NMR lineshape broadening. For ^{11}B, SSNMR spectra can provide information about both the quadrupolar interaction between the nucleus and the EFG, as well as CSA, both of which are related to the electronic and molecular environment. An advantage of SSNMR experiments using quadrupolar nuclei is that additional parameters which reflect the orientation-dependence of the NMR interactions are available and they help one to determine the local geometry and bonding environment. When considering quadrupolar nuclei, one must take the quadrupole induced shift into account. The QI shifts the centre of gravity of the lineshape, which needs to be corrected. The correction due to the quadrupole induced shift is inversely proportional to $\mathbf{B}_0$.

SSNMR experiments on powdered samples using quadrupolar probe nuclei will, almost always, lead to the observation of broad lines in the spectrum. The CT is broadened by anisotropy of second-order quadrupolar interactions. MAS, depicted below in Figure 1.5, was introduced as a means of enhancing spectral resolution.[2] Spinning a sample rapidly about the magic angle (54.74^o relative to the applied static magnetic field) leads to a time averaging of molecular orientations of the sample within the magnetic field over the period of sample rotation.[2,15,16,17,18,19,20]

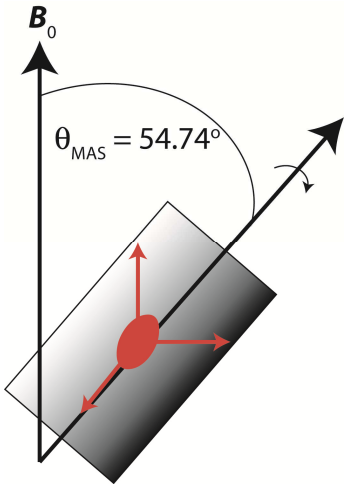

Figure 1.5: MAS depicting a rotor which is rotating at an angle of 54.74º relative to the magnetic field. This effect assists in averaging the molecular orientations of the molecules in the rotor.

MAS reduces the second-order line broadening by about 3 times.[8] If the magic angle (θ_{MAS}, as per Figure 1.5) is properly set, the first-order line broadening can be averaged for the satellite transitions in addition to suppressing the direct dipolar broadening effects. Since the central transition is usually the region of the spectrum from which physicochemical data is extracted, resolution of this region is a main focus. Second-order quadrupolar interactions affect the line shape of the central transition and act as a perturbation to the Zeeman interaction which is the dominant interaction in the high-field approximation. Setting the magic angle precisely will partially average this second-order quadrupolar interaction and potentially result in a well-resolved spectrum.

Line broadening, which manifests itself in the line patterns of a given spectrum, is due to anisotropy of second order quadrupolar interactions. Under MAS conditions, this is determined by the second and fourth-rank tensors. An n^{th} rank tensor is independent of

any specific coordinate system and is an n-dimensional array composed of numerical values or components.[21] For example, a zero-rank tensor can be represented by a single scalar value, a first-rank tensor by a vector, and a second-rank tensor by a square matrix. The magnetic shielding tensor is a 3 x 3 second-rank tensor. Spinning the sample at a precise angle with respect to the external magnetic field could individually average each of these tensors. In MAS, however, one does not spin the sample about two (or more) axes simultaneously. Thus, averaging out both the second and fourth-rank tensors and removing line broadening due to second-order anisotropy is not possible. In order to average out both second and fourth-rank tensors and fully remove the broadening due to second-order anisotropy, the following condition would have to be satisfied:[8]

$$\mathbf{P}_2(\cos\beta_2)=\mathbf{P}_4(\cos\beta_1)=0, \tag{13}$$

where $\mathbf{P}_2$ represents a second-order Legendre polynomial, $\mathbf{P}_4$ represents a fourth-order Legendre polynomial, and β represents the corresponding angles to make this condition true. Such a condition, where the second and fourth-order Legendre polynomials are being averaged to zero, is satisfied when $\beta_2 = 54.7^o$ and $\beta_1 = 30.6^o$. Magic angle spinning will average out the second-order polynomial; hence line broadening due to second-order anisotropy is reduced significantly since it is only due to the effect of the fourth-order polynomial. In MAS spectra, second-order quadrupolar interactions are still present, however, increasing the magnetic field will cause a decrease in the broadening associated with the second-order quadrupolar interaction. Although the QI and CS tensors are both second rank tensors which can be used to describe second-order QI, the second-order QI is described using second and higher-order Legendre polynomials.

Experimental characterization and interpretation of boron chemical shift and EFG tensors in a series of solid boronic acids and esters are reported. Boron-11 SSNMR experiments were performed under stationary and MAS conditions at $\mathbf{B}_0$ values of 9.40 T and 21.1 T. At 21.1 T, the influence of the CS tensor on the observed SSNMR line shapes becomes extremely important as its linewidth (in Hz) is proportional to $\mathbf{B}_0$. In addition to improving sensitivity, ultrahigh-field ($\mathbf{B}_0$ > 18.8 T) NMR spectrometers should therefore provide more precise measurements of the influence of the CS tensor on SSNMR spectra. In the case of quadrupolar nuclei, such as ^{11}B, a high magnetic field also produces narrower CT line shapes since the central transition signal broadening associated with the second-order quadrupolar coupling scales inversely with magnetic field.

Molecular orbital (MO) analyses are performed to provide insight into the relationship between the molecular and electronic structure around the boron nucleus and the ^{11}B NMR parameters. CSA is often rationalized by considering contributions to the paramagnetic shielding term, as outlined in Ramsey's theory of nuclear magnetic shielding.[4,5,6] The theory may be applied in explaining the effects of orbital-mixing-induced paramagnetic shielding on CSA. Interpretation of experimental data alongside quantum chemical calculations has the potential to provide important information relating NMR parameters and molecular and electronic environments about the boron nucleus.

1.3 Objectives and Scope

This thesis aims to relate the experimental ^{11}B SSNMR parameters for a series of boronic acids, boronic esters and boronic acid catechol cyclic esters to the molecular and electronic structures of these compounds. As an example, this can be accomplished by relating NMR parameters such as the CS tensor span (Ω) to the occupied and virtual MOs. In addition, quantum chemical calculations were carried out on all compounds. This was done to calculate the NMR parameters. These calculations can be carried out to both confirm the experimental NMR parameters, as well as to determine magnetic shielding contributions due to pairwise orbital mixing. Agreement between experimental and calculated NMR parameters provides additional evidence that the relationships noted and parameters acquired are in fact valid, and often assists in understanding the local structure. NMR signal enhancement techniques such as DFS and QCPMG were applied to these systems to test the efficacy of signal enhancement on boron-11 systems.

In Chapter 2, a series of boronic acids and esters were studied where there was large variation in the molecular and electronic structure from compound to compound. Under these conditions, there is sufficient variation in the ^{11}B NMR and therefore some of them can easily be related to the molecular structure.

In Chapter 3, ^{11}B SSNMR spectra of selected compounds from Chapter 2 were re-acquired using DFS and QCPMG pulse sequences. Signal enhancement is noted when these pulse sequences are used, and this allows for the acquisition of more signal in fewer scans, which can be useful in dilute systems.

Finally, in Chapter 4, a series of boronic acids and boronic acid catechol cyclic esters were studied where there was little variation in the molecular and electronic

structure from compound to compound. Under these conditions, there is not sufficient variation in the NMR parameters to relate them to the molecular structure. Ideally, small changes to the structure, such as the variation of a substituent on the aromatic ring system would lead to observable changes in the observed ^{11}B SSNMR spectrum. Studying these compounds proved to be a fruitful endeavor. It provides a handle as to how much electronic variation needs to be present in the system in order to have an impact on the experimentally observed ^{11}B SSNMR parameters.

SSNMR is an extremely useful technique which can be used to measure physicochemical data about a compound and to help elucidate the structure. It can provide details such as quadrupolar or magnetic shielding data which liquid NMR typically cannot. In the case of ^{11}B SSNMR, vast amounts of data can be acquired and simulated, and NMR parameters can be calculated using quantum chemical methods, to verify and help support the experimental data. Numerous signal enhancement techniques are available and can be quite useful for the characterization of dilute systems where there is a lack of boron present. Most importantly, the physicochemical data that we can extract from analyzing a spectrum can teach us about the local structure, bonding environment, and other possible interactions with nearby NMR-active nuclei. Because SSNMR is still a relatively young field (first observed experimentally in 1946),[22] there is a lot of work that remains to be done and many nuclei that have yet to be thoroughly studied. In the case of SSNMR, only recently have ultra-high field magnets been developed to allow for the study of nuclei which are otherwise too impractical to study at lower magnetic field strengths. Their observation was also facilitated by the development of signal enhancing pulse sequences such as QCPMG (*vide infra*).

Chapter 2

Relating ^{11}B NMR Parameters to Molecular and Electronic Structure

2.1 Introduction

Boronic acids and boronic esters[23] are particularly important classes of compounds that have a wide range of uses and applications. For example, they are used in catalytic additions to ketones,[24] asymmetric conjugate additions,[25] enzyme inhibition,[26,27,28,29,30,31] potent and selective serine protease inhibition,[32,33] Suzuki coupling reactions in organic synthesis,[34,35,36] materials synthesis,[37,38,39,40,41] and neutron capture therapy treatments for cancer patients.[42,43,44,45] Given the broad utility of boronic acids and esters, an understanding of the structural and electronic properties of these compounds is important.

Comprehensive ^{11}B NMR studies have been conducted on boron compounds in solution and many isotropic chemical shifts (δ_{iso}) have been reported.[14,46] The known boron chemical shift range for tricoordinate and tetracoordinate species covers approximately 210 ppm, with tetracoordinate species falling between δ_{iso} = 20 and -120 ppm, and tricoordinate species between δ_{iso} = 90 and -20 ppm with respect to $F_3B{\bullet}O(C_2H_5)_2$ at 0 ppm.[14,46] Boronic acids and esters have chemical shifts in solution ranging from about 18 to 31 ppm.[14] The chemical shifts for ^{11}B have been shown to correlate with the ligand's π–donor ability.[14] Thus, the interpretation of ^{11}B chemical shifts may provide insight into π bonding. For tricoordinate boron compounds of the series BR_3, BXR_2, BX_2R, and BX_3 (X = electron-withdrawing ligand; R = alkyl group), as one progresses from BR_3 to BX_3, the ^{11}B isotropic chemical shifts decrease systematically, which has been interpreted as being associated with increased π-electron

backbonding from X to B.[14] In addition, a sterically encumbered environment tends to cause decreased π-bonding; hence, a positive shift may be observed with increasing steric bulk about the boron.[14]

In addition to literature studies reporting isotropic information for the boron-11 nucleus in solution, ^{11}B NMR studies have been conducted on boron compounds in the solid state. The corresponding anisotropic information, such as C_Q and η_Q, was collected and reported. These solid state studies include characterization of the ^{11}B nucleus in glass,[47,48,49] glass-ceramics,[50,51] ceramics,[52,53] boron nitride in ceramics,[54,55] boron nitrides,[56] and plant cells.[57] Although ^{11}B SSNMR experiments have been carried out on a variety of compounds, there is still much characterization to be done as there is not nearly as much experimental data reported on boron-11 in the solid state as there is in liquids. Due to the fact that so much extra characterization information can be gained from SSNMR, it is beneficial to carry out experiments on relevant boron compounds.

This chapter covers a SSNMR study of the five boronic acids and five boronic esters shown below. A comprehensive discussion relating their NMR parameters to molecular and electronic structure follows.

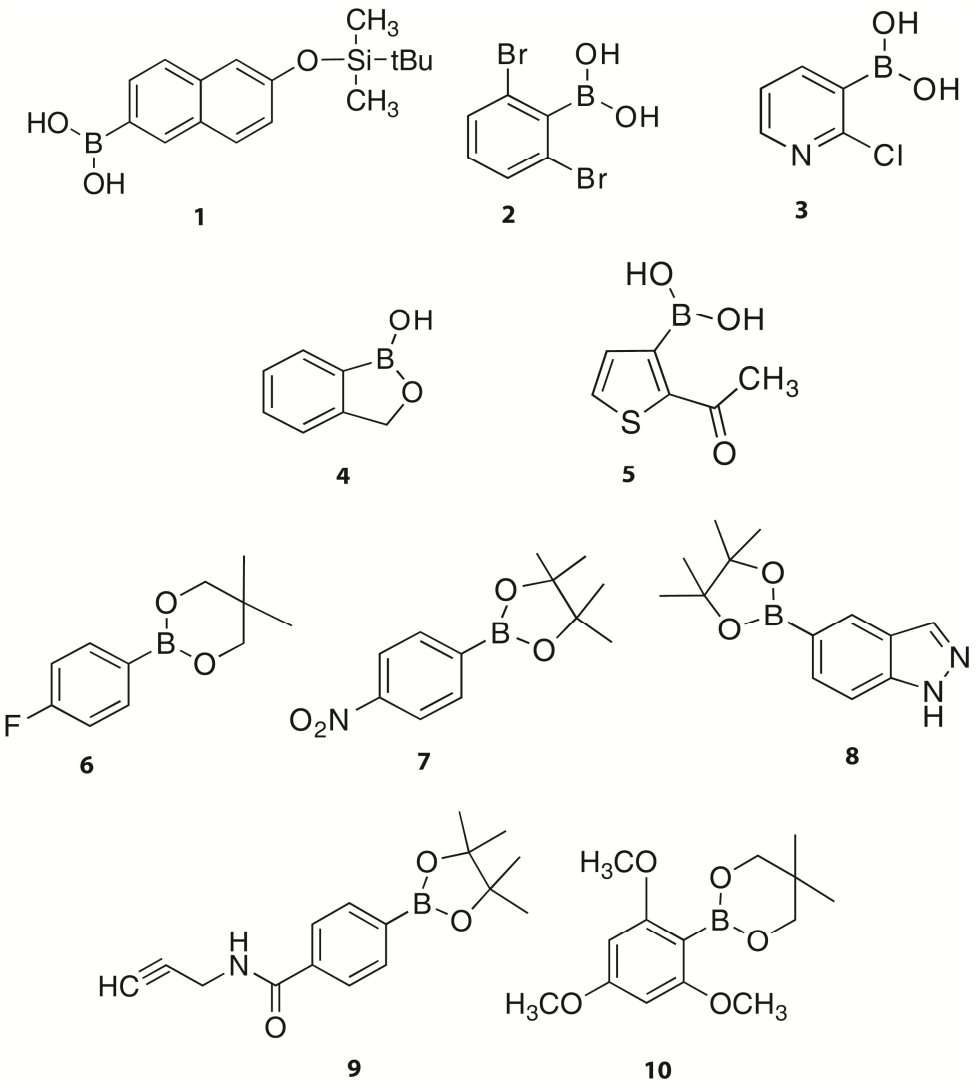

Figure 2.1: Structures of the boronic acids (**1** to **5**) and boronic esters (**6** to **10**) used in this study.

2.2 Results and Discussion

2.2.1 ^{11}B Solid-State NMR Spectroscopy

Shown in Table 2.1 are the experimental boron EFG and CS tensor values obtained via analytical simulations of the ^{11}B NMR spectra of boronic acids and esters **1** to **10**. By simultaneously fitting data at both 9.40 and 21.1 T, the C_Q, η_Q, and δ_{iso} values were determined from MAS NMR spectra. Subsequently, stationary spectra were analyzed to determine the Ω, κ, and Euler angles relating the two tensor PASs (Figures 2.2 to 2.9).

Shown in Figure 2.2 are ^{11}B SSNMR spectra of boronic ester **8** obtained at 9.40 and 21.1 T. As a representative example, these spectra and the extracted parameters are discussed in detail. The $C_Q(^{11}B)$ value obtained for **8** is 2.76 ± 0.20 MHz and η_Q = 0.59 ± 0.10. CSA is present and broadening is therefore observed in the spectrum due to both the quadrupolar interaction as well as CSA (Ω = 14 ± 2 ppm). The isotropic chemical shift of 30.3 ± 1.0 ppm falls within the expected range for a boronic ester.[14] For the data obtained at both magnetic fields, simulated spectra fit very well with the experimental data; hence, there are small experimental error values associated with the reported data (Table 2.1). The ^{11}B NMR spectra of both MAS and stationary samples are less broad at 21.1 T. This narrowing is seen for all samples in the present work, as the broadening of the CT due to the second-order quadrupolar interaction decreases with increasing $\mathbf{B}_0$. This is always the case when broadening in the spectrum is dominated by the second-order quadrupolar interaction. QCPMG spectra were also obtained and each corresponding manifold of spikelets mimics the lineshape of the stationary spectra. QCPMG was also used as a method of signal enhancement (*vide infra*).

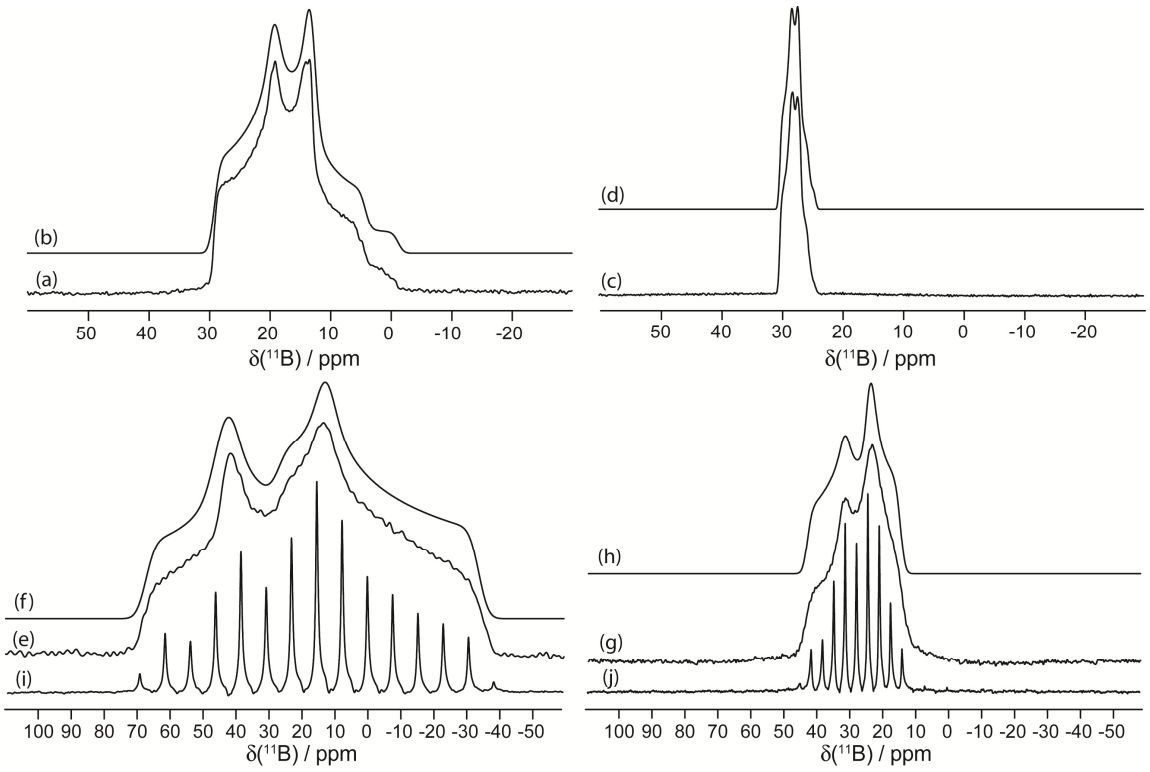

Figure 2.2: Solid-state boron-11 NMR spectroscopy of **8**. Experimental spectra of a powdered sample undergoing MAS are shown in (a) ^{11}B at 9.40 T and (c) ^{11}B at 21.1 T. Best-fit spectra were simulated using WSolids (traces (b) and (d)) using the parameters given in Table 2.1. Experimental spectra of stationary powdered samples are shown in (e) ^{11}B at 9.40 T and (g) ^{11}B at 21.1 T. Best-fit spectra were simulated using WSolids (traces (f) and (h)) using the parameters given in Table 2.1. Experimental QCPMG spectra of stationary powdered samples are shown in (i) ^{11}B at 9.40 T and (j) ^{11}B at 21.1 T.

Table 2.1: Experimental ^{11}B EFG and CS tensor parameters for compounds **1** to **10**.[a]

	Sample	C_Q / MHz	η_Q	δ_{iso} / ppm	Ω / ppm	κ	α / º	β / º	γ / º
Boronic Acids	**1**	3.29 ± 0.10	0.40 ± 0.10	29.0 ± 1.0	33 ± 11	-0.50 ± 0.20	50 ± 30	25 ± 25	40 ± 40
	2	3.10 ± 0.20	0.30 ± 0.20	30.0 ± 1.4	40 ± 10	0.40 ± 0.60	65 ± 10	0 ± 10	0 ± 10
	3	3.05 ± 0.10	0.10 ± 0.20	27.5 ± 1.0	32 ± 2	0.40 ± 0.40	0 ± 20	0 ± 10	0 ± 20
	4	2.80 ± 0.10	0.45 ± 0.10	31.0 ± 2.0	19 ± 1	-0.90 ± 0.10	40 ± 5	0 ± 5	0 ± 5
	5	2.83 ± 0.25	0.10 ± 0.30	26.0 ± 2.0	30 ± 6	0.20 ± 0.20	0 ± 60	0 ± 10	0 ± 60
Boronic Esters	**6**	2.79 ± 0.10	0.40 ± 0.15	26.5 ± 1.0	23 ± 2	0.30 ± 0.10	15 ± 75	0 ± 5	0 ± 75
	7	2.83 ± 0.20	0.51 ± 0.10	29.8 ± 1.0	12 ± 2	0.60 ± 0.10	0 ± 30	0 ± 5	0 ± 30
	8	2.76 ± 0.20	0.59 ± 0.10	30.3 ± 1.0	14 ± 2	-0.25 ± 0.10	25 ± 10	0 ± 5	0 ± 10
	9	2.66 ± 0.10	0.68 ± 0.10	30.2 ± 1.0	10 ± 2	0.40 ± 0.10	30 ± 15	0 ± 5	0 ± 15
	10	2.89 ± 0.10	0.37 ± 0.05	27.3 ± 1.0	30 ± 2	0.60 ± 0.10	103 ± 10	0 ± 5	0 ± 10
Boric Acid[b]		2.85 ± 0.05	0.40 ± 0.10	19.6 ± 0.3	-	-	-	-	-

[a]Experimental C_Q, η_Q, δ_{iso}, Ω, κ, and Euler angles for each boronic acid and ester compound studied. Chemical shifts are reported with respect to solid $NaBH_4$ at -42.06 ppm. Boric acid is included as the impurity present at 19.6 ppm in compounds **2** and **3**.

[b]The NMR parameters were included in the simulations of compounds **2** and **3** using 4% and 10% intensity relative to the main signal, respectively.

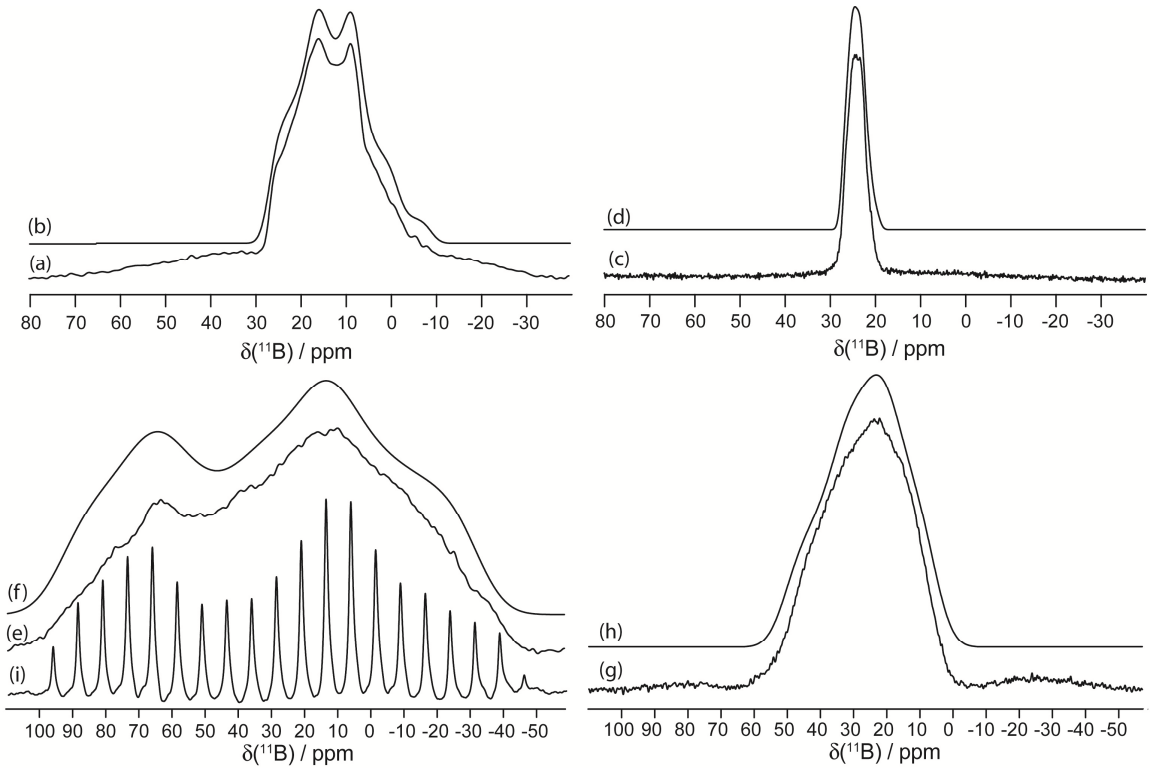

Figure 2.3: Solid-state boron-11 NMR spectroscopy of **1**. Experimental spectra of a powdered sample undergoing MAS are shown in (a) ^{11}B at 9.40 T and (c) ^{11}B at 21.1 T. Best-fit spectra were simulated using WSolids (traces (b) and (d)) using the parameters given in Table 2.1. Experimental spectra of stationary powdered samples are shown in (e) ^{11}B at 9.40 T and (g) ^{11}B at 21.1 T. Best-fit spectra were simulated using WSolids (traces (f) and (h)) using the parameters given in Table 2.1. Experimental QCPMG spectrum of a stationary powdered sample is shown in (i) ^{11}B at 9.40 T.

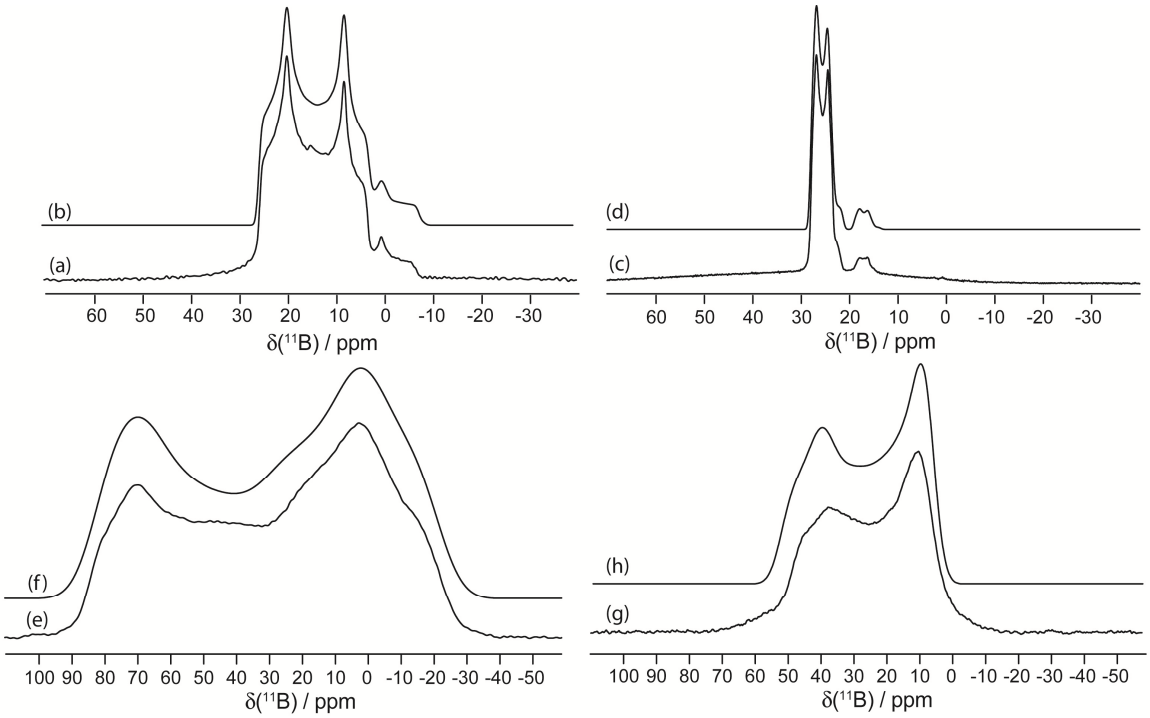

Figure 2.4: Solid-state boron-11 NMR spectroscopy of **2**. Experimental spectra of a powdered sample undergoing MAS are shown in (a) ^{11}B at 9.40 T and (c) ^{11}B at 21.1 T. Best-fit spectra were simulated using WSolids (traces (b) and (d)) using the parameters given in Table 2.1. Experimental spectra of stationary powdered samples are shown in (e) ^{11}B at 9.40 T and (g) ^{11}B at 21.1 T. Best-fit spectra were simulated using WSolids (traces (f) and (h)) using the parameters given in Table 2.1. The small peaks in spectra (a) – (d) seen at ~ 1 and 19 ppm are due to boric acid, and its spectral parameters may be found in Table 2.1.

There is very little variation in the measured $\delta_{iso}(^{11}B)$, which range from 26.0 ppm (compound **5**) to 31.0 ppm (compound **4**), i.e., only about 5 % of the total known range for tricoordinate boron. Because this range is so small, it is difficult to conclusively relate $\delta_{iso}(^{11}B)$ to any single structural or electronic feature, although there is a good correlation between the experimental isotropic chemical shift values and the calculated isotropic magnetic shielding values (*vide infra*).

In general, the directions of the eigenvectors corresponding to V_{33} and δ_{33} are coincident within experimental error, as quantified by the Euler angle β. Overall, it is found that the span is the most sensitive NMR parameter to changes in the molecular and electronic structure from compound to compound, ranging from 10 ppm (compound **9**) to 40 ppm (compound **2**); i.e., the variation in Ω (30 ppm) represents 75 % of the maximum span value (40 ppm) observed. Since the span has the largest relative variation among the NMR parameters, it is the primary focus and its relationship with the local boron electronic and molecular structure is discussed in a subsequent section.

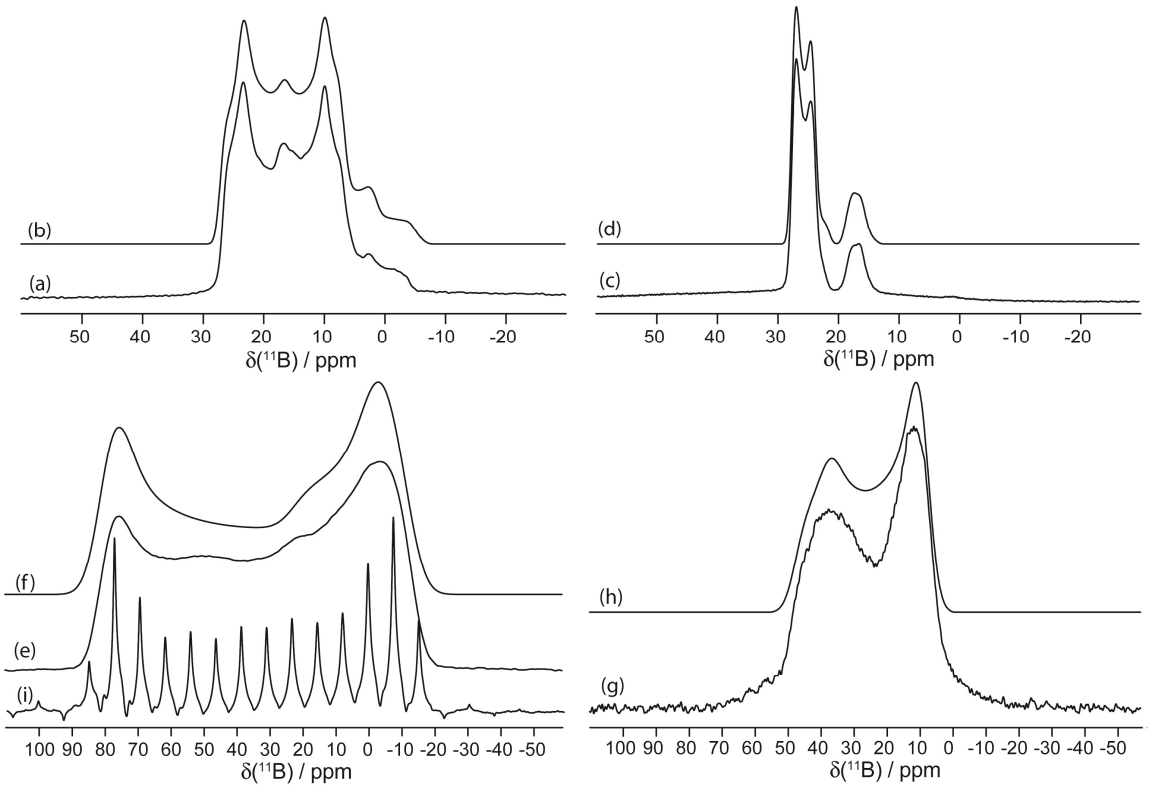

Figure 2.5: Solid-state boron-11 NMR spectroscopy of **3**. Experimental spectra of a powdered sample undergoing MAS are shown in (a) ^{11}B at 9.40 T and (c) ^{11}B at 21.1 T. Best-fit spectra were simulated using WSolids (traces (b) and (d)) using the parameters given in Table 2.1. Experimental spectra of stationary powdered samples are shown in (e) ^{11}B at 9.40 T and (g) ^{11}B at 21.1 T. Best-fit spectra were simulated using WSolids (traces (f) and (h)) using the parameters given in Table 2.1. Experimental QCPMG spectrum of a stationary powdered sample is shown in (i) ^{11}B at 9.40 T. The small peaks in spectra (a) – (d) seen at ~ 1 and 19 ppm are due to boric acid, and its spectral parameters may be found in Table 2.1.

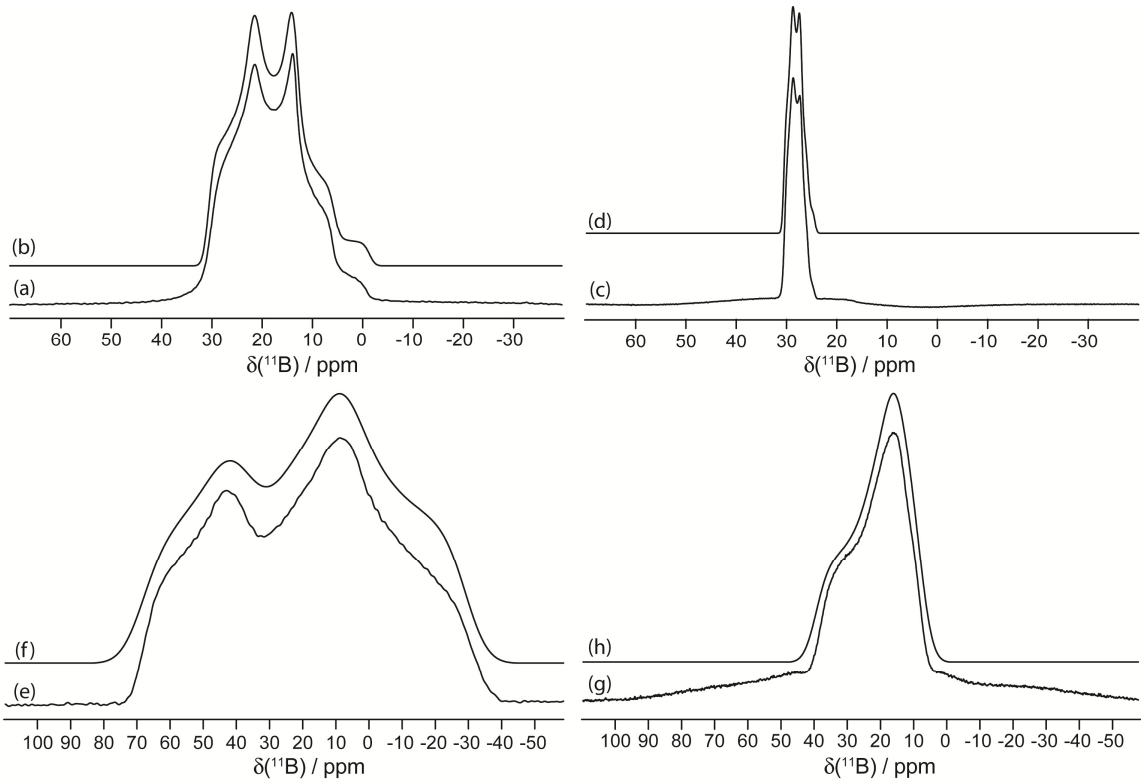

Figure 2.6: Solid-state boron-11 NMR spectroscopy of **4**. Experimental spectra of a powdered sample undergoing MAS are shown in (a) ^{11}B at 9.40 T and (c) ^{11}B at 21.1 T. Best-fit spectra were simulated using WSolids (traces (b) and (d)) using the parameters given in Table 2.1. Experimental spectra of stationary powdered samples are shown in (e) ^{11}B at 9.40 T and (g) ^{11}B at 21.1 T. Best-fit spectra were simulated using WSolids (traces (f) and (h)) using the parameters given in Table 2.1.

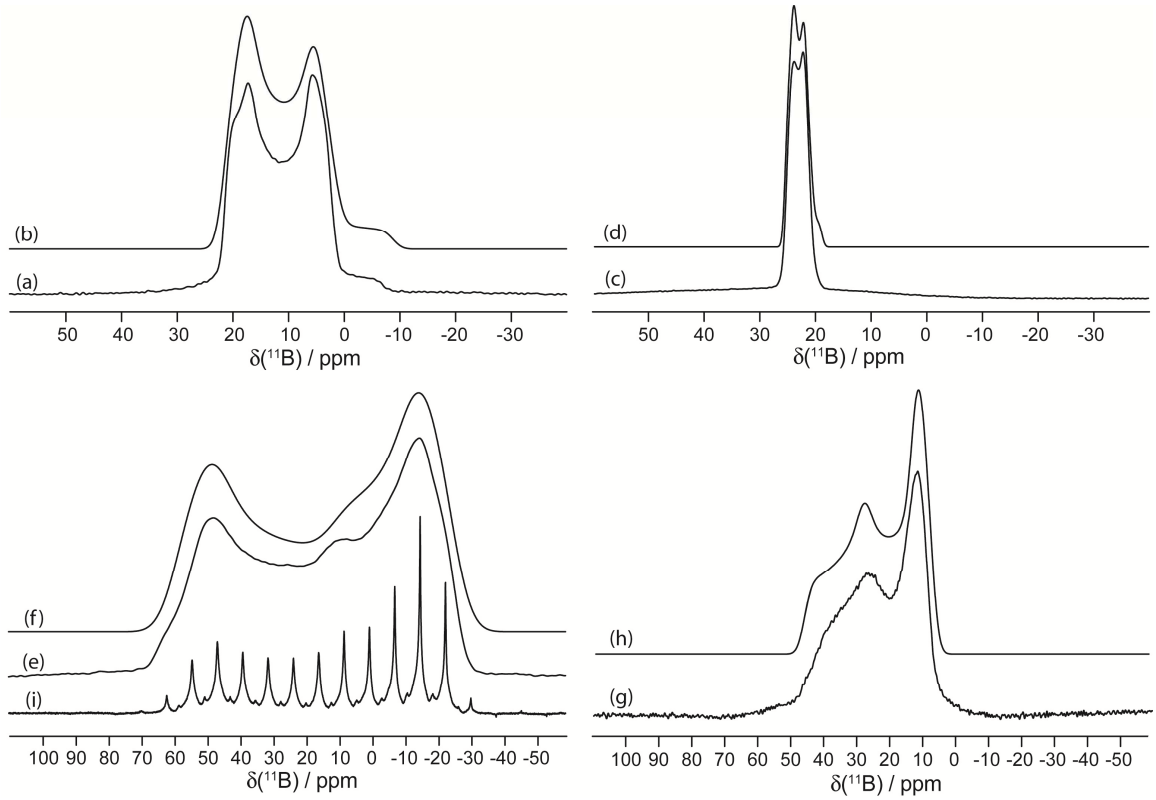

Figure 2.7: Solid-state boron-11 NMR spectroscopy of **5**. Experimental spectra of a powdered sample undergoing MAS are shown in (a) ^{11}B at 9.40 T and (c) ^{11}B at 21.1 T. Best-fit spectra were simulated using WSolids (traces (b) and (d)) using the parameters given in Table 2.1. Experimental spectra of stationary powdered samples are shown in (e) ^{11}B at 9.40 T and (g) ^{11}B at 21.1 T. Best-fit spectra were simulated using WSolids (traces (f) and (h)) using the parameters given in Table 2.1. Experimental QCPMG spectrum of a stationary powdered sample is shown in (i) ^{11}B at 9.40 T.

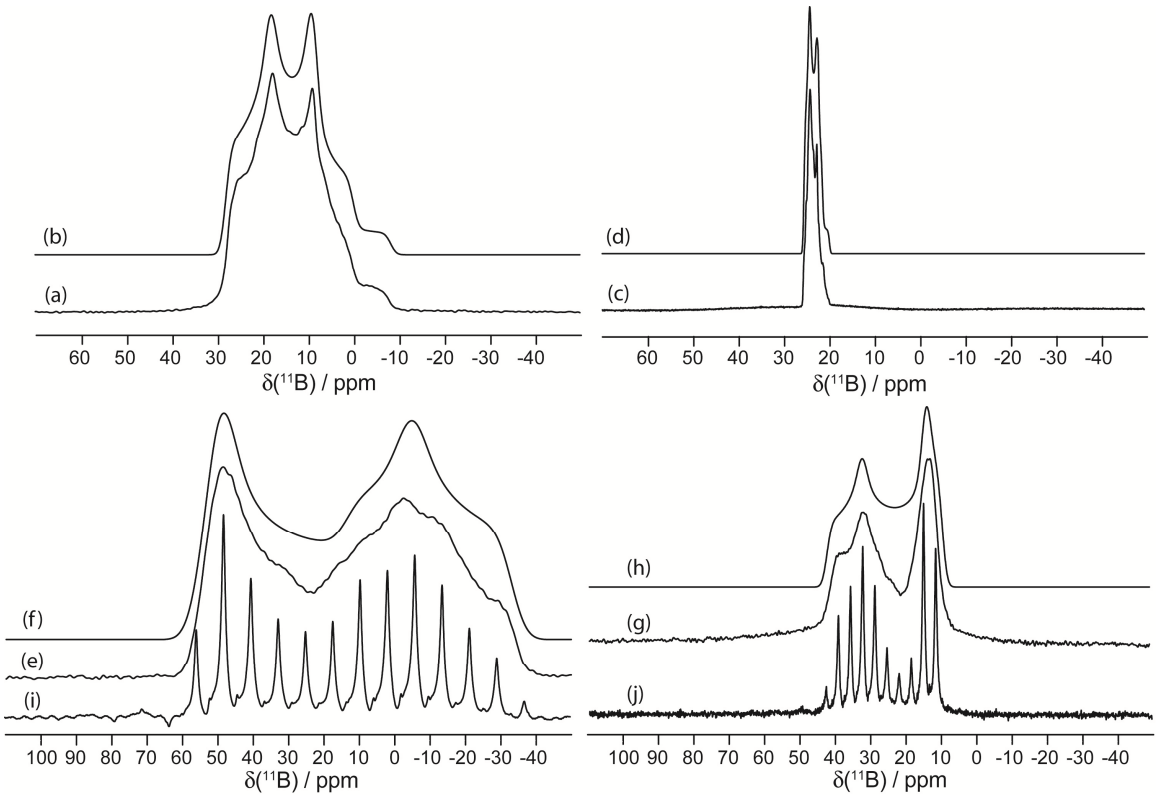

Figure 2.8: Solid-state boron-11 NMR spectroscopy of **6**. Experimental spectra of a powdered sample undergoing MAS are shown in (a) ^{11}B at 9.40 T and (c) ^{11}B at 21.1 T. Best-fit spectra were simulated using WSolids (traces (b) and (d)) using the parameters given in Table 2.1. Experimental spectra of stationary powdered samples are shown in (e) ^{11}B at 9.40 T and (g) ^{11}B at 21.1 T. Best-fit spectra were simulated using WSolids (traces (f) and (h)) using the parameters given in Table 2.1. Experimental QCPMG spectra of stationary powdered samples are shown in (i) ^{11}B at 9.40 T and (j) ^{11}B at 21.1 T.

Depicted in Figures 2.3 to 2.6, 2.9, 2.10, and 2.11 are the ^{11}B SSNMR spectra of compounds **1** to **4**, **7**, **9**, and **10** respectively. Upon examination of the spectra it is apparent that the ^{11}B line shapes associated with the boronic acids tend to be broader than the spectra of boronic esters. This observation is associated with the fact that the boronic acids tend to have larger $C_Q(^{11}B)$ and Ω values. In Table 2.1, NMR parameters are also listed for boric acid, a known decomposition product of boronic acids.[23] This decomposition product is clearly identified in compounds **2** and **3** (Figures 2.4 and 2.5) as purchased, and is responsible for the peak with δ_{iso} = 19.6 ppm. In addition, spectra for compounds **1**, **2**, and **4** (Figures 2.3, 2.4, and 2.6) contain broad, low intensity peaks buried underneath the main signal. It is speculated that these peaks are likely due to small amounts of an unknown impurity, decomposition product present in the sample, or possibly the result of less effective suppression of the signal due to boron nitride inside the stator.

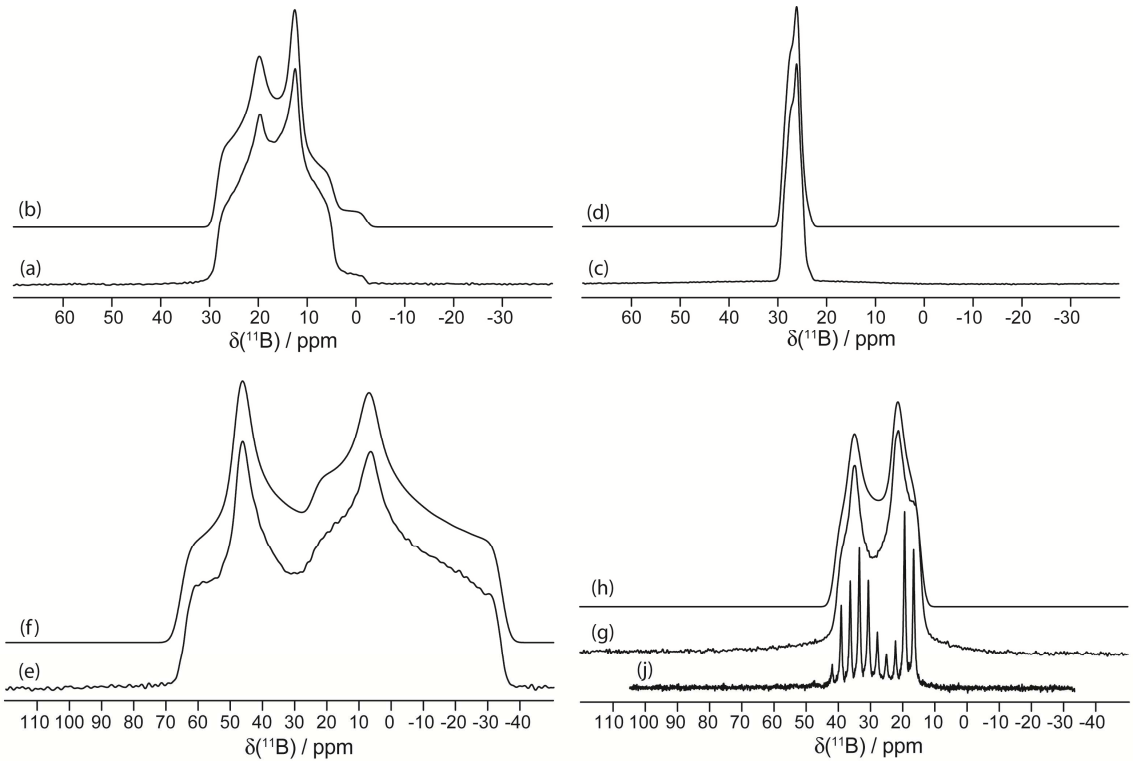

Figure 2.9: Solid-state boron-11 NMR spectroscopy of **7**. Experimental spectra of a powdered sample undergoing MAS are shown in (a) ^{11}B at 9.40 T and (c) ^{11}B at 21.1 T. Best-fit spectra were simulated using WSolids (traces (b) and (d)) using the parameters given in Table 2.1. Experimental spectra of stationary powdered samples are shown in (e) ^{11}B at 9.40 T and (g) ^{11}B at 21.1 T. Best-fit spectra were simulated using WSolids (traces (f) and (h)) using the parameters given in Table 2.1. Experimental QCPMG spectrum of a stationary powdered sample is shown in (j) ^{11}B at 21.1 T.

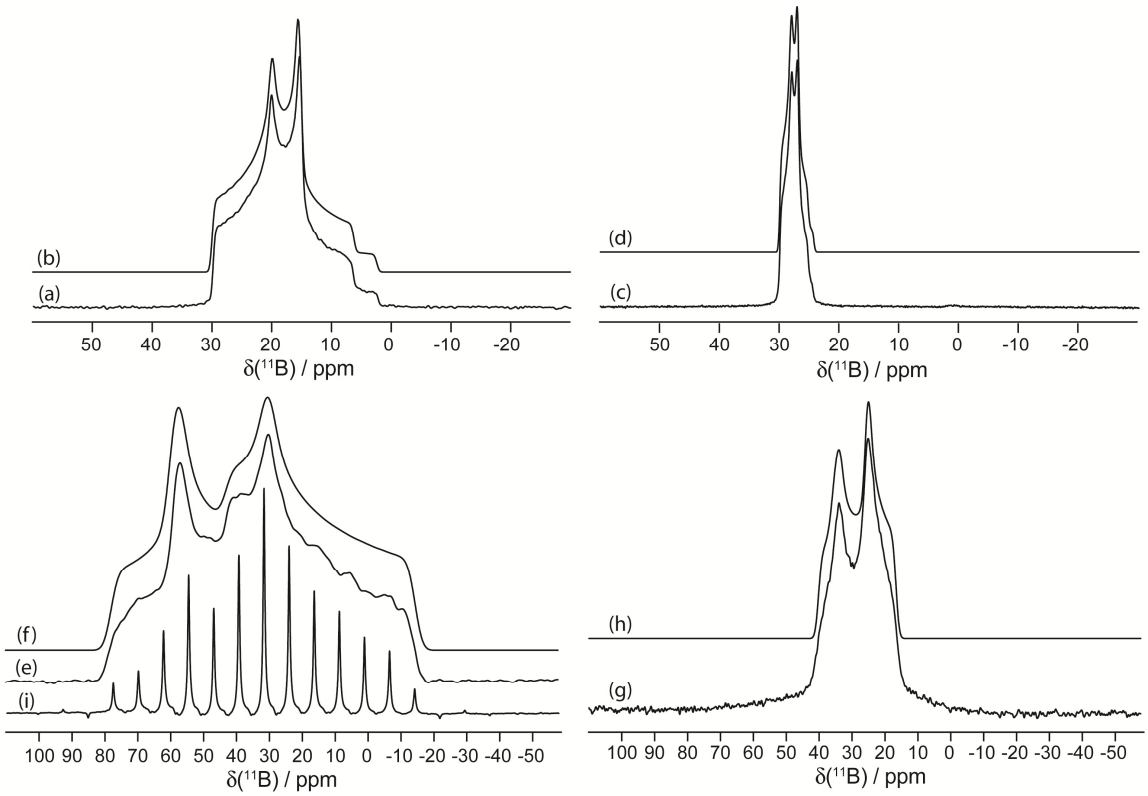

Figure 2.10: Solid-state boron-11 NMR spectroscopy of **9**. Experimental spectra of a powdered sample undergoing MAS are shown in (a) ^{11}B at 9.40 T and (c) ^{11}B at 21.1 T. Best-fit spectra were simulated using WSolids (traces (b) and (d)) using the parameters given in Table 2.1. Experimental spectra of stationary powdered samples are shown in (e) ^{11}B at 9.40 T and (g) ^{11}B at 21.1 T. Best-fit spectra were simulated using WSolids (traces (f) and (h)) using the parameters given in Table 2.1. Experimental QCPMG spectrum of a stationary powdered sample is shown in (i) ^{11}B at 9.40 T.

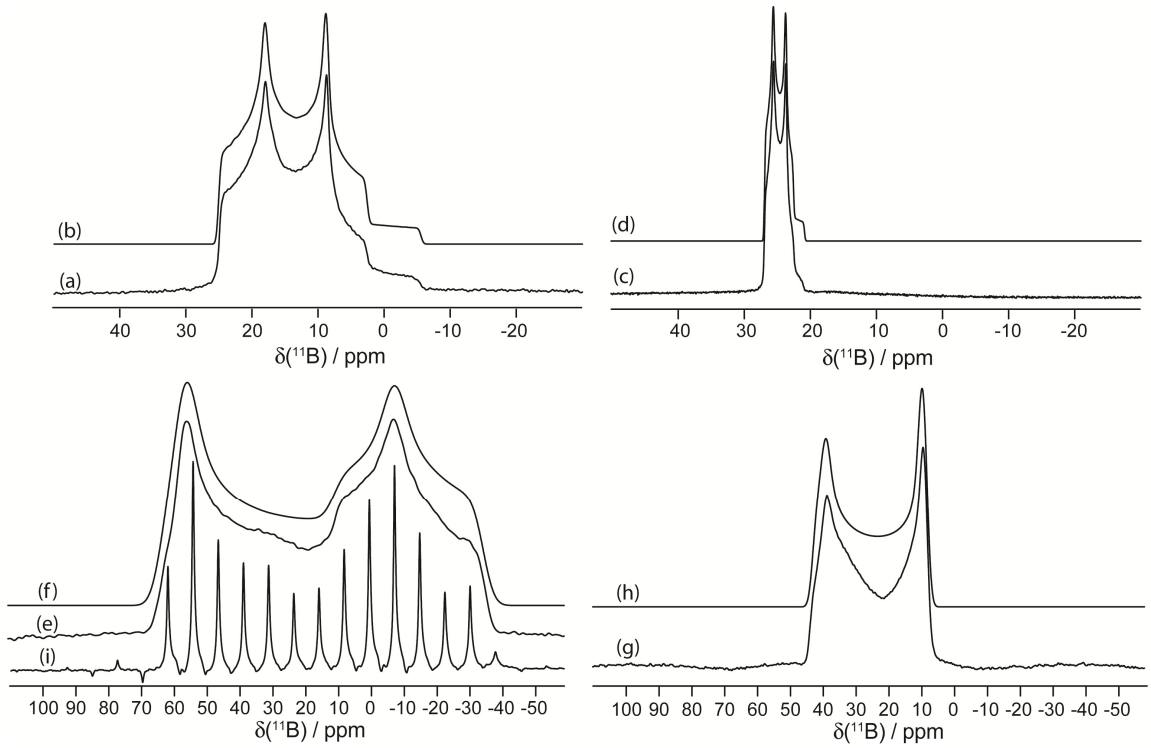

Figure 2.11: Solid-state boron-11 NMR spectroscopy of **10**. Experimental spectra of a powdered sample undergoing MAS are shown in (a) ^{11}B at 9.40 T and (c) ^{11}B at 21.1 T. Best-fit spectra were simulated using WSolids (traces (b) and (d)) using the parameters given in Table 2.1. Experimental spectra of stationary powdered samples are shown in (e) ^{11}B at 9.40 T and (g) ^{11}B at 21.1 T. Best-fit spectra were simulated using WSolids (traces (f) and (h)) using the parameters given in Table 2.1. Experimental QCPMG spectrum of a stationary powdered sample is shown in (i) ^{11}B at 9.40 T.

A small range in $C_Q(^{11}B)$ is observed (i.e., from 2.66 MHz for compound **9** to 3.29 MHz for compound **1**). In general, the $C_Q(^{11}B)$ values for the boronic acids tend to be slightly larger than for the esters; however, there is overlap in the ranges for each class of compound. Similarly, a small range in **Ω** is observed (i.e., 10 ppm for compound **9** to 40 ppm for compound **2**). Usually, the **Ω** values for the boronic acids tend to be slightly larger than for the esters; however, there is overlap in the ranges for each class of compound.

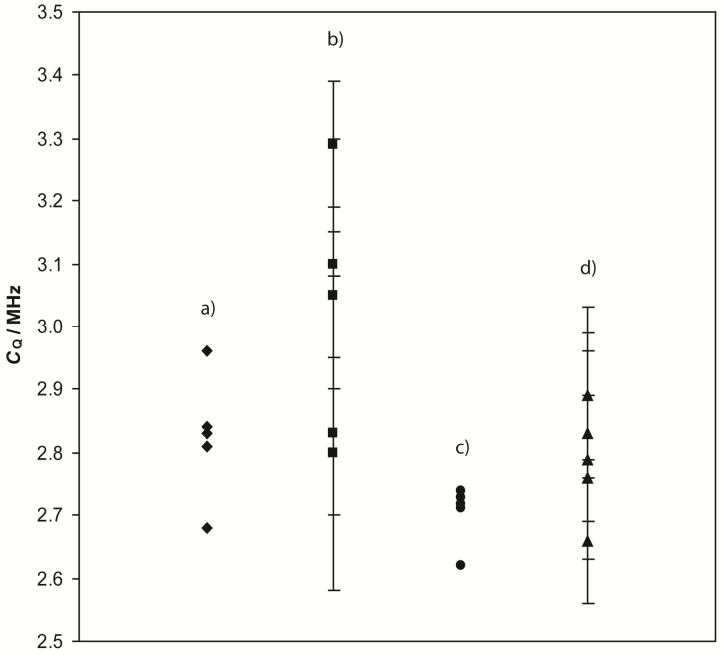

Figure 2.12: Calculated and experimental boron C_Q for the boronic acids and boronic esters studied. Calculated values for boronic acid dimers which take into account hydrogen bonding interactions are included where applicable. ADF calculations were performed using the GGA revPBE functional and TZP basis set on all atoms. The following data are shown: a) calculated C_Q for boronic acids, b) experimental C_Q for

boronic acids, c) calculated C_Q for boronic esters, and d) experimental C_Q for boronic esters.

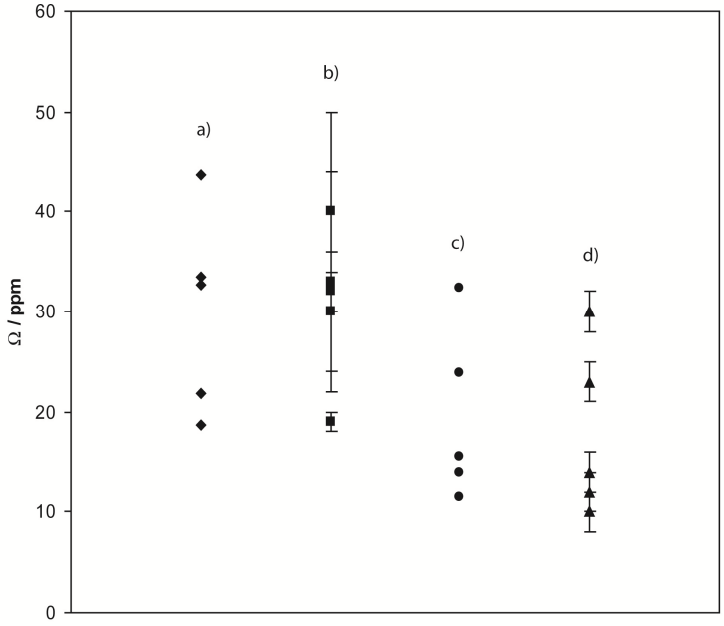

Figure 2.13: Calculated and experimental boron **Ω** values for the boronic acids and boronic esters studied. Calculated values for boronic acid dimers which take into account hydrogen bonding interactions are included where applicable. ADF calculations were performed using the GGA revPBE functional and TZP basis set on all atoms. The following data are shown: a) calculated **Ω** values for boronic acids, b) experimental **Ω** values for boronic acids, c) calculated **Ω** values for boronic esters, and d) experimental **Ω** values for boronic esters.

Figures 2.14 – 2.22 illustrate the $\mathbf{B}_0$ dependencies of the second-order quadrupolar interaction and CSA observed in the magnetic resonance line shape for several of the boronic acids and esters. Shown in these Figures are the stationary spectra for each

compound, the corresponding best-fit analytical simulation, and a simulation where the CSA is ignored (i.e., Ω = 0 ppm). Comparing the traces where CSA is included to those where it is not for the data acquired at 9.40 T, one clearly sees that the difference between the two traces is minimal. At 21.1 T, however, the difference between the two traces is clear. This holds true for both boronic acids and esters.

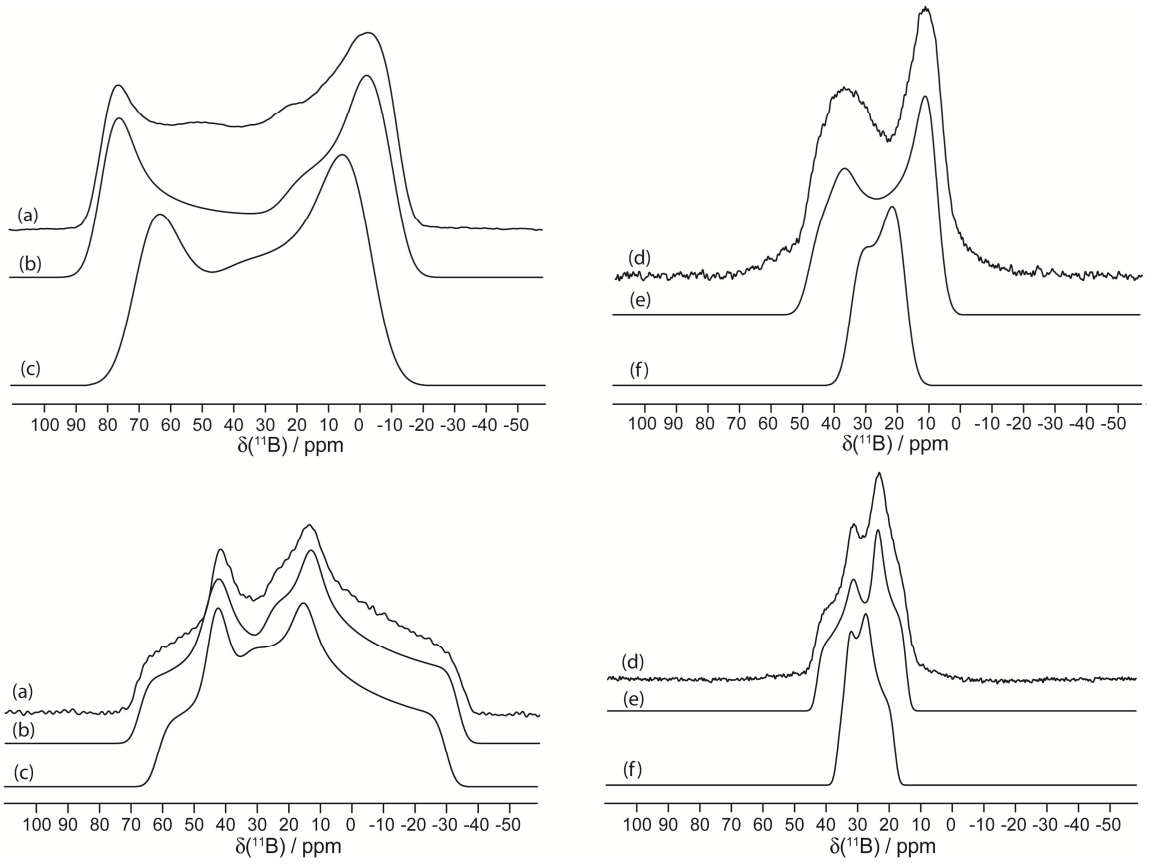

Figure 2.14: Solid-state boron-11 NMR spectroscopy of **3** (top), and **8** (bottom). Experimental spectra of stationary powdered samples are shown in (a) ^{11}B at 9.40 T and (d) ^{11}B at 21.1 T. Best-fit spectra were simulated using WSolids (traces (b) and (e)) using the parameters given in Table 2.1. Best-fit spectra not taking the effects of CSA into account were simulated using WSolids (traces (c) and (f)) using the parameters given in Table 2.1, but where the values for span were set to 0 ppm.

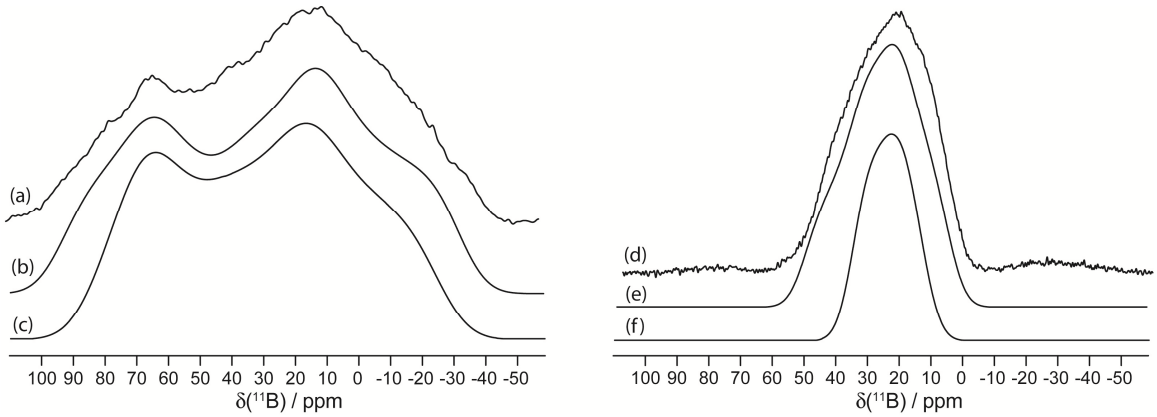

Figure 2.15: Solid-state boron-11 NMR spectroscopy of **1**. Experimental spectra of stationary powdered samples are shown in (a) ^{11}B at 9.40 T and (d) ^{11}B at 21.1 T. Best-fit spectra were simulated using WSolids (traces (b) and (e)) using the parameters given in Table 2.1. Best-fit spectra not taking the effects of CSA into account were simulated using WSolids (traces (c) and (f)) using the parameters given in Table 2.1, but where the values for Ω were set to 0 ppm.

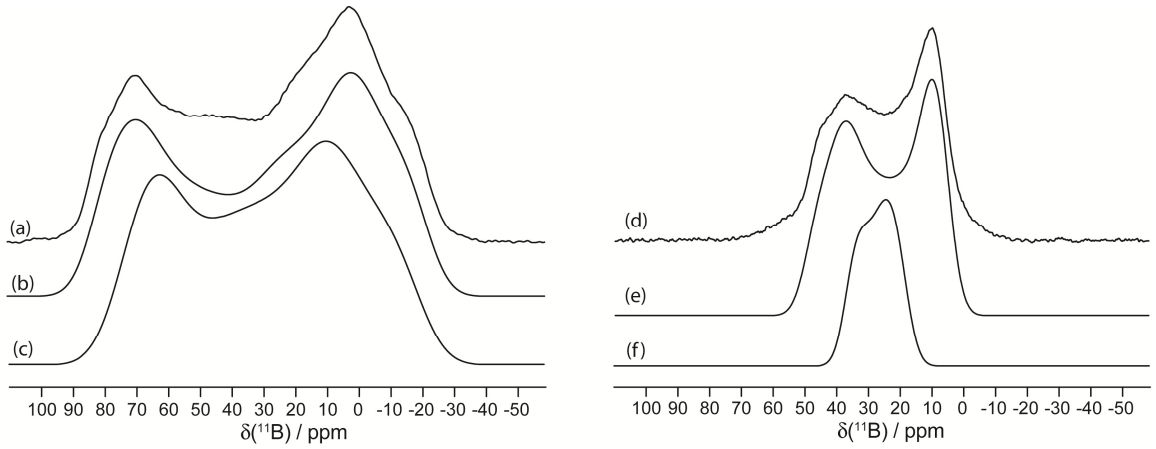

Figure 2.16: Solid-state boron-11 NMR spectroscopy of **2**. Experimental spectra of stationary powdered samples are shown in (a) ^{11}B at 9.40 T and (d) ^{11}B at 21.1 T. Best-

fit spectra were simulated using WSolids (traces (b) and (e)) using the parameters given in Table 2.1. Best-fit spectra not taking the effects of CSA into account were simulated using WSolids (traces (c) and (f)) using the parameters given in Table 2.1, but where the values for Ω were set to 0 ppm.

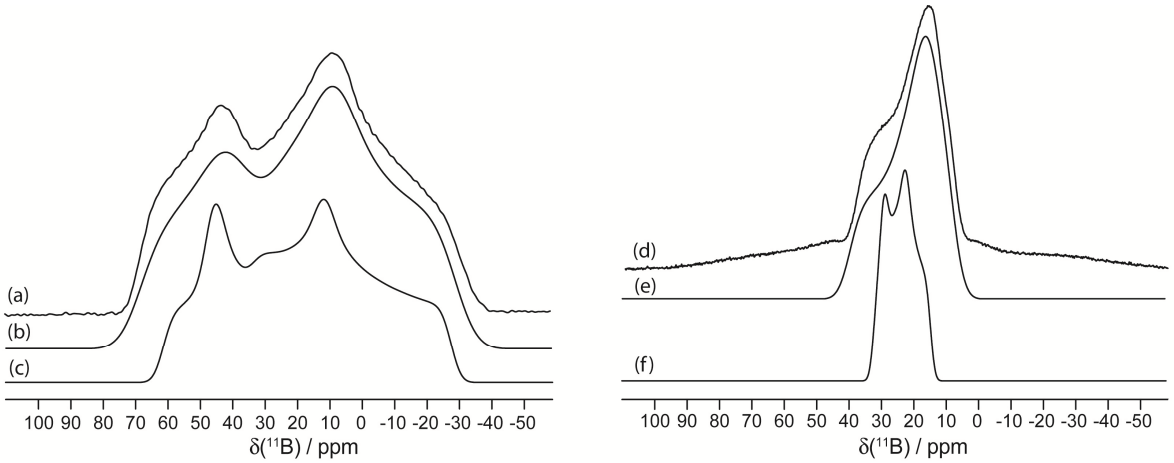

Figure 2.17: Solid-state boron-11 NMR spectroscopy of **4**. Experimental spectra of stationary powdered samples are shown in (a) ^{11}B at 9.40 T and (d) ^{11}B at 21.1 T. Best-fit spectra were simulated using WSolids (traces (b) and (e)) using the parameters given in Table 2.1. Best-fit spectra not taking the effects of CSA into account were simulated using WSolids (traces (c) and (f)) using the parameters given in Table 2.1, but where the values for Ω were set to 0 ppm.

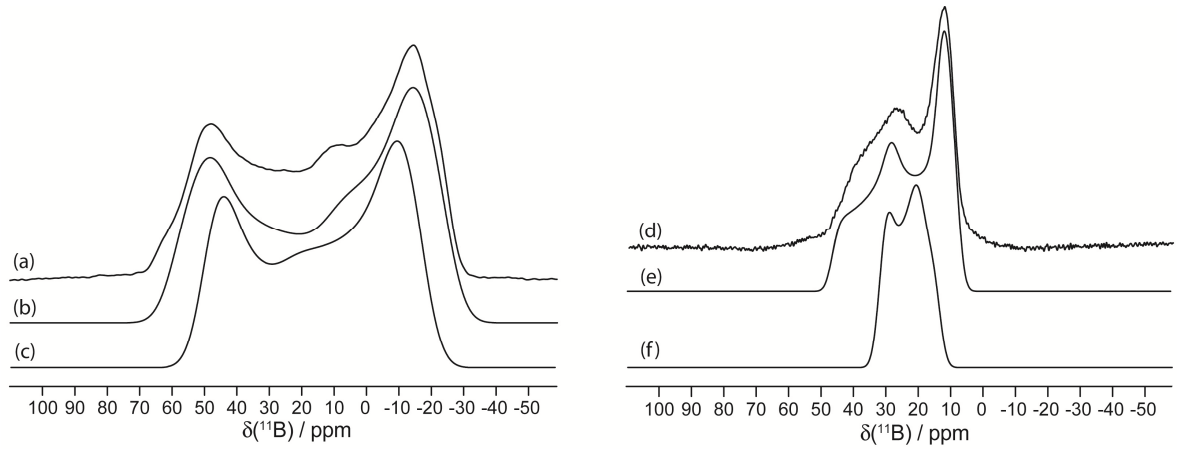

Figure 2.18: Solid-state boron-11 NMR spectroscopy of **5**. Experimental spectra of stationary powdered samples are shown in (a) ^{11}B at 9.40 T and (d) ^{11}B at 21.1 T. Best-fit spectra were simulated using WSolids (traces (b) and (e)) using the parameters given in Table 2.1. Best-fit spectra not taking the effects of CSA into account were simulated using WSolids (traces (c) and (f)) using the parameters given in Table 2.1, but where the values for Ω were set to 0 ppm.

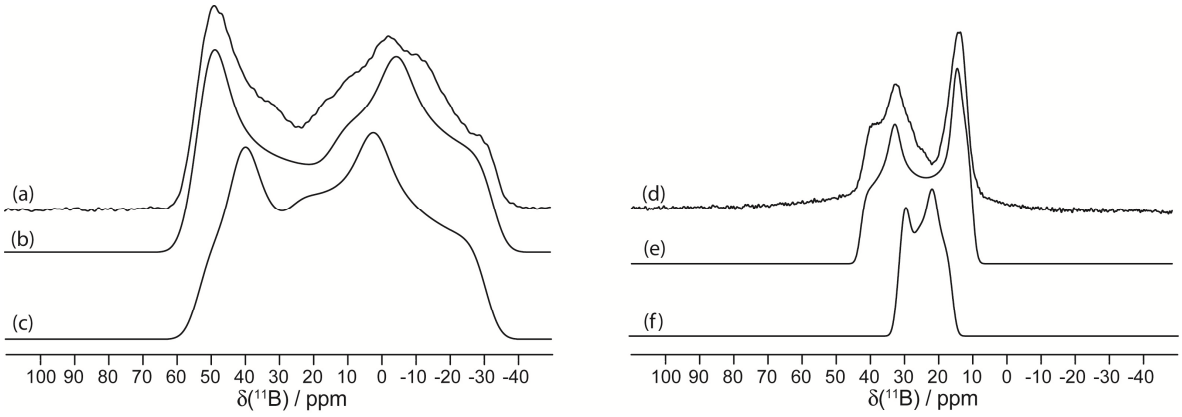

Figure 2.19: Solid-state boron-11 NMR spectroscopy of **6**. Experimental spectra of stationary powdered samples are shown in (a) ^{11}B at 9.40 T and (d) ^{11}B at 21.1 T. Best-fit spectra were simulated using WSolids (traces (b) and (e)) using the parameters given

in Table 2.1. Best-fit spectra not taking the effects of CSA into account were simulated using WSolids (traces (c) and (f)) using the parameters given in Table 2.1, but where the values for Ω were set to 0 ppm.

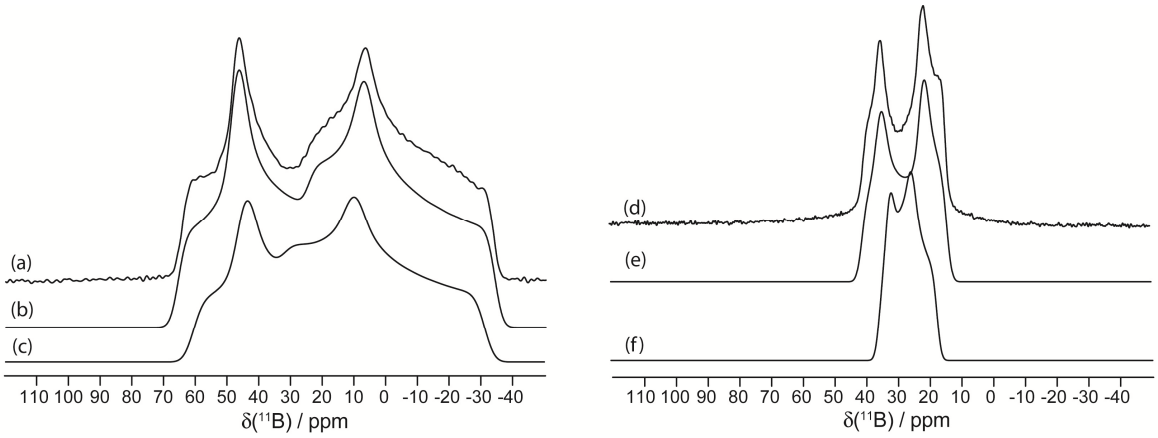

Figure 2.20: Solid-state boron-11 NMR spectroscopy of **7**. Experimental spectra of stationary powdered samples are shown in (a) ^{11}B at 9.40 T and (d) ^{11}B at 21.1 T. Best-fit spectra were simulated using WSolids (traces (b) and (e)) using the parameters given in Table 2.1. Best-fit spectra not taking the effects of CSA into account were simulated using WSolids (traces (c) and (f)) using the parameters given in Table 2.1, but where the values for Ω were set to 0 ppm.

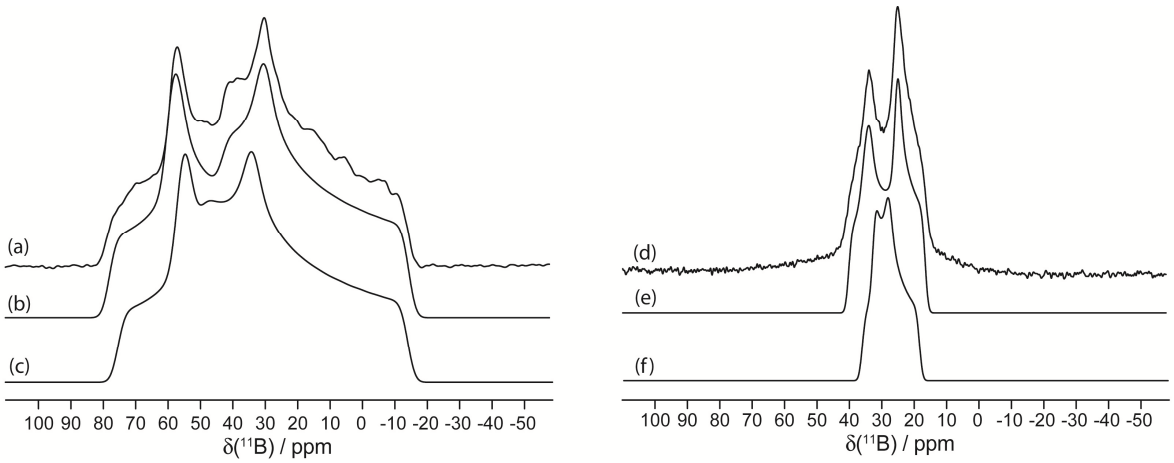

Figure 2.21: Solid-state boron-11 NMR spectroscopy of **9**. Experimental spectra of stationary powdered samples are shown in (a) ^{11}B at 9.40 T and (d) ^{11}B at 21.1 T. Best-fit spectra were simulated using WSolids (traces (b) and (e)) using the parameters given in Table 2.1. Best-fit spectra not taking the effects of CSA into account were simulated using WSolids (traces (c) and (f)) using the parameters given in Table 2.1, but where the values for Ω were set to 0 ppm.

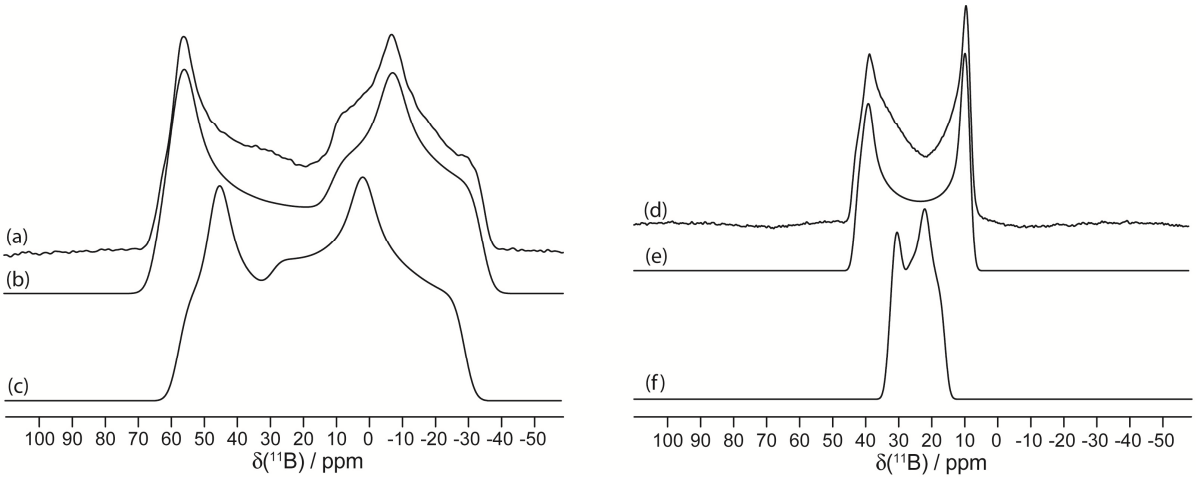

Figure 2.22: Solid-state boron-11 NMR spectroscopy of **10**. Experimental spectra of stationary powdered samples are shown in (a) ^{11}B at 9.40 T and (d) ^{11}B at 21.1 T. Best-fit spectra were simulated using WSolids (traces (b) and (e)) using the parameters given

in Table 2.1. Best-fit spectra not taking the effects of CSA into account were simulated using WSolids (traces (c) and (f)) using the parameters given in Table 2.1, but where the values for Ω were set to 0 ppm.

Figure 2.23 is a graphical representation of the measured Ω values for different trigonal planar boron bonding environments.[58] As the central boron atom is bound to more oxygen atoms and fewer carbon atoms, the experimental Ω values decrease dramatically.

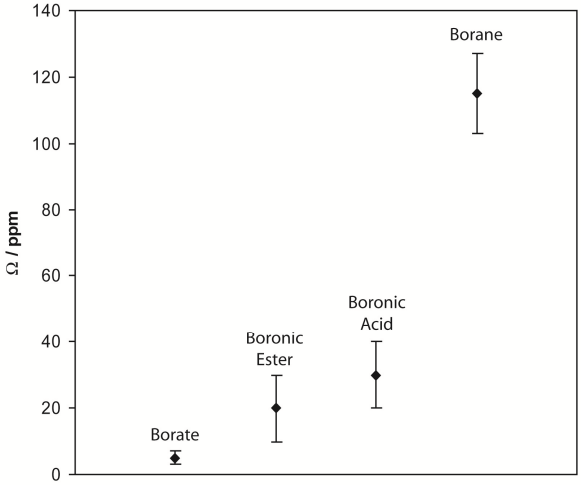

Figure 2.23: Graphical representation of experimental Ω values for the compounds being studied (Table 2.1) and different borate and borane compounds.[58] Data points indicate average values for a range of compounds (boronic acids and esters) or single experimental measurements (borate and borane). The vertical bars for the boronic acid and ester data show the range of Ω for each class of compound. In the case of borane and borate, the vertical bars represent the experimental measurement error for one compound (trimesitylborane and triphenylborate).[58] As the central boron atom is bound to more

oxygen atoms and fewer carbon atoms, the experimental Ω values decrease dramatically, as does their range. See text for further discussion.

This trend may be rationalized by considering the atomic orbitals for each species involved. The oxygen atoms can donate electron density through lone pairs of electrons into the vacant *p*-orbital of the boron. As described in more detail later, the contributions to the paramagnetic portion of the total **σ** in the boron trigonal plane are reduced upon increasing oxygen coordination, which can explain the observed decrease in the measured Ω.[58] The boronic acids and esters have Ω values in the small/intermediate range relative to borates on the low end and boranes on the high end. Although the spans being examined are small, they are the most characteristic NMR parameters for each compound and can successfully be related to the immediate bonding environment (Figure 2.23).

2.2.2 Computational Results

Shown in Table 2.2 are the boron EFG and **σ** tensor results calculated using Becke, three-parameter, Lee-Yang-Parr (B3LYP), restricted Hartree-Fock (RHF), and generalized gradient approximation - revised Perdew-Burke-Ernzerhof (GGA-revPBE) methods for compounds **1** to **10**. Table 2.3 contains all of the computational results pertaining to the mentioned computational methods listing the skew values as well as the Euler angles.

Table 2.2: Calculated EFG and CS tensor parameters for compounds **1** to **10**.[a]

		B3LYP			RHF			GGA revPBE			
	Sample	C_Q / MHz	η_Q	Ω / ppm	C_Q / MHz	η_Q	Ω / ppm	C_Q / MHz	η_Q	Ω / ppm	ϕ_{CCBO} / º
Boronic Acids	**1**	3.09	0.658	20.9	3.58	0.517	19.1	2.83	0.644	21.9	0.0
	1†	3.06	0.632	21.1	3.57	0.498	21.6	2.81	0.570	25.0	8.7
	2	3.21	0.402	40.9	3.66	0.283	32.9	2.96	0.383	43.7	90.0
	2†	3.16	0.399	41.6	3.63	0.271	36.1	2.91	0.380	41.8	90.0
	3	3.03	0.534	27.9	3.50	0.406	19.3	2.81	0.504	33.4	28.1
	3†	3.00	0.382	27.9	3.49	0.272	18.2	2.74	0.362	27.7	0.1
	4	2.96	0.482	17.3	3.48	0.360	12.6	2.68	0.447	18.7	0.0
	4†	2.95	0.628	25.5	3.47	0.461	20.9	2.68	0.553	23.4	0.0
	5	3.07	0.637	28.2	3.54	0.436	17.5	2.84	0.524	32.6	36.7
	5†	2.94	0.565	28.3	3.53	0.406	22.5	2.68	0.537	28.1	19.9
Boronic Esters	**6**	2.93	0.622	23.1	3.48	0.470	17.4	2.62	0.649	23.9	0.5
	7	3.01	0.548	15.6	3.57	0.405	13.0	2.72	0.545	11.5	3.0
	8	3.01	0.633	20.0	3.56	0.497	23.9	2.71	0.632	15.5	2.9
	9	3.03	0.597	18.2	3.59	0.453	17.7	2.73	0.592	14.0	1.2
	10	3.05	0.495	32.8	3.56	0.397	27.9	2.74	0.529	32.3	61.3
Boric Acid		2.46	0.304	13.3	3.04	0.235	10.2	2.24	0.300	11.4	0.0

† Corresponds to boronic acid dimer

[a] Calculated values for boronic acid dimers which take into account hydrogen bonding interactions are included where applicable. Hybrid DFT calculations were performed using the B3LYP functional and the 6-311+G* basis set on all elements. RHF calculations were performed using the 6-311+G* basis set on elements. ADF calculations were performed using the GGA revPBE functional and TZP basis set on all atoms. ϕ_{CCBO} is defined in Figure 2.25. Boric acid is included as the impurity present at 19.6 ppm in compounds **2** and **3**.

Table 2.3: Calculated magnetic shielding tensor skew and Euler angles for compounds **1** to **10** using a single basis set on all atoms.[a]

		B3LYP				RHF			
	Sample	κ	α / º	β / º	γ / º	κ	α / º	β / º	γ / º
Boronic Acids	**1**	0.81	6	0	11	0.15	276	0	90
	1†	0.24	182	8	201	0.05	242	7	62
	2	0.44	223	0	227	0.69	178	0	272
	2†	0.00	326	0	187	0.22	87	0	68
	3	0.24	356	6	76	0.37	41	0	89
	3†	-0.24	156	0	254	0.01	154	0	249
	4	-0.87	200	0	276	-0.76	217	90	270
	4†	-0.38	127	90	270	-0.14	209	90	90
	5	0.64	177	16	275	0.73	175	13	294
	5†	-0.36	131	12	253	-0.15	219	13	306
Boronic Esters				1				3	
	6	0.71	90		0	0.44	90		90
	7	0.23	0	1	360	-0.93	0	1	360
	8	-0.58	30	1	329	-0.57	268	90	90
	9	-0.20	111	1	251	-0.79	91	88	269
	10	0.88	342	5	66	0.44	347	8	12
Boric Acid		-0.69	241	0	112	-0.67	264	90	90

†Corresponds to boronic acid dimer

[a] Calculated boron κ and Euler angles for each boronic acid and ester compound studied. Calculated values for boronic acid dimers which take into account hydrogen bonding interactions are included where applicable. Hybrid DFT calculations were performed using the B3LYP functional and the 6-311+G* basis set on all elements. RHF calculations were performed using the 6-311+G* basis set on elements. Boric acid is included as the impurity present at 19.6 ppm in compounds **2** and **3**.

Calculations similar to the ones discussed here were carried out on boronic acids and boronic esters **1** – **10**. Both hybrid DFT calculations using the B3LYP functional as well as RHF calculations were performed using the 6-31G* basis set on all first and second row elements, while the aug-cc-pVTZ basis set was used on all heavier elements. These calculations yielded results that were comparable to experimental results; however, calculations employing a higher level basis set (6-311+G*) were carried out in attempts to achieve calculated NMR parameters that were more in agreement with the experimental data. Logically, computations which use a higher level basis set should provide more accurate results. That is indeed the case for the results discussed here. Although calculations using the 6-31G* basis set provided results that were not in agreement to the same extent as when the 6-311+G* basis set is used, those data are still useful and can be used to obtain approximate values for the NMR parameters being calculated. Using a higher level basis set, in the case of these boron compounds, will generally provide more accurate results. However, this comes at the cost of having to expend more computational resources.

Table 2.4: Calculated ^{11}B EFG parameters and CSA for compounds **1** to **10**.[a]

		B3LYP			RHF			GGA revPBE			
	Sample	C_Q / MHz	η_Q	Ω / ppm	C_Q / MHz	η_Q	Ω / ppm	C_Q / MHz	η_Q	Ω / ppm	ϕ_{CCBO} / º
Boronic Acids	**1**	2.82	0.631	17.1	2.84	0.614	16.6	2.83	0.644	21.9	0.0
	1†	2.61	0.494	22.0	3.09	0.419	20.1	2.81	0.570	25.0	8.7
	2	2.92	0.439	36.0	2.90	0.422	34.7	2.96	0.383	43.7	90.0
	2†	2.86	0.302	38.4	2.88	0.288	38.0	2.91	0.380	41.8	90.0
	3	2.23	0.922	16.6	2.42	0.782	17.0	2.81	0.504	33.4	28.1
	3†	2.80	0.338	22.7	2.79	0.339	22.4	2.74	0.362	27.7	0.1
	4	2.78	0.466	13.8	3.34	0.364	10.3	2.68	0.447	18.7	0.0
	4†	2.76	0.561	22.4	3.32	0.426	18.7	2.68	0.553	23.4	0.0
	5	2.07	0.548	15.8	2.11	0.377	17.2	2.84	0.524	32.6	36.7
	5†	2.43	0.449	24.7	2.43	0.449	24.8	2.68	0.537	28.1	19.9
Boronic Esters	**6**	2.72	0.621	17.0	2.72	0.624	16.0	2.62	0.649	23.9	0.5
	7	2.78	0.582	11.5	2.79	0.574	10.8	2.72	0.545	11.5	3.0
	8	2.79	0.640	15.5	2.80	0.638	15.4	2.71	0.632	15.5	2.9
	9	2.62	0.677	12.0	3.09	0.586	17.6	2.73	0.592	14.0	1.2
	10	2.10	0.186	15.5	2.14	0.274	16.7	2.74	0.529	32.3	61.3
Boric Acid		2.30	0.249	10.7	2.90	0.183	7.9	2.24	0.300	11.4	0.0

†Corresponds to boronic acid dimer

[a] Calculated boron C_Q, η_Q, and Ω values for each boronic acid and ester compound studied. Calculated values for boronic acid dimers which take into account hydrogen bonding interactions are included where applicable. Hybrid DFT calculations were performed using the B3LYP functional and the 6-31G* basis set on all first and second row elements, while the aug-cc-pVTZ basis set was used on all heavier elements. RHF calculations were performed using the 6-31G* basis set on all first and second row elements, while the aug-cc pVTZ basis set was used on all heavier elements. ADF calculations were performed using the GGA revPBE functional and TZP basis set on all atoms. ϕ_{CCBO} is shown (see Figure 2.25). Boric acid is included as the impurity present at 19.6 ppm in compounds **2** and **3**.

Table 2.5: Calculated magnetic shielding tensor skew and Euler angles for compounds **1** to **10** using two different basis sets.[a]

		B3LYP				RHF			
	Sample	κ	α / º	β / º	γ / º	κ	α / º	β / º	γ / º
Boronic Acids	**1**	0.79	295	0	82	0.78	283	0	98
	1†	-0.19	136	16	246	-0.60	300	16	71
	2	0.47	236	0	214	0.36	180	0	270
	2†	0.15	2	0	143	0.09	353	0	151
	3	0.54	357	14	77	0.43	355	15	78
	3†	-0.50	319	0	169	-0.48	314	0	173
	4	-0.96	24	0	90	-0.81	217	90	270
	4†	-0.27	306	90	90	-0.12	121	90	270
	5	0.85	2	18	69	0.85	2	17	74
	5†	-0.35	133	19	254	-0.34	133	18	253
Boronic Esters	**6**	0.63	270	1	180	0.67	90	1	360
	7	0.00	359	0	1	-0.29	0	2	360
	8	-0.84	77	0	282	-0.96	268	89	91
	9	-0.45	164	2	197	-0.58	91	90	268
	10	0.84	184	9	175	0.86	5	9	354
Boric Acid		-0.68	151	0	203	-0.78	84	90	270

†Corresponds to boronic acid dimer

[a] Calculated boron Euler angles, which represent the corresponding angles between the EFG and shielding tensor components in their respective PASs, and κ values for each boronic acid and ester compound studied. Calculated values for boronic acid dimers which take into account hydrogen bonding interactions are included where applicable. Hybrid DFT calculations were performed using the B3LYP functional and the 6-31G* basis set on all first and second row elements, while the aug-cc-pVTZ basis set was used on all heavier elements. RHF calculations were performed using the 6-31G* basis set on all first and second row elements, while the aug-cc-pVTZ basis set was used on all heavier elements. Boric acid is included as the impurity present at 19.6 ppm in compounds **2** and **3**.

The GGA-revPBE calculated isotropic magnetic shielding constants are plotted against the experimental values of δ_{iso} in Figure 2.24. A good correlation exists between the experimental and calculated data, as quantified by a correlation coefficient of R^2 = 0.9000 (excluding an outlier for boronic acid **2**). The experimental spans are also best reproduced by the GGA-revPBE calculations, as quantified by a correlation coefficient of R^2 = 0.9818, once one outlier is excluded (Figure 2.24). The outlier, corresponding to boronic acid **1**, may be tentatively rationalized by considering the relatively large experimental error associated with this particular measurement.

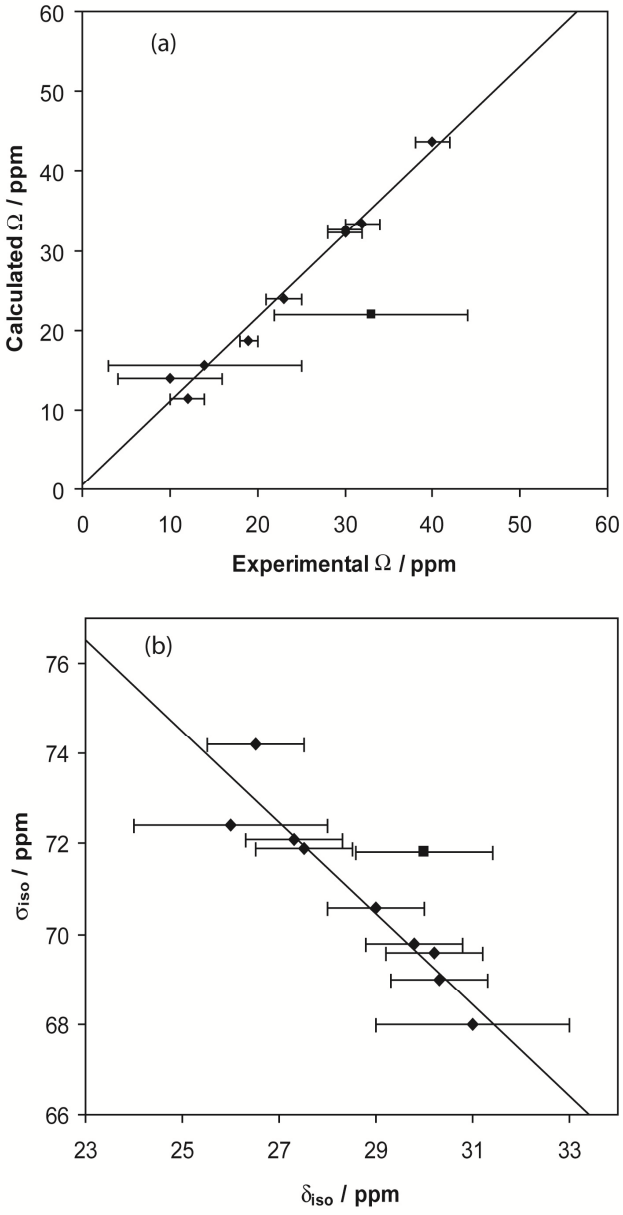

Figure 2.24: Correlation between the calculated (ADF/GGA revPBE) and experimental span values (a) and calculated total isotropic shielding and experimental isotropic chemical shift values (b) measured in the solid state for each boronic acid and ester studied. Experimental **Ω** is plotted against the calculated **Ω** values for the monomer in all cases. Experimental isotropic chemical shift is plotted against the calculated total isotropic shielding values for the dimer where applicable. **Ω** data ((a), diamonds) are described by a R^2 value of 0.9818 and a trendline given by y = 1.0536x + 0.482. One

data point for boronic acid **1** ((a), square) is not taken into account and is plotted separately. Data in part (b) (diamonds) have a R^2 value of 0.9000 with a trendline given by y = -1.0117x + 99.8. One stray data point for boronic acid **2** ((b), square) is not taken into account and is plotted separately.

The GGA-revPBE-calculated values can be used to discuss the impact of hydrogen bonding, electronic substituents, and ϕ_{CCBO} on the span. The two hydroxy groups present in boronic acids are capable of engaging in intermolecular hydrogen bonding. Therefore, if hydrogen bonding interactions are present, the boronic acids being considered usually exist as dimers. Only one crystal structure exists for the compounds being studied, that of compound **4**, which is a dimer.[59] Boronic acids may also exist as oligomers in the solid state, as discussed, for example, by Maly *et al*.[60,61] Calculations on both boronic acid monomers and dimers were performed to assess the impact of hydrogen bonding on the ^{11}B NMR interaction tensors. It was found that $C_Q(^{11}B)$ generally decreases slightly in the dimers, relative to the monomers. There is no consistent trend in the change of Ω as a result of hydrogen bonding in the dimers. This is attributed to the observation that the value of ϕ_{CCBO} (as shown in Figure 2.25) of the optimized structures changes differentially from compound to compound as a result of dimerization, in addition to the simple fact that the hydroxy groups are hydrogen bonded.

Therefore, the impact of varying ϕ_{CCBO} upon calculated Ω values was studied next. Shown in Table 2.2 are the GGA-revPBE optimized dihedral angles for each boronic acid and ester (see also Figure 2.25), where the two carbon atoms are located in the aromatic ring, and the boron and oxygen atoms are part of the boronic acid or ester functionality.

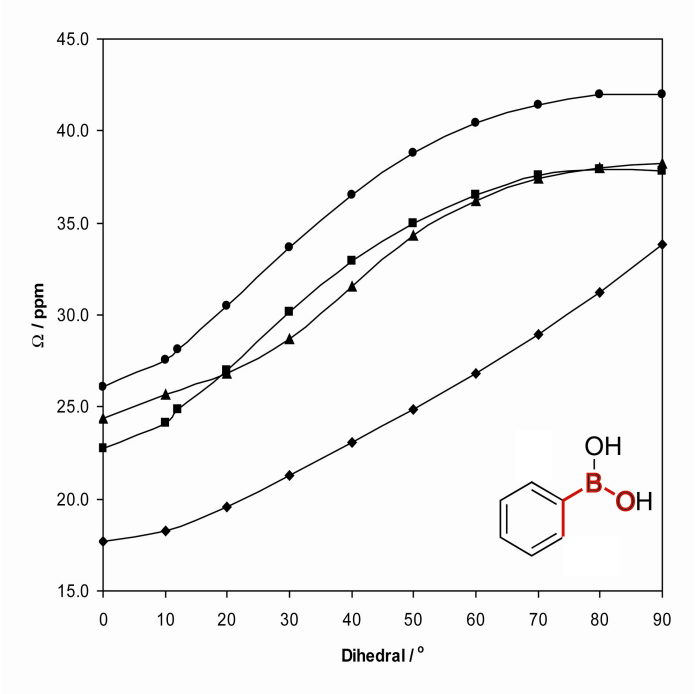

Figure 2.25: Correlation between the calculated **Ω** values and ϕ_{CCBO} for monomeric and dimeric forms of phenylboronic acid. Shown are results for (diamonds) Gaussian (B3LYP) monomer, (squares) Gaussian (B3LYP) dimer, (triangles) ADF (GGA revPBE) monomer, and (circles) ADF (GGA revPBE) dimer. Shown in red is ϕ_{CCBO}.

As noted earlier, ϕ_{CCBO} is altered primarily by sterics, and depends on the bulkiness of nearby substituents on the aromatic ring. For example, for every boronic acid and ester possessing bulky substituents on the aromatic ring, particularly in the ortho position, the value of ϕ_{CCBO} is always much greater relative to when there is a less bulky substituent. As this angle is systematically varied, the orientations of MOs centered on boron, relative to the aromatic ring, change accordingly. An examination of the correlation between experimental and calculated spans (Figure 2.24) suggested a potential relationship between ϕ_{CCBO} and both the experimental and calculated **Ω** values. Previous work by Zhang *et al.* reported a dependence of the computed energy of boronic acids on this

dihedral angle.[62] A plot of the value of Ω as a function of the calculated value of ϕ_{CCBO} for each compound reveals no clear and direct correlation, which is not surprising, as there are several variables changing simultaneously. For example, boronic acids have hydrogen bonding interactions taking place whereas the esters do not; the aromatic substituents are different on the various compounds, and the dihedral angle changes primarily due to sterics. To determine if there is an underlying fundamental correlation between span and ϕ_{CCBO}, phenylboronic acid was chosen as a model system. The structures of both the phenylboronic acid monomer and dimer were optimized computationally. The value of ϕ_{CCBO} was then systematically altered from 0 to 90° in 10° steps. For each ϕ_{CCBO}, spans were calculated using both B3LYP and GGA-revPBE density functional methods. The resulting variations of the spans with dihedral angle are shown in Figure 2.25. Two important conclusions may be drawn: (i) for all four data sets, there is a distinct positive correlation between Ω and ϕ_{CCBO}; (ii) in all cases, the Ω values are smaller for the phenylboronic acid monomer than for the dimer. It is clear that calculations predict that the presence of the hydrogen bonding interaction results in an increased span. The calculated variation of the span results from small changes (on the order of 1 to 5 ppm) in the values of the principal components of the magnetic shielding tensor as a result of hydrogen bonding. In no case do the calculations imply that the span varies because of the unilateral change of a single component (see Table 2.6). It is the combination of these small changes, specifically in σ_{11} and σ_{33}, rather than a significant change in a single principal component, which leads to variation in the Ω values. The σ_{33} values become slightly larger, and the σ_{11} values become smaller, resulting in an overall increased span.

Table 2.6: Calculated magnetic shielding tensor components and Ω for phenylboronic acid monomer and dimer as the dihedral is varied from 0 to 90º.[a]

	Monomer[b]				Dimer[b]			
ϕ_{CCBO} / º	σ_{11}	σ_{22}	σ_{33}	Ω / ppm	σ_{11}	σ_{22}	σ_{33}	Ω / ppm
0	61.2	67.7	85.6	24.4	56.9	72.5	83.0	26.1
10	61.0	66.6	86.2	25.2	56.2	71.9	83.7	27.5
20	60.7	64.0	87.5	26.8	54.8	69.9	85.3	30.5
30	60.2	61.0	88.9	28.7	53.1	67.6	86.8	33.7
40	58.5	59.5	90.1	31.6	51.5	65.5	88.1	36.6
50	56.7	58.8	91.0	34.3	50.4	63.7	89.2	38.8
60	55.6	58.0	91.8	36.2	49.8	62.2	90.3	40.5
70	55.0	57.4	92.4	37.4	49.7	60.9	91.2	41.5
80	54.8	56.9	92.8	38.0	49.9	59.9	91.9	42.0
90	54.8	56.7	93.0	38.2	50.3	29.2	92.3	42.0

	Monomer[c]				Dimer[c]			
ϕ_{CCBO} / º	σ_{11}	σ_{22}	σ_{33}	Ω / ppm	σ_{11}	σ_{22}	σ_{33}	Ω / ppm
0	80.1	80.1	97.8	17.7	73.3	87.9	96.1	22.8
10	79.8	80.0	98.1	18.3	72.7	87.5	96.8	24.1
20	79.1	79.9	98.7	19.6	71.3	86.1	98.3	27.0
30	78.2	79.6	99.6	21.4	69.7	84.6	99.9	30.2
40	77.3	79.3	100.5	23.2	68.3	83.1	101.2	32.9
50	76.5	78.9	101.4	24.9	67.3	81.8	102.3	35.0
60	75.7	78.6	102.5	26.8	66.9	80.4	103.4	36.5
70	74.9	78.2	103.8	28.9	66.8	79.2	104.4	37.6
80	74.1	77.7	105.3	31.2	67.0	78.1	105.0	38.0
90	73.1	77.1	106.9	33.8	67.5	77.2	105.3	37.8

[a] Calculated boron ϕ_{CCBO}, Ω, and shielding tensor components for phenylboronic acid monomer and dimer as ϕ_{CCBO} is varied from 0 to 90º.

[b] Hybrid DFT calculations were performed using the B3LYP functional and the 6-31G* basis set on all first and second row elements, while the aug-cc-pVTZ basis set was used on all heavier elements.

[c] ADF calculations were performed using the GGA revPBE functional and TZP basis set on all atoms.

2.2.3 MO Analysis of Boron Shielding Tensors

GGA-revPBE calculations for the phenylboronic acid monomer were used to compile shielding tensor magnitude and orientation information at each ϕ_{CCBO}. Not surprisingly, the eigenvector corresponding to σ_{33} remains nearly perpendicular to the boron bonding plane. For phenylboronic acid, σ_{33} is calculated to intersect the boron bonding plane at an angle ranging from 76 to 90º, depending on the value of ϕ_{CCBO}. In addition, for boronic acids and esters **1** to **10**, σ_{33} remains perpendicular (within 18º) to the boron bonding plane. (Compound **4** is an exception to this rule with σ_{22} being perpendicular, although compound **4** is also unique in the sense that it is a boronic acid monoester). To relate the MOs to the observed and calculated Ω values, the individual MO contributions to total shielding must first be examined. As previously mentioned, magnetic shielding may be partitioned into σ_{dia} and σ_{para} components.[4,5,6] As conventionally partitioned, the paramagnetic shielding term is often the dominant term that contributes to shielding tensor anisotropy.[4,5,6] Consider an occupied MO with strong *p* character and centered on boron. If virtual rotation of this orbital by 90º produces a favorable overlap with a virtual *p* orbital of the boron atom, the situation results in paramagnetic contributions to the component along the axis of virtual rotation.[58] To assist in visualization, consider occupied orbital 33 in Figure 2.26. A 90º rotation about a vertical axis in the plane of the page will yield an orbital orientation that overlaps with (and looks very similar to) virtual orbital 65. Hence, paramagnetic shielding contributions are experienced along this vertical axis in the plane of the page. Consider the action of the angular momentum operator (eq. 10) on a given MO wavefunction that can account for contributions to paramagnetic shielding due to orbital overlap between occupied and virtual states. The action that this angular momentum operator has on a *p*-

character orbital, which is the case for the boron compounds being examined, can be visualized as a 90º rotation of the occupied orbital. If σ_{para} is the dominant contributor to shielding anisotropy, it is anticipated that there should be a relationship between the observed Ω and the MOs involved in mixing. To assist in visualization of this concept, consider the pair of MOs that give the greatest contributions to σ_{para} for compound **6** (Figure 2.26).

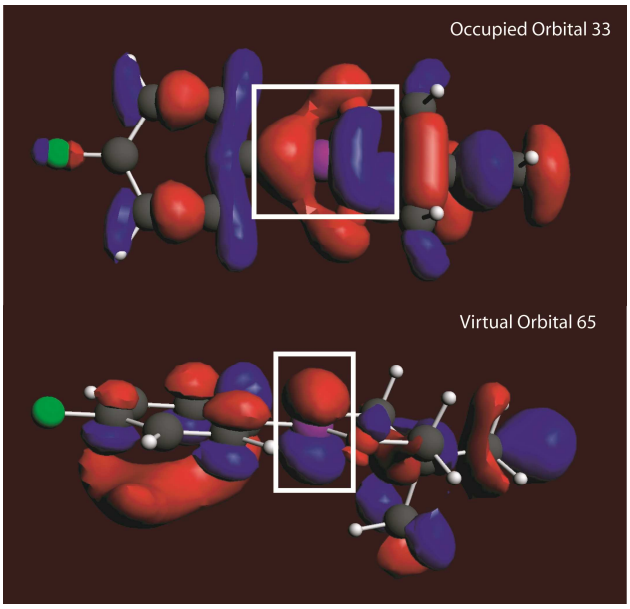

Figure 2.26: Occupied orbital 33 (HOMO -7) and virtual orbital 65 (LUMO +24) for compound **6**. These are the two orbitals involved in mixing which yield the largest contribution to total isotropic σ_{para}. Note the orbital overlap between a 90 degree virtual rotation of occupied orbital 33 out of the plane of the page and virtual orbital 65. This leads to a paramagnetic shielding contribution along the axis of rotation.

When examining the boronic acids and esters, the long axis of the occupied *p*-orbital that has the largest contribution to the total isotropic σ_{para} is always along the shielding tensor component which is coincident with the B-C bond (σ_{11} or σ_{22} except for

compound **4**). For all boronic acids and esters **1** to **10**, the shielding tensor component that is coincident with the axis of virtual rotation of the occupied MO yields the largest contribution to total isotropic σ_{para}.

Interestingly, when considering compounds **1** to **10**, there is no clear correlation between span and orbital energy gap between the occupied and virtual states which give the largest contribution to the total isotropic σ_{para} (Table 2.7). There is also no obvious correlation between the span and total isotropic σ_{para}. From compound to compound, different effects need to be considered, including: hydrogen bonding, ϕ_{CCBO}, and varying electronics of the different substituents on the aromatic ring. It is likely a composite of these different effects that clouds the relationship between Ω and orbital energy gap or total isotropic σ_{para}.

When considering the model phenylboronic acid monomer system, there is a clear correlation between Ω and total isotropic σ_{para} (Table 2.8). In addition, when the same occupied and virtual MOs are considered from compound to compound, as the orbital energy gap decreases, the span values increase, which is the expected correlation when the span is dominated by σ_{para}.

Table 2.7: Calculated magnetic shielding tensor components with the largest contribution to total isotropic σ_{para} for a given set of occupied and virtual MOs for compounds **1** to **10**.[a]

Compound	MOs (OCC-VIR)	σ_{11}[b]	σ_{22}[b]	σ_{33}[b]	σ_{iso}	ΔE	ϕ_{CCBO} / °	Ω / ppm
1	102-201	0	0	-6	-2	0.4615	8.7	25.0
2	43-70	-2	-58	0	-20	0.3156	90.0	41.8
3	42-75	-8	-8	0	-5	0.4240	0.1	27.7
4	45-67	-6	0	-9	-5	0.3377	0.0	23.4
5	49-81	0	-12	0	-4	0.3887	19.9	28.1
6	33-65	0	-16	0	-5	0.4553	0.5	23.9
7	39-74	-17	0	0	-5	0.4379	3.0	11.5
8	39-59	-20	0	0	-7	0.3444	2.9	15.5
9	46-70	-12	0	0	-4	0.3389	1.2	14.0
10	43-60	0	-7	-5	-4	0.3290	61.3	32.3

[a] Calculated boron ϕ_{CCBO}, Ω, shielding tensor components, and energy gap for each pair of occupied and virtual orbitals which have the largest contribution to total isotropic σ_{para} for each boronic acid and ester compound studied. The shielding tensor components are those for the given pair of MOs, and are not the total shielding values. Calculated values for boronic acid dimers which take into account hydrogen bonding interactions are included where applicable. ADF calculations were performed using the GGA revPBE functional and TZP basis set on all atoms.

[b] Contributions (ppm) to shielding tensor principal components for a given pair of MOs which yield the largest contribution to total isotropic paramagnetic shielding.

Table 2.8: Calculated magnetic shielding tensor components with the largest contribution to total isotropic σ_{para} for a given set of occupied and virtual MOs for phenylboronic acid.[a]

Dihedral	MOs (OCC-VIR)	σ_{11}[b]	σ_{22}[b]	σ_{33}[b]	σ_{iso}	ΔE	Ω / ppm
0	21-36	0	-45	0	-15	0.4316	24.39
10	21-36	0	-38	-1	-13	0.4285	25.71
20	21-36	0	-27	-3	-9	0.4215	26.80
30	21-36	0	-18	-3	-7	0.4139	28.69
40	18-58	0	-12	-7	-6	0.6885	31.56
50	9-27	-19	0	0	-6	0.5202	34.33
60	9-27	-26	0	0	-9	0.5165	36.22
70	9-27	-32	0	0	-11	0.5127	37.39
80	9-27	0	-36	0	-12	0.5098	38.01
90	9-27	0	-38	0	-13	0.5087	38.20

[a] Calculated boron ϕ_{CCBO}, Ω, and shielding tensor components and energy gap for each pair of occupied and virtual orbitals which have the largest contribution to total isotropic paramagnetic shielding for phenylboronic acid as the dihedral is varied from 0 to 90 degrees. ADF calculations were performed using the GGA revPBE functional and TZP basis set on all atoms.

[b] Contributions (ppm) to shielding tensor principal components for a given pair of MOs which yield the largest contribution to total isotropic paramagnetic shielding.

Both the paramagnetic shielding tensor components as well as the total magnetic shielding components are plotted against ϕ_{CCBO} in Figure 2.27. As ϕ_{CCBO} increases from 0 to 90°, the separation between σ_{11} and σ_{33} increases, which equates to an increasing span (eq. 7). In the plot where the contributions to paramagnetic shielding are plotted against ϕ_{CCBO}, the paramagnetic contribution to σ_{11} becomes increasingly negative with increasing dihedral while the paramagnetic contribution to σ_{33} also decreases slightly.

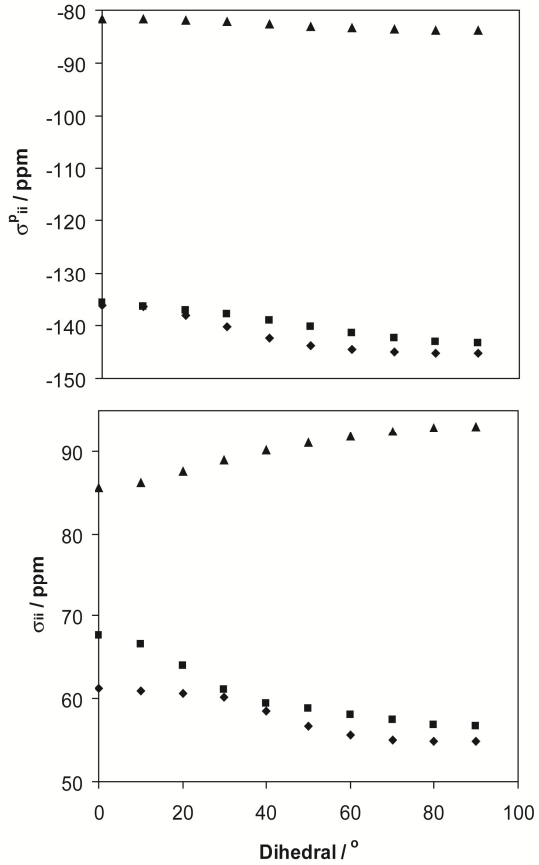

Figure 2.27: Correlation between the ADF/GGA revPBE calculated total magnetic shielding tensor components (bottom), total isotropic σ_{para} tensor components (top) and ϕ_{CCBO} for phenylboronic acid. The three data sets on each plot represent σ_{11} (diamonds),

σ_{22} (squares), and σ_{33} (triangles). Experimental Ω is plotted against the calculated Ω values for the monomer in all cases.

As a consequence of the paramagnetic contribution to σ_{11} becoming increasingly negative, the total isotropic σ_{para} will become more negative and the span will increase. However, a plot of total magnetic shielding against ϕ_{CCBO} reveals that σ_{11} shifts in the negative direction, while σ_{33} becomes more positive as ϕ_{CCBO} increases. Consequently, it is concluded that *diamagnetic* shielding contributions play a non-negligible role in determining the span values observed. Numerical values are tabulated in Tables 2.9 and 2.10. Shown below is a diagram demonstrating the chemical shift tensor components in one of the boronic esters.

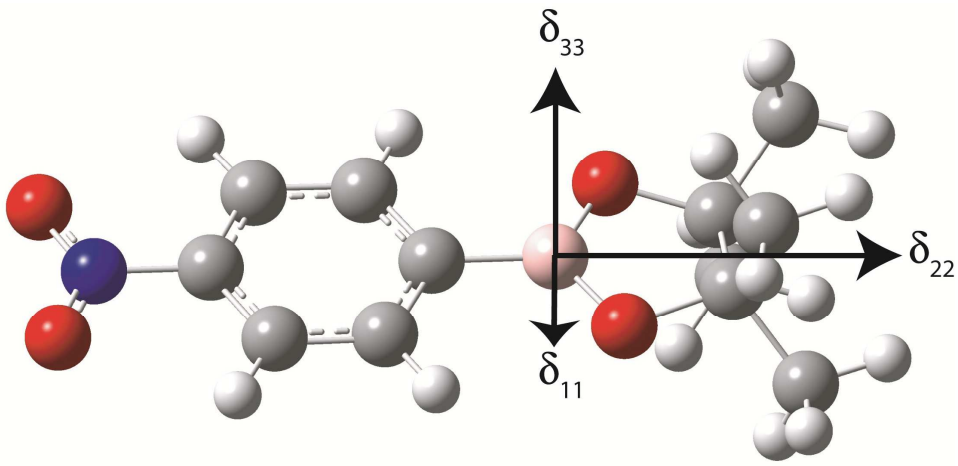

Figure 2.28: A molecular diagram showing the structure of compound **7** as well as the orientations of the chemical shift tensors. δ_{33} and δ_{22} are both in the plane of the page, and δ_{11} is perpendicular to the plane of the page.

Table 2.9: Calculated magnetic shielding tensor components for compounds **1** to **10**.[a]

Boronic Acids	**1**				**2**				**3**				**4**				**5**			
Contribution	σ_{11}	σ_{22}	σ_{33}	σ_{iso}	σ_{11}	σ_{22}	σ_{33}	σ_{iso}	σ_{11}	σ_{22}	σ_{33}	σ_{iso}	σ_{11}	σ_{22}	σ_{33}	σ_{iso}	σ_{11}	σ_{22}	σ_{33}	σ_{iso}
σ^d (Core Density)	163.9	164.1	164.3	164.1	163.4	164.2	164.7	164.1	163.8	164.2	164.4	164.1	163.8	164.2	164.3	164.1	163.8	164.1	164.4	164.1
σ^d (Valence Density)	-0.5	33.6	38.3	23.8	8.5	29.5	34.5	24.2	-0.5	32.8	39.1	23.8	4.2	32.9	40.9	24.6	3.1	34.2	39.6	25.6
σ^d	163.4	197.7	202.6	187.9	171.9	193.7	199.2	188.3	163.3	197.0	203.5	187.9	168.0	197.1	205.2	188.7	166.9	198.3	204	189.8
σ^p (OCC-OCC)	22.9	28.6	162.0	71.2	16.4	62.2	101.6	60.1	10.8	21.0	132.9	54.9	12.3	22.6	138.4	57.8	14.5	19.4	123.7	52.5
σ^p (OCC-VIR)	-307.6	-177.8	-156.6	-214	-273.5	-157.0	-138.2	-189.6	-251.8	-161.9	-138.7	-184.1	-267.3	-163.6	-143.8	-191.5	-248.7	-157.9	-143.7	-183.4
σ^p	-142.0	-128.7	-81.3	-117.4	-143.6	-125.9	-80.0	-116.5	-141.1	-127.6	-79.4	-116.1	-142.3	-125.8	-94.0	-120.7	-141.8	-127.9	-82.4	-117.4
Total	57.5	71.6	82.5	70.6	51.4	70.8	93.2	71.8	56.2	75.6	83.8	71.9	55.4	69.8	78.8	68.0	57.2	74.5	85.3	72.4

*Boronic acid calculations are performed on the dimer

Boronic Esters	**6**				**7**				**8**				**9**				**10**			
Contribution	σ_{11}	σ_{22}	σ_{33}	σ_{iso}	σ_{11}	σ_{22}	σ_{33}	σ_{iso}	σ_{11}	σ_{22}	σ_{33}	σ_{iso}	σ_{11}	σ_{22}	σ_{33}	σ_{iso}	σ_{11}	σ_{22}	σ_{33}	σ_{iso}
σ^d (Core Density)	163.8	164.1	164.4	164.1	163.8	164.1	164.4	164.1	163.8	164.1	164.4	164.1	163.8	164.1	164.4	164.1	163.9	164.1	164.4	164.1
σ^d (Valence Density)	3.0	35.1	40.0	26.0	3.0	36.5	38.1	25.9	2.5	36.5	38.1	25.7	2.7	36.7	37.6	25.7	6.6	34.9	36.0	25.8
σ^d	166.8	199.2	204.4	190.1	166.8	200.6	202.5	190.0	166.3	200.6	202.5	189.8	166.5	200.8	202.0	189.8	170.5	199.0	200.4	190.0
σ^p (OCC-OCC)	24.3	24.7	89.2	46.0	31.2	33.0	96.1	53.4	30.4	33.0	98.7	54.0	31.5	43.3	93.8	56.2	28.8	49.0	87.7	55.2
σ^p (OCC-VIR)	-200.6	-170.4	-161.8	-177.6	-220.7	-189.5	-168.4	-192.9	-226.0	-191.4	-165.4	-194.3	-219.1	-205.9	-167.4	-197.5	-227.9	-182.3	-166.8	-192.3
σ^p	-135.7	-132.7	-79.3	-115.9	-137.2	-133.2	-90.3	-120.2	-142.3	-129.0	-91.0	-120.7	-139.1	-131.4	-90.0	-120.2	-140	-134.1	-79.4	-117.8
Total	63.7	71.4	87.6	74.2	65.1	67.8	76.5	69.8	59.8	71.9	75.4	69.0	62.6	69.7	76.5	69.6	59.9	64.3	92.2	72.1

[a] Calculated boron magnetic shielding tensor components for each boronic acid and ester compound studied. Calculated values for boronic acid dimers which take into account hydrogen bonding interactions were used for **1** to **5**. ADF calculations were performed using the GGA revPBE functional and TZP basis set on all atoms.

Table 2.10: Calculated magnetic shielding tensor components for phenylboronic acid.[a]

Dihedral	0				10				20				30				40			
Contribution	σ_{11}	σ_{22}	σ_{33}	σ_{iso}	σ_{11}	σ_{22}	σ_{33}	σ_{iso}	σ_{11}	σ_{22}	σ_{33}	σ_{iso}	σ_{11}	σ_{22}	σ_{33}	σ_{iso}	σ_{11}	σ_{22}	σ_{33}	σ_{iso}
σ^d (Core Density)	163.9	164.2	164.2	164.1	163.9	164.2	164.3	164.1	163.9	164.2	164.3	164.1	163.9	164.2	164.3	164.1	163.9	164.2	164.3	164.1
σ^d (Valence Density)	3.4	33.1	39.2	25.2	3.7	33.2	39.2	25.3	4.5	33.4	39	25.6	5.8	33.8	38.6	26.1	7.3	34.3	38.1	26.6
σ^d	167.3	197.3	203.4	189.3	167.6	197.4	203.5	189.5	168.4	197.6	203.3	189.8	169.7	198	202.9	190.2	171.2	198.5	202.4	190.7
σ^p (OCC-OCC)	7.7	18.5	33.4	19.9	7.7	18.2	33.3	19.7	7.5	17.3	33.1	19.3	7.3	15.9	32.9	18.7	7.3	14.3	32.7	18.1
σ^p (OCC-VIR)	-154.7	-143.4	-129.5	-142.6	-154.7	-145.3	-128.1	-142.7	-154.4	-149.3	-125.3	-143	-153.9	-153.5	-122.6	-143.4	-157.2	-153.5	-120.5	-143.7
σ^p	-136.2	-135.7	-81.7	-117.9	-136.4	-136.4	-81.7	-118.2	-138.1	-137	-81.9	-119	-140.3	-137.9	-82.2	-120.1	-142.3	-139	-82.6	-121.3
Total	61.2	67.7	85.6	71.5	61	66.6	86.2	71.3	60.7	64	87.5	70.7	60.2	61.1	88.9	70.1	58.5	59.5	90.1	69.4

*Boronic acid calculations are performed on the dimer

Dihedral	50				60				70				80				90			
Contribution	σ_{11}	σ_{22}	σ_{33}	σ_{iso}	σ_{11}	σ_{22}	σ_{33}	σ_{iso}	σ_{11}	σ_{22}	σ_{33}	σ_{iso}	σ_{11}	σ_{22}	σ_{33}	σ_{iso}	σ_{11}	σ_{22}	σ_{33}	σ_{iso}
σ^d (Core Density)	163.9	164.2	164.3	164.1	163.9	164.2	164.3	164.1	163.9	164.2	164.3	164.1	163.9	164.1	164.3	164.1	163.9	164.1	164.3	164.1
σ^d (Valence Density)	8.9	34.7	37.5	27.1	10.4	35.1	36.9	27.5	11.7	35.5	36.3	27.8	12.6	35.7	36	28.1	12.9	35.7	35.8	28.1
σ^d	172.8	198.9	201.8	191.2	174.3	199.3	201.2	191.6	175.6	199.7	200.6	191.9	176.5	199.8	200.3	192.2	176.8	199.8	200.1	192.3
σ^p (OCC-OCC)	7.3	12.6	32.5	17.5	7.4	11.1	32.4	17	7.5	10	32.3	16.6	7.6	9.3	32.2	16.4	7.7	9.1	32.2	16.3
σ^p (OCC-VIR)	-159.9	-153.1	-118.8	-143.9	-161.7	-152.8	-117.6	-144	-162.9	-152.7	-116.9	-144.1	-163.5	-152.6	-116.4	-144.2	-163.6	-152.6	-116.2	-144.2
σ^p	-143.7	-140.2	-83	-122.3	-144.6	-141.4	-83.4	-123.1	-145	-142.4	-83.6	-123.7	-145.2	-143	-83.8	-124	-145.2	-143.3	-83.8	-124.1
Total	56.7	58.8	91	68.8	55.6	58	91.8	68.5	55	57.4	92.4	68.3	54.8	56.9	92.8	68.2	54.8	56.7	93	68.2

[a] Calculated boron magnetic shielding tensor components for phenylboronic acid as ϕ_{CCBO} is varied from 0 to 90 degrees. ADF calculations were performed using the GGA revPBE functional and TZP basis set on all atoms.

2.2.4 Effect of Substituents

Due to the demonstrated importance of diamagnetic shielding, a brief study was conducted to determine the effects of strong and mild electron-donating and withdrawing groups on the boron shielding tensor. Phenylboronic acid was used as a control molecule, and a steric group (bromine), a mild electron-donating group (carboxylic acid ester), a strong electron-donating group (amine), a mild electron-withdrawing group (carboxyl), and a strong electron-withdrawing group (nitro) were each substituted in the ortho, meta, and para positions of the aromatic ring. Data are found in Table 2.11.

Table 2.11: Calculated Ω and magnetic shielding tensor components for a series of steric, electron donating, and electron withdrawing groups substituted on phenylboronic acid.[a]

Compound[b]	σ_{11}[d]	σ_{22}[d]	σ_{33}[d]	Total σ_{para}	σ_{11}	σ_{22}	σ_{33}	Total σ_{iso}	Ω / ppm
phenylboronic acid	-136.2	-135.7	-81.7	-117.9	61.2	67.7	85.6	71.5	24.4
o-steric	-138.9	-132.2	-81.5	-117.5	58.7	72.4	85.4	72.2	26.7
m-steric	-136.3	-134.4	-80.9	-117.2	60.4	69.8	85.8	72.0	25.4
p-steric	-136.8	-134.4	-81.2	-117.5	61.0	68.8	85.7	71.8	24.7
mild o-EWG	-140.2	-138.4	-83.2	-120.6	56.1	58.3	93.9	69.4	37.9
mild m-EWG	-137.1	-133.4	-81.3	-117.3	60.1	70.1	85.3	71.8	25.3
mild p-EWG	-137.9	-132.7	-81.6	-117.4	59.7	70.5	85.4	71.9	25.7
strong o-EWG	-140.4	-133.7	-83.9	-119.3	56.4	63.2	92.6	70.7	36.2
strong m-EWG	-139.6	-132.5	-95.6	-122.6	55.3	60.1	92.8	69.4	37.5
strong p-EWG	-144.8	-140.7	-83.2	-122.9	55.3	58.7	93.1	69.1	37.8
mild o-EDG	-136.0	-133.4	-80.6	-116.7	59.5	70.5	86.4	72.2	27.0
mild m-EDG	-135.9	-133.6	-81.8	-117.1	59.9	70.3	85.8	72.0	25.8
mild p-EDG	-136.6	-133.1	-81.9	-117.2	60.7	69.8	85.6	72.0	24.9
strong o-EDG	-140.7	-132.4	-82.9	-118.7	61.4	66.1	84.6	70.7	23.2
strong m-EDG	-136.8	-135.3	-81.3	-117.8	61.9	66.8	85.7	71.4	23.7
strong p-EDG	-137.8	-133.8	-81.6	-117.7	63.9	65.7	85.6	71.8	21.7

Compound[c]	σ_{11}[d]	σ_{22}[d]	σ_{33}[d]	Total σ_{para}	σ_{11}	σ_{22}	σ_{33}	Total σ_{iso}	Ω / ppm
phenylboronic acid	-136.2	-135.7	-81.7	-117.9	61.2	67.7	85.6	71.5	24.4
o-steric	-137.8	-134.1	-81.6	-117.8	58.9	71.6	84.9	71.8	26.1
m-steric	-136.6	-134.8	-81.1	-117.5	60.5	69.0	85.6	71.7	25.1
p-steric	-136.7	-134.8	-81.3	-117.6	61.2	68.2	85.5	71.6	24.4
mild o-EWG	-136.5	-135.4	-81.3	-117.7	59.5	70.2	85.6	71.8	26.0
mild m-EWG	-137.1	-133.8	-81.4	-117.4	60.2	69.4	85.1	71.6	25.0
mild p-EWG	-137.9	-133.1	-81.7	-117.6	59.8	69.8	85.2	71.6	25.4
strong o-EWG	-137.2	-133.9	-80.1	-117.1	58.5	71.9	86.7	72.4	28.2
strong m-EWG	-136.8	-133.9	-81.0	-117.3	59.6	70.2	85.7	71.8	26.0
strong p-EWG	-137.8	-132.6	-81.3	-117.2	59.9	70.3	85.6	71.9	25.6
mild o-EDG	-134.8	-133.9	-81.8	-116.8	59.7	70.3	85.7	71.9	26.0
mild m-EDG	-136.1	-134.0	-82.0	-117.4	60.0	69.5	85.6	71.7	25.6
mild p-EDG	-136.4	-133.5	-82.1	-117.3	60.8	69.2	85.4	71.8	24.6
strong o-EDG	-140.9	-132.2	-82.1	-118.4	61.9	66.3	84.5	70.9	22.7
strong m-EDG	-136.3	-135.2	-81.3	-117.6	61.2	67.8	85.5	71.5	24.3
strong p-EDG	-135.9	-135.5	-81.8	-117.7	61.7	67.7	85.3	71.6	23.6

[a] Calculated boron Ω and magnetic shielding tensor components for substituted phenylboronic acid. ADF calculations were performed using the GGA revPBE functional and TZP basis set on all atoms. Bromine was used as a steric group, carboxyl as a mild electron withdrawing group, nitro as a strong electron withdrawing group,

carboxylic acid ester as a mild electron donating group, and amine as a strong electron donating group.

[b] Phenylboronic acid structure has been fully optimized.

[c] Phenylboronic acid structure has ϕ_{CCBO} fixed at 0 degrees.

[d] Shielding tensor component which contributes to total isotropic paramagnetic shielding.

While changes in the isotropic shielding constant are small for all substituents, it was found that the presence of electron-withdrawing groups correlates with increases in the calculated Ω values (up to 13.5 ppm), while electron-donating groups have less of an effect on the calculated Ω values. For both shifts in σ_{11} in the negative direction which increase Ω, and shifts in σ_{11} in the positive direction which decrease Ω, in general, it was σ_{11} which had the largest change in magnitude as a result of substitution. These results are logical because tricoordinate boron compounds that feature boron atoms bound to multiple oxygen atoms have smaller observed Ω values due to the lone pairs on the oxygen donating electron density to a virtual MO centred on the boron atom.[58]

In this chapter, a series of ten boronic acid and boronic esters were studied by SSNMR, simulated, and their NMR parameters calculated at various levels of theory. It has been shown that the span is the most characteristic NMR parameter. Molecular orbital (MO) analysis can be used to relate span, total isotropic paramagnetic shielding, and energy gap in phenylboronic acid – a model system. In the case of compounds **1** – **10**, span can be related to the dihedral angle on the relative MO orientations. The effects of various substituents were studied, and a detailed analysis of magnetic shielding tensor components was performed.

2.3 Experimental

Solid-State NMR Spectroscopy

400 MHz Data: The five boronic acids (2-(tert-butyldimethylsilyloxy)naphthalene-6-boronic acid (**1**), 2,6-dibromophenylboronic acid (**2**), 2-chloropyridine-3-boronic acid (**3**), 2-(hydroxymethyl)phenylboronic acid cyclic monoester (**4**), and 2-acetyl-3-thiopheneboronic acid (**5**)), and five boronic esters (4-fluorophenylboronic acid neopentylglycol ester (**6**), 4-nitrophenylboronic acid pinacol ester (**7**), 1H-indazole-5-boronic acid pinacol ester (**8**), 4-(2-propynylcarbamoyl)phenylboronic acid pinacol ester (**9**), and 2,4,6-trimethoxyphenylboronic acid neopentyl glycol ester (**10**)) in this study (Figure 2.1) were purchased from Aldrich and used without further purification. The manufacturer performed various analytical techniques on all of the compounds studied in this chapter to verify purity. These techniques include solution state ^{1}H and ^{13}C NMR, infrared spectroscopy, and elemental analysis. Melting point analysis was also performed by the manufacturer, and the specified melting points were verified. Samples were powdered and packed in a glovebox under an inert atmosphere of nitrogen into 4 mm o.d. ZrO_2 rotors, and NMR experiments were conducted using a Bruker AvanceIII NMR spectrometer ($\mathbf{B}_0$ = 9.40 T, $\nu_L(^{11}B)$ = 128.38 MHz). Spectra were acquired using TopSpin 2.0 software. A Bruker 4.0 mm HXY triple-resonance MAS probe tuned to ^{11}B on the X channel was used. Experimental referencing, calibration, and setup were done using solid powdered sodium borohydride. Solid $NaBH_4$ has a chemical shift of -42.06 ppm relative to the primary standard, liquid $F_3B{\bullet}O(C_2H_5)_2$ (where $\delta(^{11}B)$ = 0.00 ppm).[63] For both MAS and stationary samples, the Hahn echo ($\pi/2$ - τ_1 - π - τ_2 - ACQ)[64,65] pulse

sequence was used. MAS spinning frequencies ranged from 12 to 15 kHz. Typical $\pi/2$ pulse lengths for solid $NaBH_4$ were ~3.0 μs. For the ten samples under study, the "solid $\pi/2$" pulse was used (e.g., 3.0 μs/(I + 1/2) = 1.5 μs, where I = 3/2 for ^{11}B). Recycle delays of 2 to 120 s were employed. Signal averaging was carried out over a period of 4 min to 4 h for both static and MAS samples. Proton decoupling was applied during acquisition of the spectra of stationary samples. The probes used at both fields exhibit a small, but manageable background ^{11}B signal in the acquired spectra, as a result of boron nitride in the stators. The Hahn echo pulse sequence was generally found to be effective at suppressing the background signal.

900 MHz Data: Samples were powdered and packed in a glovebox under a dry argon atmosphere into 2.5 mm o.d. ZrO_2 rotors, and NMR experiments were conducted using a Bruker AvanceII NMR spectrometer ($\mathbf{B}_0$ = 21.1 T, $\nu_L(^{11}B)$ = 288.80 MHz). Spectra were acquired using TopSpin 1.3 software at the National Ultrahigh-Field NMR Facility for Solids in Ottawa (www.nmr900.ca). A Bruker 2.5 mm HX MAS VT probe tuned to ^{11}B on the X channel was used. The referencing, calibration, and setup procedures were identical, and the pulse sequences, pulse widths, pulse delays and experiment times were similar to those used at 9.40 T. The MAS speed was 30 kHz. All MAS samples were cooled to room temperature using a VT unit to prevent sample decomposition caused by heat production at fast spinning speeds.

Spectral Processing and Simulation: Data were processed using TopSpin 2.0. FIDs were left-shifted to the echo maxima when necessary, apodized using a Gaussian function of 5-25 Hz for MAS samples and 20-200 Hz for stationary samples, and Fourier transformed. Stack plots were produced with DMFit.[66] Spectral simulations were

performed using the WSolids1 program[67] which incorporates the space-tiling algorithm of Alderman et al.[68] The error associated with spectral parameters was determined heuristically by analyzing the spectra (MAS and static echo) obtained at both magnetic fields. In simulations, error was estimated by altering each NMR parameter individually from the optimum value until there was a noticeable discrepancy in the experimental spectrum, and discontinuities were varied until deviation from the experimental spectrum was observed. Of the compounds studied, an X-ray crystal structure is available for compound **4**[59] only; this structure indicates a single crystallographically unique boron site. NMR spectra acquired presently strongly suggest that there is a single unique boron site for all other compounds studied as well. As such, all spectra were simulated using a single boron site for each compound. In some cases, boric acid or other decomposition products were simulated as an additional boron site.

Quantum Chemical Calculations

A model for each compound was generated using standard bond lengths in Gaussview '03. These structures were then subjected to geometry optimization using the B3LYP hybrid DFT functional ('B3LYP')[69] and the 6-311+G* basis set for all atoms, while keeping the coordinates of the carbon and hydrogen atoms in the aromatic ring system frozen so as to not perturb the planarity of the aromatic system and to assist in convergence. On the resulting optimized structure, B3LYP was then used to perform an unrestrained second geometry optimization using the 6-311+G* basis set. These optimized structures were subjected to further NMR calculations. Dihedral angles (ϕ_{CCBO}) of interest were altered simply by defining a new ϕ_{CCBO} in Gaussview '03 for the

optimized structure. Although the crystal structure for phenylboronic acid has been reported,[70] geometry optimizations were performed in order to systematically vary ϕ_{CCBO}. These computations were performed to isolate the impact of varying ϕ_{CCBO} on the boron magnetic shielding tensor. EFG and $\boldsymbol{\sigma}$ tensors were calculated using Gaussian 03[71] running on an in-house 304 CPU system, and the Amsterdam Density Functional package[72] (ADF) running on the High Performance Computing Virtual Laboratory (www.hpcvl.org) cluster. DFT calculations employing B3LYP[69] used the 6-311+G* basis set on all atoms. RHF calculations were also carried out using the same basis set. Finally, magnetic shielding, EFG, and MO analysis calculations using ADF employing the GGA-revPBE DFT method ('GGA-revPBE') were carried out using the TZP basis set on all atoms.

Boron-11 quadrupolar coupling constants were calculated from the largest principal component of the EFG tensor, V_{33}, using eq 5. Calculated NMR parameters were parsed using EFGShield.[9] The factor 9.7177 x 10^{21} V m^{-2} per atomic unit is used to convert V_{33} from atomic units to V m^{-2}.[73]

Chapter 3

Signal Enhancement Using Double Frequency Sweeps and the Quadrupolar Carr-Purcell-Meiboom-Gill Pulse Sequence

3.1 Introduction

The effectiveness of modified-QCPMG[74] and DFS-modified-QCPMG[75,76] signal enhancement techniques for boronic acids and esters are discussed in the following section. The FID produced via QCPMG consists of a pulse train series of echoes. The Fourier transform of this FID produces a spectrum consisting of a manifold of spikelets which are separated by $(2\tau)^{-1}$. The QCPMG pulse sequence is similar to the Hahn-echo pulse sequence, as shown in Figure 3.1, except a refocusing pulse is applied N times after the original echo.[76]

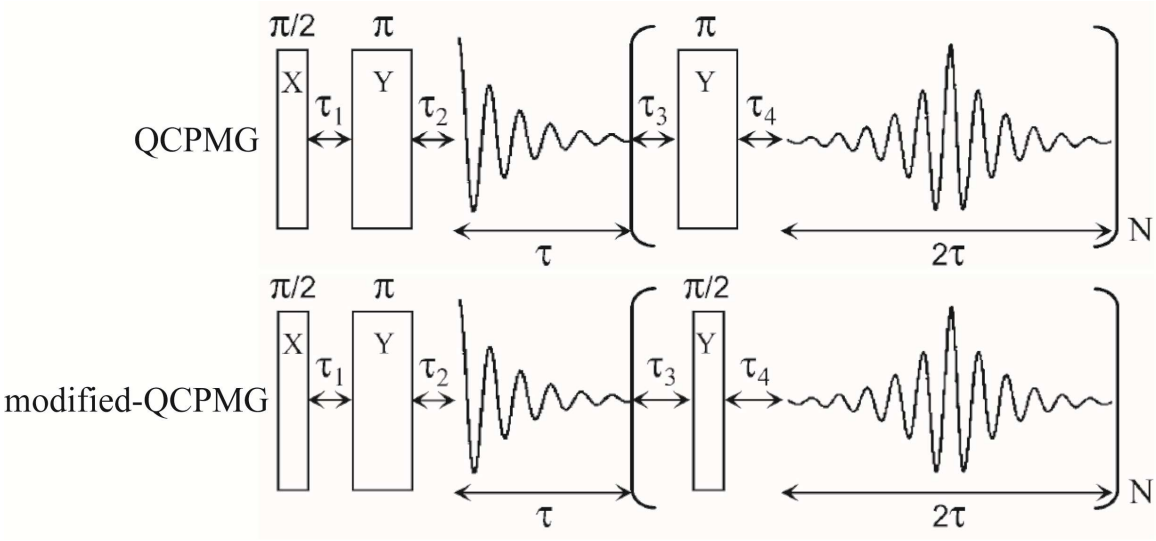

Figure 3.1: A graphical illustration depicting the QCPMG pulse sequence. Note that in the modified-QCPMG pulse sequence, the π refocusing pulse in the echo train has been replaced with a π/2 pulse. Reproduced from reference 76.

The sequence suppresses homonuclear dipolar coupling, hence a longer effective T_2 is observed, allowing more echoes in the echo train to be acquired in the time-domain, resulting in sharper spikelets in the frequency-domain.[77] The signal enhancement can be explained by considering that the observed NMR signal is being split into separate spikelets. Modified-QCPMG is similar to the conventional QCPMG pulse sequence, except that the π pulses in the QCPMG echo train are replaced with $\pi/2$ pulses.[74] The modified pulse sequence produces narrower spikelets and is more effective at suppressing homonuclear dipolar coupling.[77] Since this method is more sensitive, increased signal enhancement is achieved and can be further amplified when it is used in conjunction with DFS.

DFS is a time-dependant amplitude modulated radio frequency sweep which inverts the populations of the STs simultaneously. This RF sweep is depicted below in Figure 3.2.[77]

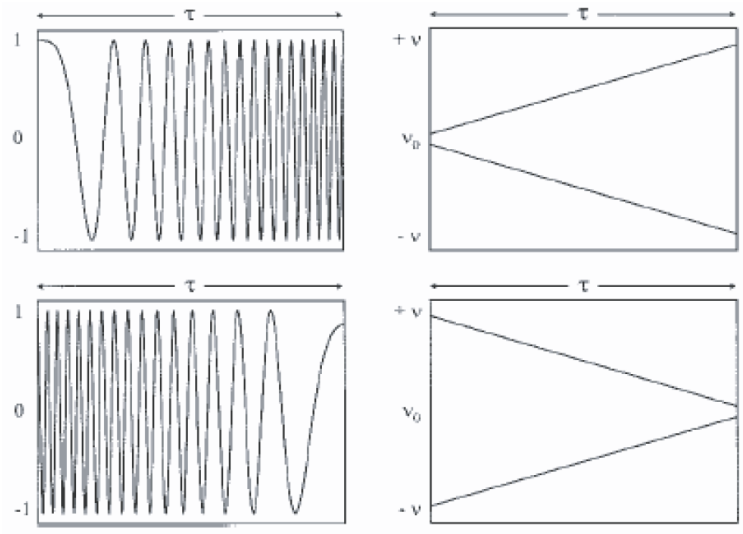

Figure 3.2: A graphical illustration of a double frequency sweep in the time domain. The amplitude profile is shown on the left, and the corresponding frequency sweep is shown in the right. The high and low frequency sides of the CT are swept simultaneously. A

diverging pulse is applied far from the CT and a converging pulse is applied near the CT. τ represents the duration of the sweep. Reproduced from reference 77.

It is these sweeps which lead to population transfer to the central transition and hence signal enhancement. This is achieved by producing a greater population difference between the two spin states in the central transition. This population inversion can be seen in Figure 3.3. The theoretical signal enhancement factor is 2*I*, where *I* represents the spin of the nucleus.[77] To observe a 2*I* enhancement factor, there needs to be uniform excitation, and all of the STs must simultaneously be inverted. Since boron-11 is spin 3/2, the theoretical signal enhancement factor is 3. An example from the literature of such signal enhancement is shown in Figure 3.4.[76]

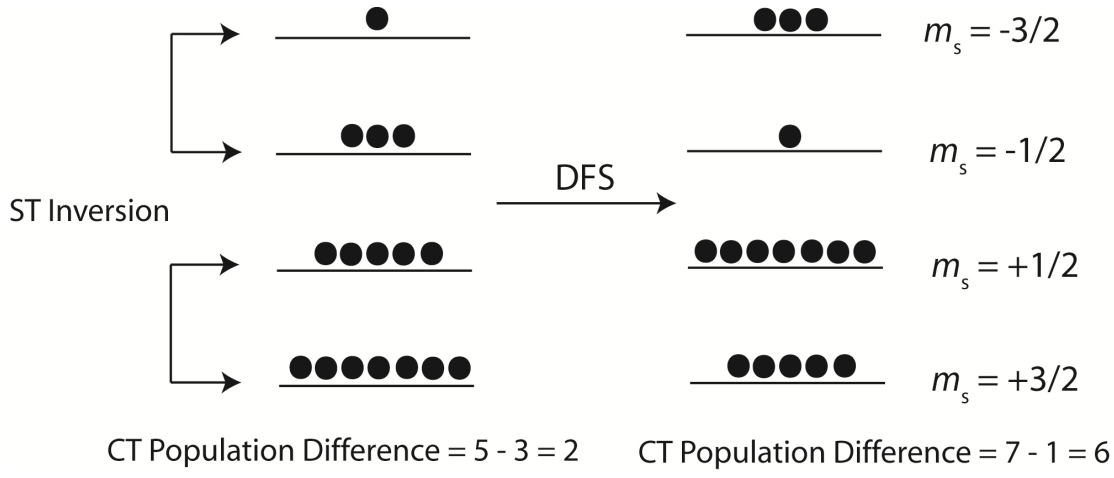

Figure 3.3: An illustration of how signal enhancement is achieved using DFS. DFS causes a simultaneous inversion of the ST which will give a larger population difference in the CT. This increased net magnetization leads to increased signal enhancement.

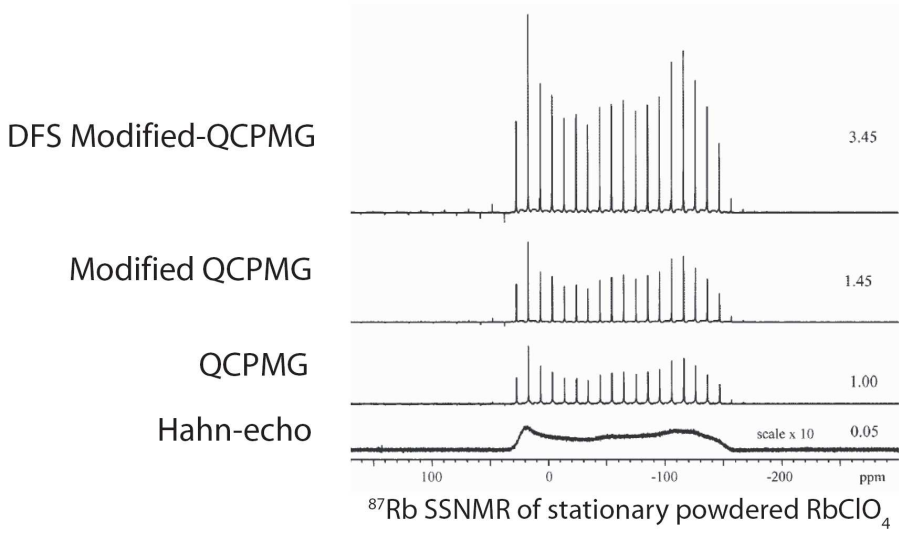

Figure 3.4: An ^{87}Rb QCPMG SSNMR spectrum of $RbClO_4$. The static Hahn-echo spectrum is shown alongside various QCPMG spectra. Significant signal enhancement is noted when modified-QCPMG is applied, and even more signal can be acquired when a DFS shaped pulse is used in addition to QCPMG. Signal enhancement factors are shown to the right of each spectrum. Reproduced from reference 76.

Such a technique is advantageous because more signal can be collected in fewer scans. It is postulated that this sequence could be beneficial due to the large magnetogyric ratio and natural abundance of ^{11}B.

3.2 Results and Discussion

Shown in Figure 3.5 are QCPMG, modified-QCPMG, and DFS modified-QCPMG NMR spectra for a representative boronic ester (**9**), where signal enhancement factors for the modified-QCPMG and DFS modified-QCPMG spectra relative to the QCPMG spectrum are shown.

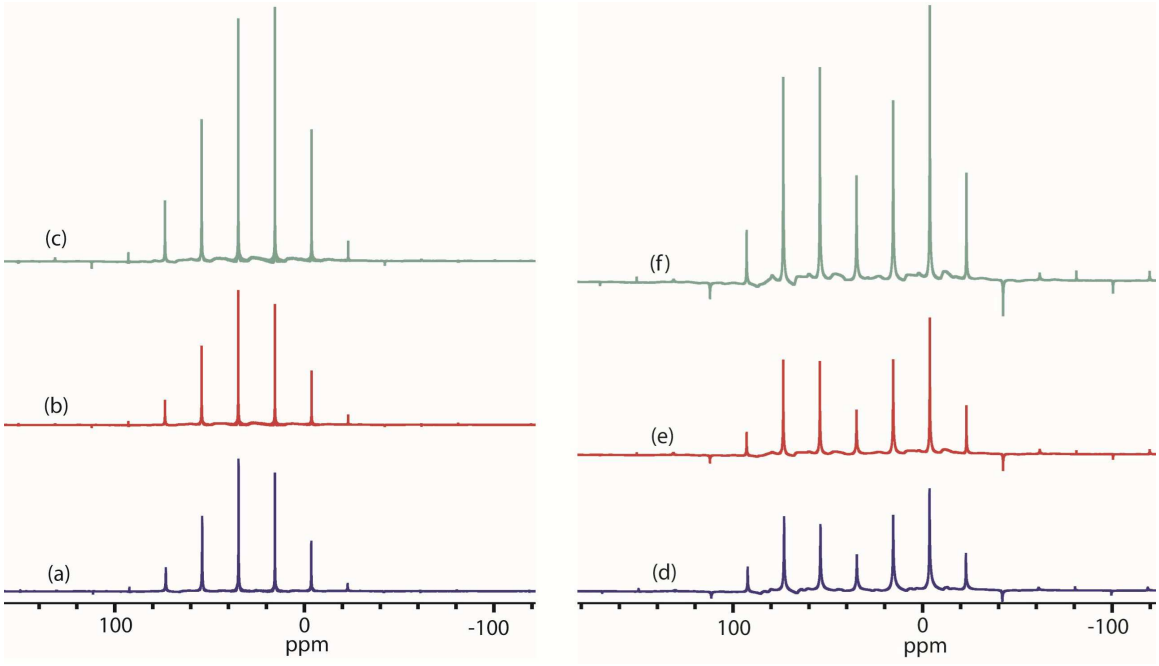

Figure 3.5: Solid-state boron-11 NMR spectroscopy of **9** (left) and **3** (right). Experimental ^{11}B spectra of stationary powdered samples at 9.40 T are shown in (a) and (d) using the QCPMG pulse sequence, (b) and (e) using the modified-QCPMG pulse sequence with a signal enhancement factor of 1.04 and 1.35 respectively, and (c) and (f) using the DFS modified-QCPMG pulse sequence with a signal enhancement factor of 2.16 and 2.71 respectively, relative to QCPMG. Spikelets are separated by 2500 Hz.

Figure 3.5 also presents analogous data for a representative boronic acid (**3**). Further examples of signal enhancement for additional boronic acids and esters may be found in the following figures. The QCPMG, modified-QCPMG, and DFS modified-QCPMG pulse sequences were applied to the following samples, and signal enhancement was successfully achieved in all cases to varying degrees.

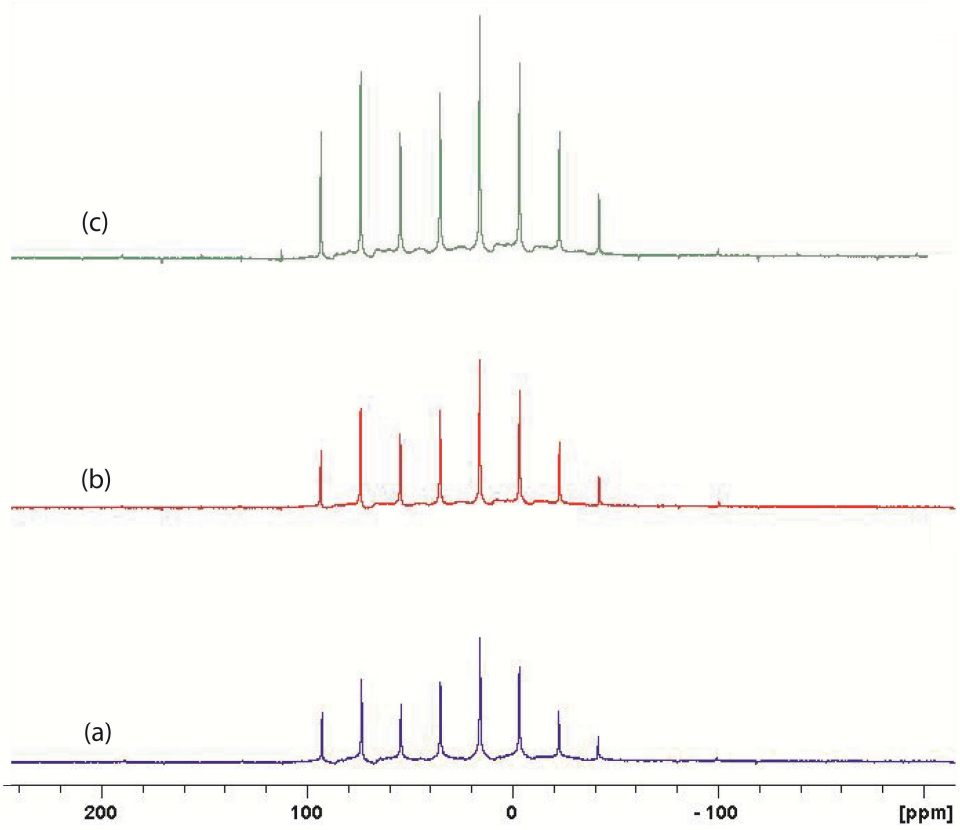

Figure 3.6: Solid-state boron-11 NMR spectroscopy of **1**. Experimental ^{11}B spectra of stationary powdered samples at 9.40 T are shown in (a) using the QCPMG pulse sequence, (b) using the modified-QCPMG pulse sequence with a signal enhancement factor of 1.18, and (c) using the DFS modified-QCPMG pulse sequence with a signal enhancement factor of 1.96 relative to QCPMG. Spikelets are separated by 2500 Hz.

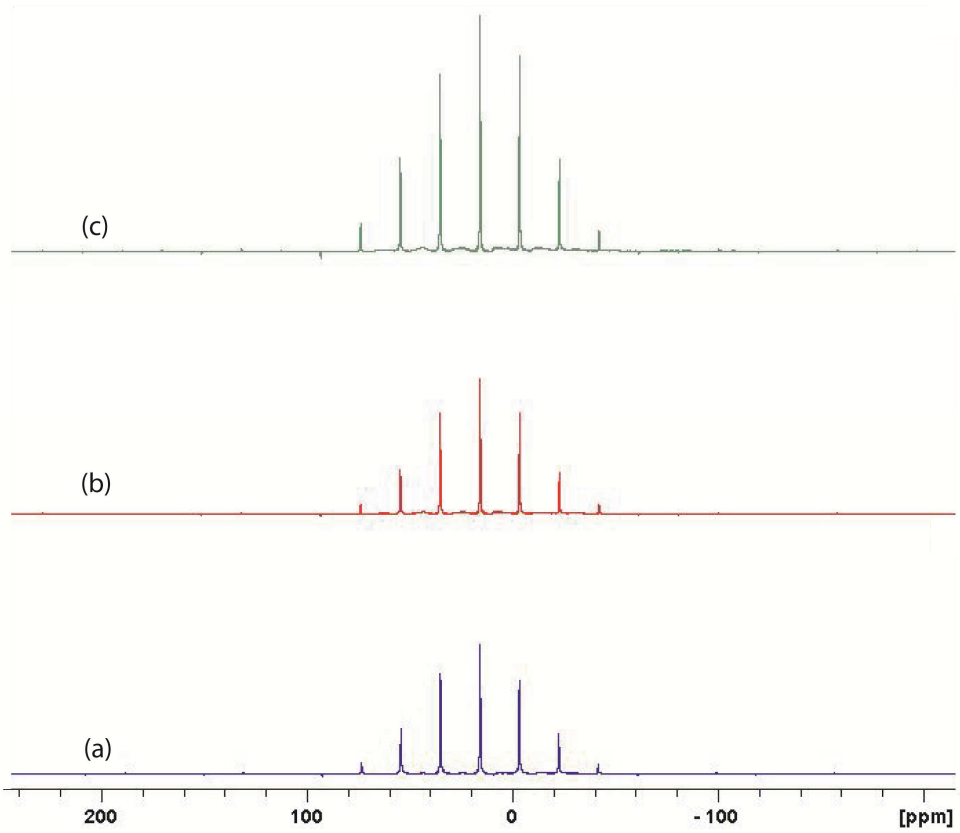

Figure 3.7: Solid-state boron-11 NMR spectroscopy of **2**. Experimental ^{11}B spectra of stationary powdered samples at 9.40 T are shown in (a) using the QCPMG pulse sequence, (b) using the modified-QCPMG pulse sequence with a signal enhancement factor of 1.05, and (c) using the DFS modified-QCPMG pulse sequence with a signal enhancement factor of 1.85 relative to QCPMG. Spikelets are separated by 2500 Hz.

Presently, the modified-QCPMG pulse sequence results in signal enhancement factors ranging from 1.04 in compound **9** to 1.42 in compound **5**, relative to the standard QCPMG pulse sequence. Similarly, the DFS modified-QCPMG pulse sequence provides signal enhancement factors ranging from 1.80 in compound **8** to a high of 2.95 in compound **5**, relative to the standard QCPMG pulse sequence. The signal enhancement factors were measured by comparing the relative intensities of the most intense peak. Namely, the less intense spectrum was overlaid on top of the more intense spectrum. The less intense spectrum was increased in magnitude until its most intense peak became the same height as the most intense peak in the more intense spectrum. The factor by which the magnitude of the less intense spectrum had to be increased to match the more intense spectrum is represented by the signal enhancement factor.

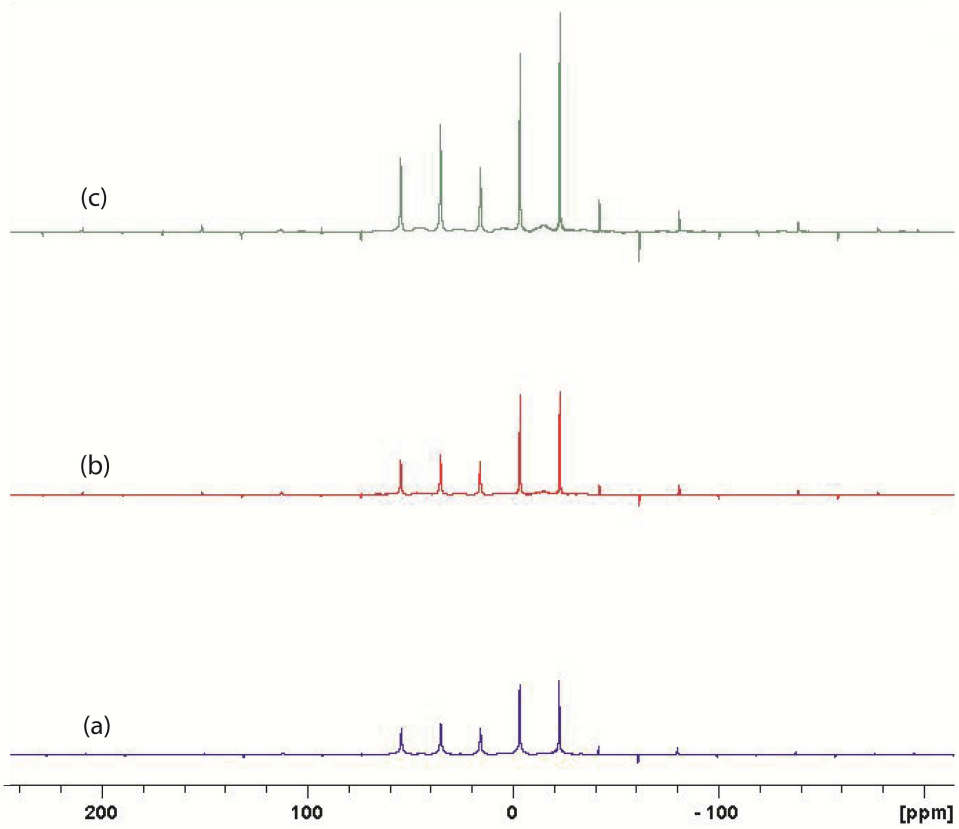

Figure 3.8: Solid-state boron-11 NMR spectroscopy of **5**. Experimental ^{11}B spectra of stationary powdered samples at 9.40 T are shown in (a) using the QCPMG pulse sequence, (b) using the modified-QCPMG pulse sequence with a signal enhancement factor of 1.42, and (c) using the DFS modified-QCPMG pulse sequence with a signal enhancement factor of 2.95 relative to QCPMG. Spikelets are separated by 2500 Hz.

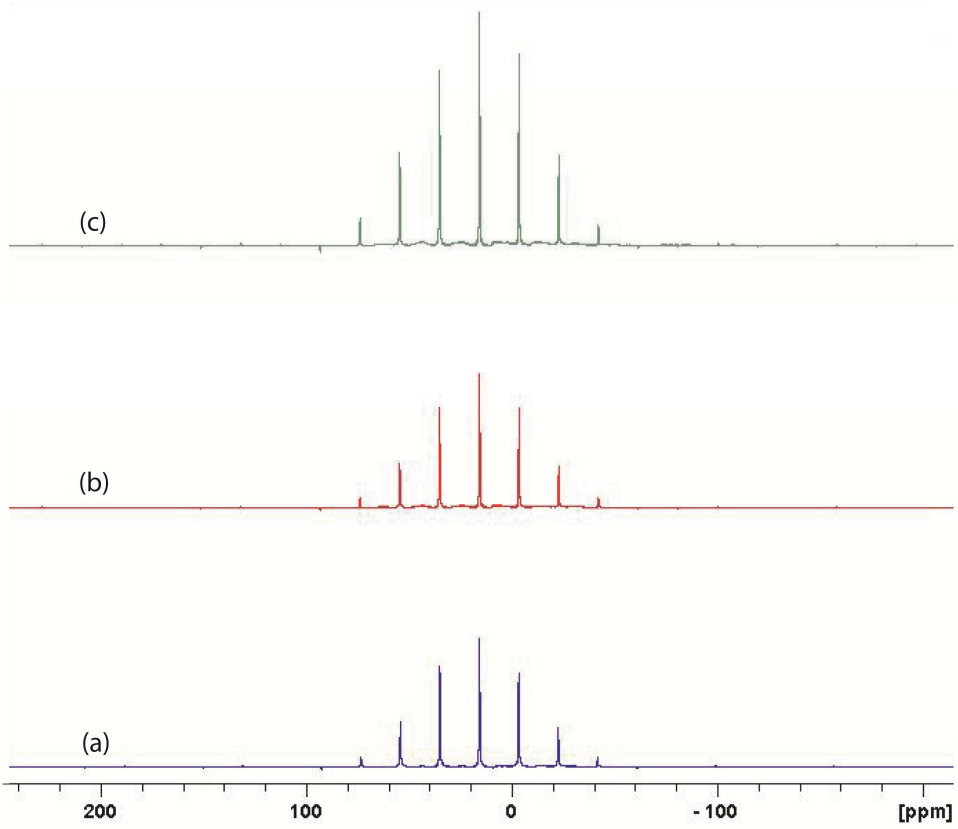

Figure 3.9: Solid-state boron-11 NMR spectroscopy of **8**. Experimental ^{11}B spectra of stationary powdered samples at 9.40 T are shown in (a) using the QCPMG pulse sequence, (b) using the modified-QCPMG pulse sequence with a signal enhancement factor of 1.05, and (c) using the DFS modified-QCPMG pulse sequence with a signal enhancement factor of 1.80 relative to QCPMG. Spikelets are separated by 2500 Hz.

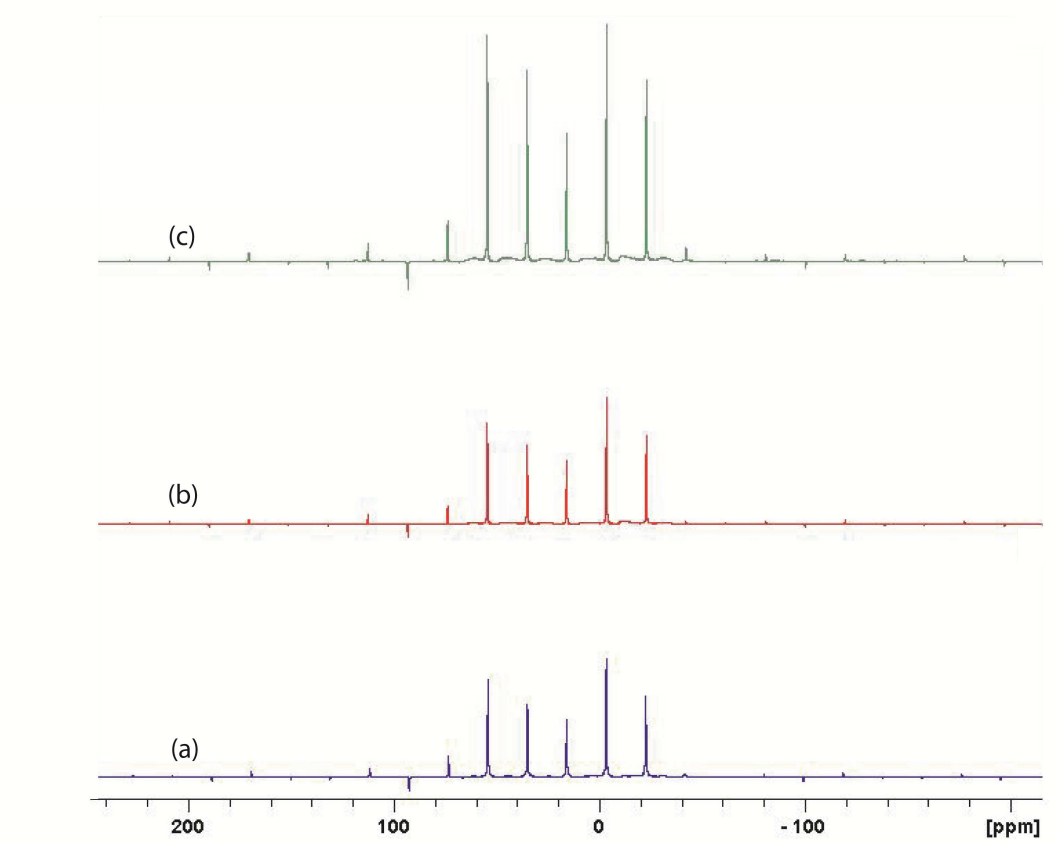

Figure 3.10: Solid-state boron-11 NMR spectroscopy of **10**. Experimental ^{11}B spectra of stationary powdered samples at 9.40 T are shown in (a) using the QCPMG pulse sequence, (b) using the modified-QCPMG pulse sequence with a signal enhancement factor of 1.09, and (c) using the DFS modified-QCPMG pulse sequence with a signal enhancement factor of 2.04 relative to QCPMG. Spikelets are separated by 2500 Hz.

Although high-quality ^{11}B SSNMR spectra were acquired without the use of these signal enhancement techniques in the present study, it is worth noting that they were successful and that they might be useful for ^{11}B SSNMR in more dilute systems.[33,78] One specific example could involve achieving signal enhancement of the ^{11}B CT of boronic acids present in dilute quantities in systems such as modified protease inhibitors.[32]

QCPMG, modified-QCPMG, and DFS modified-QCPMG spectra analogous to all of those shown above were acquired with different spikelet separations, ν_{CPMG}. Figures 3.5 to 3.10 show spectra where ν_{CPMG} = 2500 Hz. Spectra were also acquired for ν_{CPMG} = 1000 Hz and ν_{CPMG} = 500 Hz. These spectra are not shown simply because they are similar to those shown in Figures 3.5 – 3.10. As with all QCPMG spectra, their lineshapes mimicked the lineshape of the static spectra for all values of ν_{CPMG}. Consider a situation where two QCPMG spectra with different ν_{CPMG} values are acquired for the same compound. The spectrum with the lower ν_{CPMG} value will contain more spikelets simply because the spacing is smaller and they are more close together. This spectrum will also yield spikelets of lower intensity than the spectrum with a larger ν_{CPMG} value. The total integrated intensity of all the spikelets remains constant between the two spectra; however, because the spectrum with a smaller ν_{CPMG} value has more spikelets, the total integrated intensity is spread out over more spikelets. The spectrum with the larger ν_{CPMG} value has the same total integrated intensity spread out over fewer spikelets; hence they will be taller and more intense.

QCPMG is an efficient signal enhancement technique, and in the case of the five compounds studied here, the signal enhancement was almost always uniform amongst all of the spikelets within a given spectrum. This is to be expected since the overall

lineshape and ν_{CPMG} are not changing. This feature is especially important if the QCPMG spectra are being used to simulate the static lineshape and extract NMR parameters. If the signal enhancement was not uniform, this would lead to distortions in the horns and discontinuities of the simulated static spectrum.

QCPMG spectra can be useful for extracting NMR parameters. As previously mentioned, the pattern formed by the spikelets mimic the lineshape of the static spectrum. So, using NMR spectrum simulation software, one could simulate the lineshape of the QCPMG spectrum as though it were a static spectrum. This technique is extremely useful under any circumstance where signal enhancement is required. If, for example, a particular nucleus which has a low natural abundance is being observed, this signal enhancement technique would be beneficial in providing more signal in fewer scans. This, of course means less time spent acquiring spectra on the spectrometer.

Both DFS and QCPMG spectra were acquired for five compounds in this chapter and signal enhancement was achieved in all cases. Such signal enhancement techniques are extremely useful for acquiring more signal in fewer scans and can be an important tool when studying dilute systems. Not only can QCPMG provide signal enhancement in situations where the signal to noise is low, but it is also useful in serving as a basis to extract NMR parameters including information about the quadrupolar interaction and CSA.

3.3 Experimental

Solid-State NMR Spectroscopy

400 MHz Data: Four boronic acids (2-(tert-butyldimethylsilyloxy)naphthalene-6-boronic acid (**1**), 2,6-dibromophenylboronic acid (**2**), 2-chloropyridine-3-boronic acid (**3**), and 2-acetyl-3-thiopheneboronic acid (**5**)), and three boronic esters 1H-indazole-5-boronic acid pinacol ester (**8**), 4-(2-propynylcarbamoyl)phenylboronic acid pinacol ester (**9**), and 2,4,6-trimethoxyphenylboronic acid neopentyl glycol ester (**10**)) in this study (Figure 2.1) were purchased from Aldrich and used without further purification. Samples were powdered and packed in a glovebox under an inert atmosphere of nitrogen into 4 mm o.d. ZrO_2 rotors, and NMR experiments were conducted using a Bruker AvanceIII NMR spectrometer ($\mathbf{B}_0$ = 9.40 T, $\nu_L(^{11}B)$ = 128.38 MHz). Spectra were acquired using TopSpin 2.0 software. A Bruker 4.0 mm HXY triple-resonance MAS probe tuned to ^{11}B on the X channel was used. Experimental referencing, calibration, and setup were done using solid powdered sodium borohydride. Solid $NaBH_4$ has a chemical shift of -42.06 ppm relative to the primary standard, liquid $F_3B{\bullet}O(C_2H_5)_2$ (where $\delta(^{11}B)$ = 0.00 ppm).[63] For these stationary samples, the QCPMG ($\pi/2$ - τ_1 - π -τ_2 – ACQ (τ) - [τ_3 - π - τ_4 – ACQ (2τ)]$_N$)[79] pulse sequence was used. Typical $\pi/2$ pulse lengths for solid $NaBH_4$ were ~3.0 μs. For the seven samples to which signal enhancement techniques were applied, the "solid $\pi/2$" pulse was used (e.g., 3.0 μs/(I + 1/2) = 1.5 μs, where I = 3/2 for ^{11}B). Recycle delays of 2 to 120 s were employed. Signal averaging was carried out over a period of 4 min to 4 h for all static samples. Proton decoupling was applied during acquisition of the spectra of these stationary samples. The number of full echoes acquired (N) depended on the transverse (spin-spin) relaxation time constant T_2. In most cases, 96 full echoes were

acquired. The value of 2τ was varied from 450-950 μs, depending on the desired spikelet separation in the frequency domain, ν_{CPMG}. Modified QCPMG ($\pi/2$ - τ_1 - π -τ_2 – ACQ (τ) - [τ_3 - $\pi/2$ - τ_4 – ACQ (2τ)]$_N$) experiments were conducted, where the π pulse in the echo train was replaced with a $\pi/2$ pulse.[74] Double-frequency sweep (DFS) shaped pulses were also used in conjunction QCPMG experiments to enhance the CT signal intensity.[75,76] The probes used at both fields exhibit a small, but manageable background ^{11}B signal in the acquired spectra, as a result of boron nitride in the stators. The QCPMG pulse sequence was generally found to be effective at suppressing the background signal.

Spectral Processing: Data were processed using TopSpin 2.0. FIDs were left-shifted to the echo maxima when necessary, and Fourier transformed. Stack plots were produced with DMFit.[66] QCPMG spectra can simply be compared to the simulated and experimental Hahn-echo static spectra since the QCPMG spikelet pattern mimics the lineshape of the static Hahn-echo spectrum when their lineshapes are overlaid.

Chapter 4

Limitations of Relating ^{11}B NMR Parameters to Structure

4.1 Introduction

As previously mentioned in Chapter 2, boronic acids and boronic esters[23] have a wide range of uses and applications. Having the ability to relate the acquired ^{11}B SSNMR parameters to the molecular and electronic structures of these compounds would be incredibly useful since SSNMR can provide structural information and information about the local bonding environment, i.e., by being able to relate magnetic shielding tensor data to boron molecular orbitals.

Chapter 2 provided a detailed analysis of ^{11}B NMR spectra of MAS and stationary samples of ten boron compounds. In all cases, ^{11}B CS and EFG tensor information was extracted from simulations of the static and MAS spectra. It is noted that the C_Q and Ω values were found to be larger, on average, for boronic acids than for esters. Although the ranges associated with C_Q and δ_{iso} are small relative to their absolute magnitude, the compounds in Chapter 2 have adequate structural variation that there is a significant difference in NMR parameters from compound to compound. Notably, the CS tensor span provided the largest range amongst all the compounds, and was the NMR parameter most characteristic of the molecular and electronic structure.

When considering compounds **1** – **10**, some exhibit hydrogen bonding while others do not, boronic esters are in varying ring systems with different substituents, and the aromatic ring bound to the boron has different substituents bound to it. As there is great structural variation amongst these compounds, the local environment around the boron varies a substantial amount. This is the reason for the large variation in span

between the compounds in Chapter 2. In addition, although the variations in C_Q and δ_{iso} are small as compared to span, there is still a notable difference in these values, which allows for structural comparisons to be made. In the present chapter, a new series of boron compounds are studied: six boronic acids and nine boronic acid catechol cyclic esters (see Figure 4.1). Unlike the boronic acids in Chapter 2, these catechol cyclic esters are all very structurally similar. In all cases, the boron atom is in the same catechol ring system. The only difference between the compounds is the substituent that is bound to the aromatic ring. Similarly, the boronic acids studied in this chapter are more structurally similar than those in Chapter 2. Here, the boron atom is always bound to a phenyl ring that has varying substituents. In Chapter 2, not only were the substituents varied, but the boron atom was bound to diverse aromatic systems such as naphthalene, phenyl, pyridine, and thiophene.

In Chapter 2, good correlation between experimental and GGA-revPBE calculated spans, and between the calculated boron isotropic shielding and experimental chemical shift values was observed. This chapter includes similar computational analyses comparing calculated and experimental spans, as well as calculated isotropic shielding and experimental chemical shift. The compounds in this chapter will be analyzed to determine if clear correlations between the experimental and calculated values are observed, as was the case in Chapter 2. As previously outlined, the boron CS tensor in boronic acids, and most notably the span of the CS tensor, is governed by the interplay of several competing factors. Experiments performed on compounds similar to **1** – **10** in this chapter provided a comparative study, where the effects of specific changes in structure or SSNMR parameters were probed.

The boronic acid and ester compounds studied in this thesis can serve as building blocks in supramolecular materials. This is a very exciting use of boronic acid compounds that has several vital applications including dealing with increasing energy demands.[80] Thus, the motivation into studying larger compounds such as **25** and large boron containing frameworks will be discussed.

Much groundbreaking work into the development and application of boron containing covalent organic frameworks (COFs) has been conducted by Yaghi et. al.[80] A COF is an extended organic structure where the building blocks, such as compounds containing trigonal boron bound to oxygens and aromatic rings, are linked by strong covalent bonds. These COF materials can be functionalized into materials that can serve as gas storage devices (most notably for H_2 storage) or in catalytic applications.[80] Considerable research has also gone into the development of metal organic frameworks (MOFs), which also has large potential in materials chemistry to be exploited for the same applications.[81] One obvious advantage to the use of a COF relative to a MOF is that if the framework used for hydrogen storage contains only light elements, and hence more hydrogen can be stored per mass unit. One example of such a framework is COF-1, a framework constructed via the slow dehydration of diboronic acid.[80] Similarly, a larger framework, COF-5, can be constructed by the slow dehydration of diboronic acid in the presence of hexahydroxy triphenylene.[80] COF-1 is composed of linked units of boroxine anhydride, while COF-5 is composed of linked units of triboronate ester. In this work, the starting materials and COFs were all analyzed using ^{11}B SSNMR. The lineshapes obtained are reported to be very sensitive to the immediate chemical and geometrical bonding environment. The ^{11}B SSNMR spectra that were acquired for the

COFs had lineshapes that were coincident with the spectra of the linked units that they are composed of and not coincident with the lineshapes of the starting material. This provides useful evidence that in fact the COFs are being formed and are composed of the proposed linked units.

An *ab initio* study of hydrogen adsorption onto COF-1 was carried out by Ahuja et. al. using DFT theory.[82] This computational study provides insight into where the hydrogen adsorbs onto the COF and the energies of hydrogen adsorption at different sites at various temperatures was conducted.[82]

COFs are also of interest in catalysis because they contain a large pore in the middle,[80] which can be tailored to interact with a substrate, acting as a scaffold to interact with the substrate, causing a conformational change. This conformational change can then allow the substrate to have the ability to react with a target molecule. In the case of a MOF, the metal centre is present inside the framework and the pore size may be tailored to only allow molecules of a desired size inside of the pore so that it may interact with the metal and undergo a catalytic reaction.[83]

Although COFs are not the focus of this thesis, it is very important to note that boron containing compounds, specifically boronic acids, are an extremely useful class of compounds that can be used in supramolecules, to aid in applications such as hydrogen storage or catalytic transformations. In addition, ^{11}B SSNMR is an invaluable tool which can be used to analyze and characterize these highly versatile structures.

The boron-containing compounds in this chapter were synthesized and selected as possible candidates for potential applications in supramolecular chemistry in collaboration with Dr. Kenneth Maly (Wilfrid Laurier University). They all have the

potential to be transformed into supramolecular structures via slow dehydration reactions. Different substituents on the boronic acids and esters would become integrated into the COF and, depending on the intended application, the substituents could be tailored to undergo specific interactions with a particular substrate, or another desired function. Studying these compounds using ^{11}B SSNMR is an important step in probing the local boron structure. Acquiring the ^{11}B SSNMR spectra of the starting materials and comparing the lineshapes to those of the unit linked in the COF and to the lineshape of the COF itself would prove a useful method of identifying the structures, and acquiring physicochemical data about the boron environment in the framework. In addition, when a substrate is present inside the pore of the COF, ^{11}B SSNMR could be used to probe if the boron is interacting with the substrate and what effect this interaction has on the boron environment.

This chapter covers a SSNMR study of the six boronic acids and nine boronic acid catechol cyclic esters shown in Figure 4.1. A comprehensive discussion relating their NMR parameters to molecular and electronic structure follows.

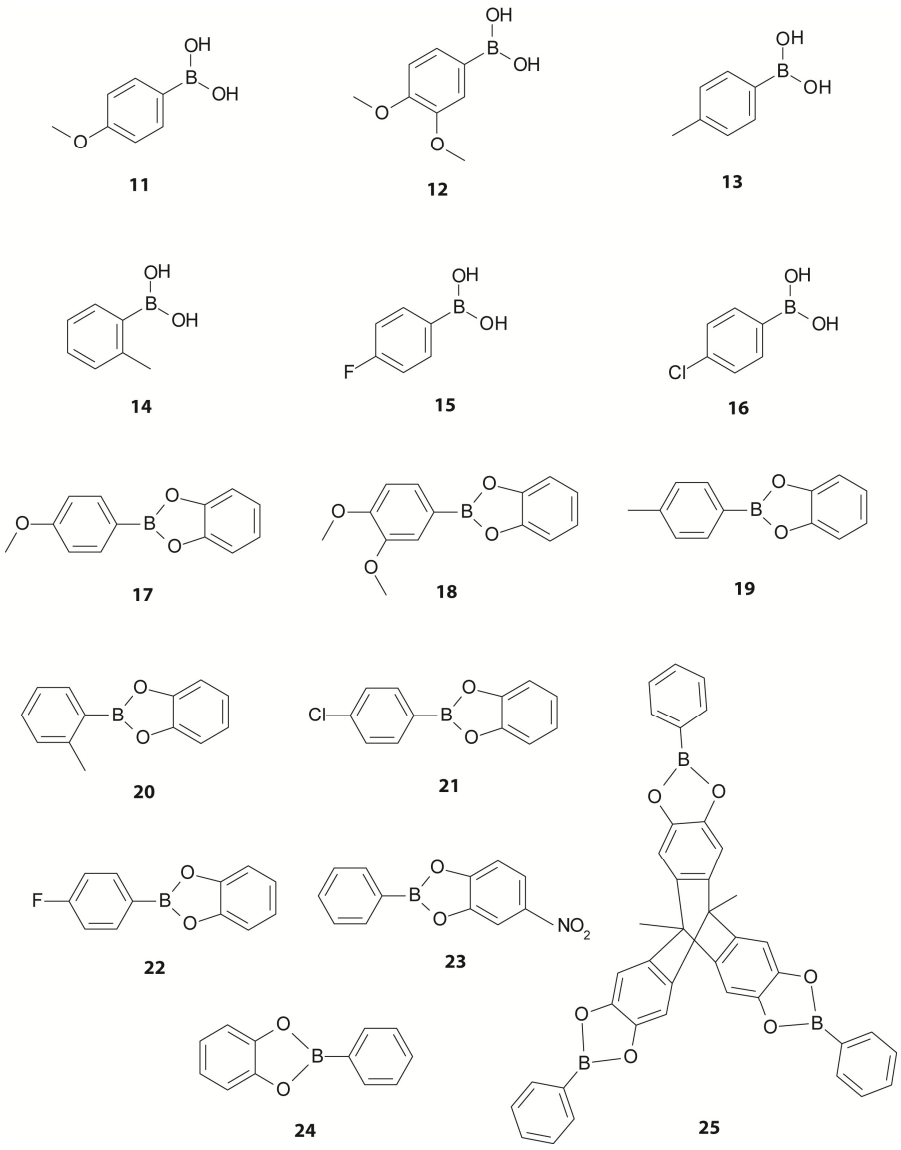

Figure 4.1: Structures of the boronic acids (**11** to **16**) and boronic acid catechol cyclic esters (**17** to **25**) studied within this chapter.

4.2 Results and Discussion

4.2.1 ^{11}B Solid-State NMR Spectroscopy

Shown in Table 4.1 are the experimental boron EFG and CS tensor values obtained via analytical simulations of the ^{11}B NMR spectra of compounds **11** to **25**. By simultaneously fitting the data at both 9.40 and 21.1 T, the C_Q, η_Q, and δ_{iso} values were determined from MAS NMR spectra. Subsequently, stationary spectra were analyzed to determine the Ω, κ, and Euler angles relating the two tensor PASs. Experimental and simulated spectra can be found in Figures 4.2 – 4.16.

In Table 4.1, the ^{11}B SSNMR parameters are also listed for boric acid, a known decomposition product of boronic acids.[23] This decomposition product is clearly identified in compounds **11** and **17** (Figures 4.2 and 4.8) and is responsible for the peak with δ_{iso} = 19.6 ppm. In addition, several spectra contain broad, low intensity peaks buried underneath the main signal. It is speculated that these peaks are likely due to small amounts of an unknown impurity or decomposition product. As a result, several of the fits in this Chapter are tentative, and many of the parameters are less precise than those determined in Chapter 2.

Table 4.1: Experimental ^{11}B EFG and CS tensor parameters for compounds **11** to **25**.[a]

	Sample	C_Q / MHz	η_Q	δ_{iso} / ppm	Ω / ppm	κ	α / º	β / º	γ / º
Boronic Acid	**11**	3.00 ± 0.10	0.70 ± 0.10	28.5 ± 0.5	20 ± 2	0.90 ± 0.10	0 ± 40	0 ± 5	0 ± 40
	12	3.00 ± 0.10	0.45 ± 0.05	29.0 ± 0.5	24 ± 6	0.60 ± 0.10	0 ± 10	0 ± 2	0 ± 10
	13	3.40 ± 0.10	0.50 ± 0.10	30.1 ± 0.2	23 ± 2	-0.45 ± 0.05	0 ± 10	7 ± 1	0 ± 10
	14	3.15 ± 0.05	0.60 ± 0.10	28.0 ± 0.5	25 ± 3	0.80 ± 0.20	0 ± 10	0 ± 5	0 ± 10
	15	3.20 ± 0.10	0.59 ± 0.01	29.2 ± 0.7	20 ± 4	0.85 ± 0.15	0 ± 10	0 ± 5	0 ± 10
	16	3.20 ± 0.10	0.40 ± 0.10	29.8 ± 0.5	25 ± 5	0.00 ± 1.00	0 ± 10	0 ± 4	0 ± 10
Catechol Cyclic Ester	**17**	2.68 ± 0.17	0.80 ± 0.10	30.8 ± 0.1	24 ± 3	-0.45 ± 0.05	0 ± 10	5 ± 3	0 ± 10
	18	2.72 ± 0.06	0.80 ± 0.01	31.4 ± 0.4	23 ± 1	-0.70 ± 0.10	0 ± 10	8 ± 2	0 ± 10
	19	2.70 ± 0.10	0.78 ± 0.02	30.3 ± 0.2	22 ± 5	-0.15 ± 0.05	7 ± 3	0 ± 2	7 ± 3
	20	2.68 ± 0.02	0.80 ± 0.10	29.7 ± 0.3	23 ± 3	-0.15 ± 0.05	8 ± 2	0 ± 2	8 ± 2
	21	2.73 ± 0.10	0.80 ± 0.10	30.2 ± 0.2	25 ± 2	-0.10 ± 0.10	0 ± 15	0 ± 2	0 ± 15
	22	2.70 ± 0.10	0.80 ± 0.10	29.6 ± 0.2	24 ± 2	-0.20 ± 0.10	0 ± 15	0 ± 2	0 ± 15
	23	2.71 ± 0.03	0.84 ± 0.04	31.0 ± 0.2	26 ± 4	-0.40 ± 0.10	0 ± 10	10 ± 2	0 ± 10
	24	2.76 ± 0.02	0.81 ± 0.01	30.7 ± 0.8	25 ± 2	-0.25 ± 0.05	0 ± 10	7 ± 2	0 ± 10
	25	2.68 ± 0.02	0.75 ± 0.05	31.9 ± 0.3	22 ± 2	-0.40 ± 0.20	0 ± 10	0 ± 2	0 ± 10
Boric Acid[b]		2.85 ± 0.05	0.40 ± 0.10	19.6 ± 0.3					

[a]Experimental C_Q, η_Q, δ_{iso}, Ω, κ, and Euler angles for each boronic acid and ester compound studied. Chemical shifts are reported with respect to solid $NaBH_4$ at -42.06 ppm. Boric acid is included as the impurity present at 19.6 ppm in the ^{11}B SSNMR spectra associated with compounds **11** and **17**.

[b]These NMR parameters were included in the simulations of the ^{11}B SSNMR spectra of compounds **11** and **17** using 8 % and 7 % intensity relative to the main signal, respectively.

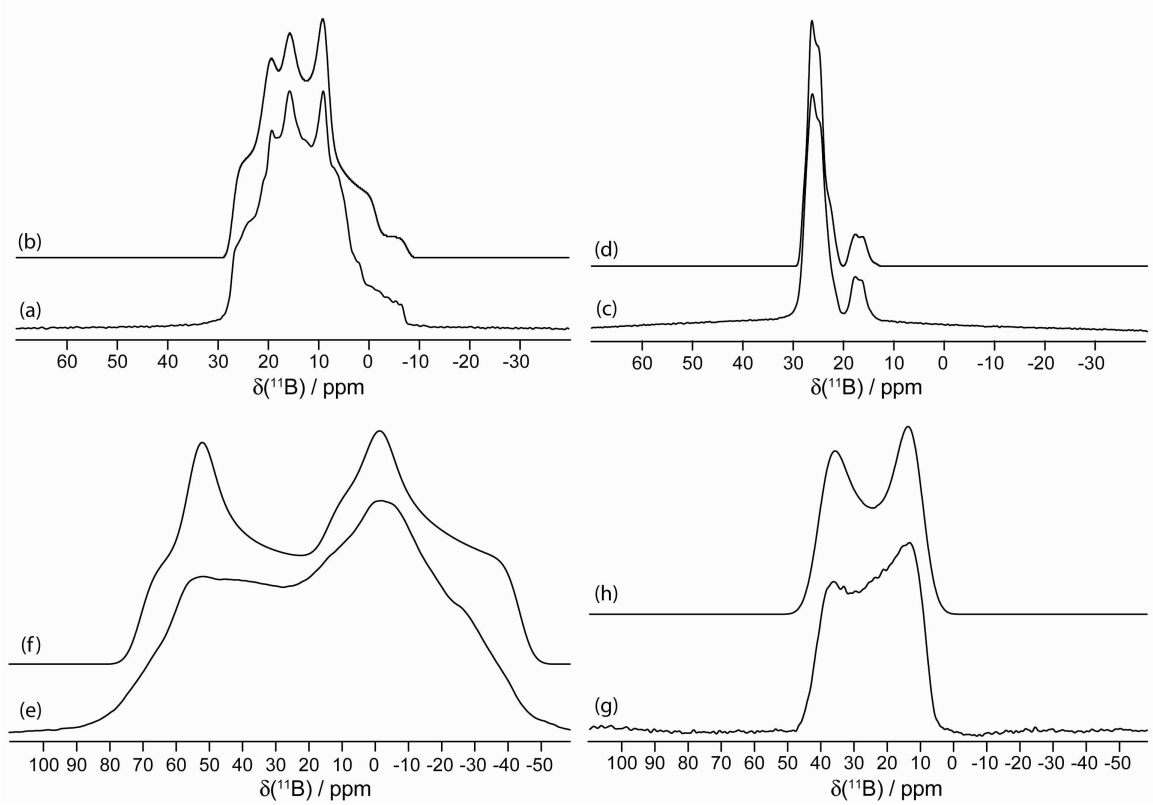

Figure 4.2: Solid-state boron-11 NMR spectroscopy of **11**. Experimental spectra of a powdered sample undergoing MAS are shown in (a) ^{11}B at 9.40 T and (c) ^{11}B at 21.1 T. Best-fit spectra were simulated using WSolids (traces (b) and (d)) using the parameters given in Table 4.1. Experimental spectra of stationary powdered samples are shown in (e) ^{11}B at 9.40 T and (g) ^{11}B at 21.1 T. Best-fit spectra were simulated using WSolids (traces (f) and (h)) using the parameters given in Table 4.1. The small lineshape in spectra (a) – (d) at ~ 19.6 ppm is due to boric acid, and its ^{11}B SSNMR spectral parameters may be found in Table 4.1.

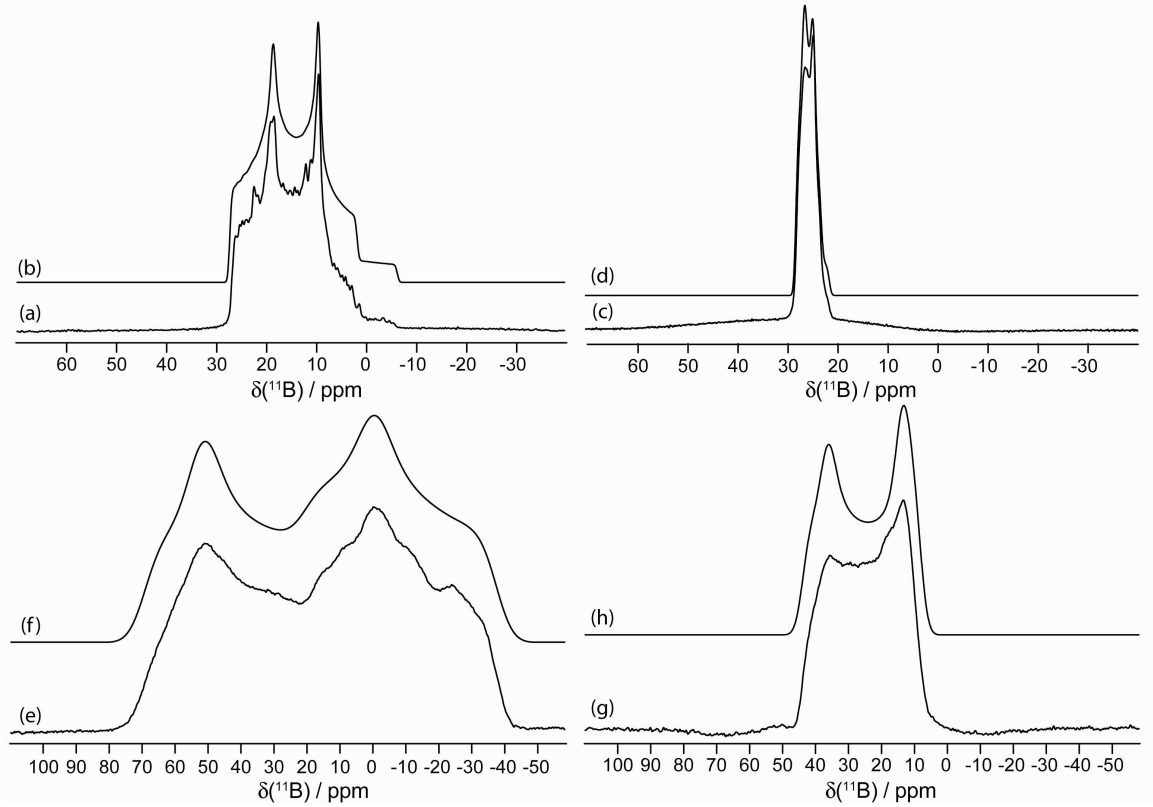

Figure 4.3: Solid-state boron-11 NMR spectroscopy of **12**. Experimental spectra of a powdered sample undergoing MAS are shown in (a) ^{11}B at 9.40 T and (c) ^{11}B at 21.1 T. Best-fit spectra were simulated using WSolids (traces (b) and (d)) using the parameters given in Table 4.1. Experimental spectra of stationary powdered samples are shown in (e) ^{11}B at 9.40 T and (g) ^{11}B at 21.1 T. Best-fit spectra were simulated using WSolids (traces (f) and (h)) using the parameters given in Table 4.1.

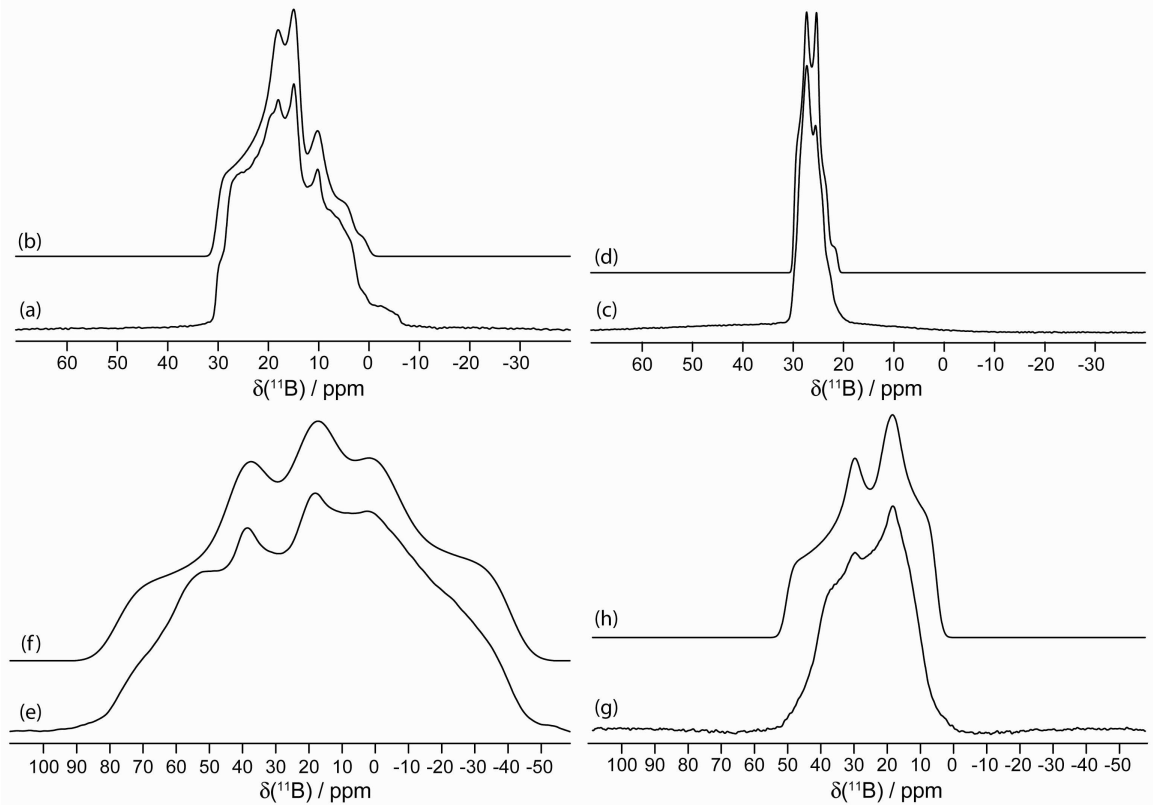

Figure 4.4: Solid-state boron-11 NMR spectroscopy of **13**. Experimental spectra of a powdered sample undergoing MAS are shown in (a) ^{11}B at 9.40 T and (c) ^{11}B at 21.1 T. Best-fit spectra were simulated using WSolids (traces (b) and (d)) using the parameters given in Table 4.1. Experimental spectra of stationary powdered samples are shown in (e) ^{11}B at 9.40 T and (g) ^{11}B at 21.1 T. Best-fit spectra were simulated using WSolids (traces (f) and (h)) using the parameters given in Table 4.1.

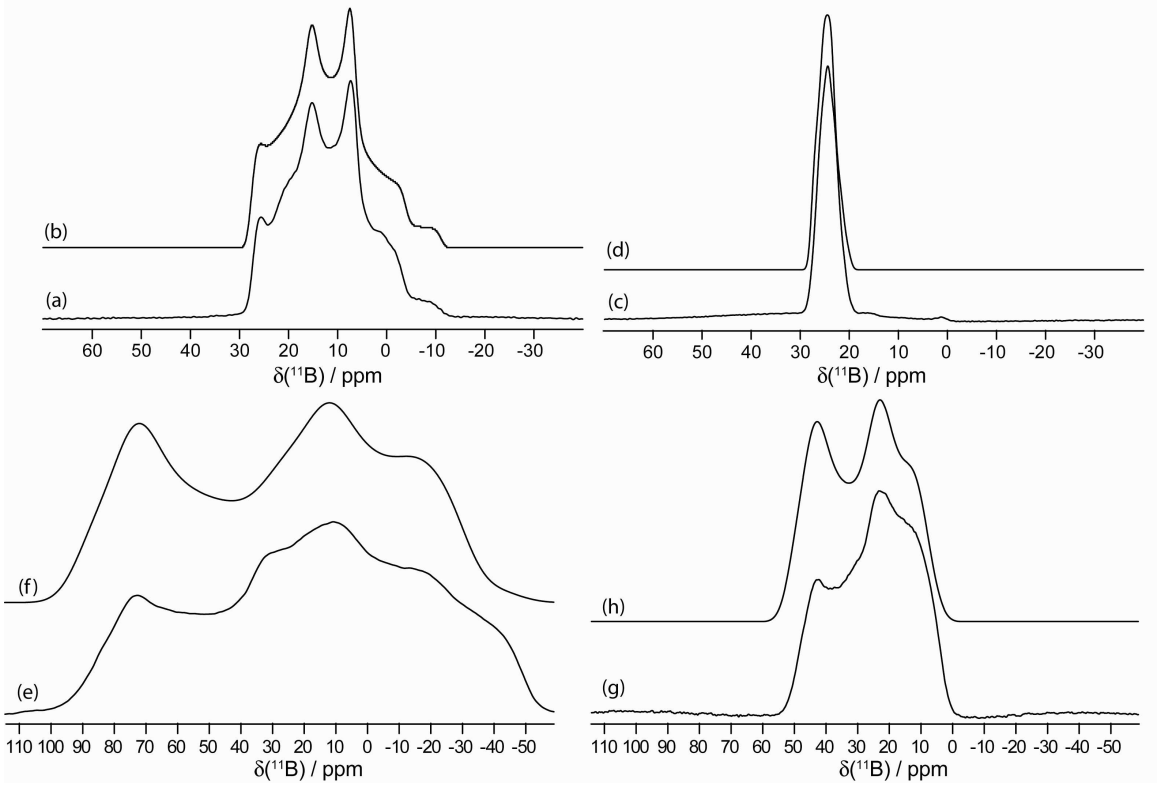

Figure 4.5: Solid-state boron-11 NMR spectroscopy of **14**. Experimental spectra of a powdered sample undergoing MAS are shown in (a) ^{11}B at 9.40 T and (c) ^{11}B at 21.1 T. Best-fit spectra were simulated using WSolids (traces (b) and (d)) using the parameters given in Table 4.1. Experimental spectra of stationary powdered samples are shown in (e) ^{11}B at 9.40 T and (g) ^{11}B at 21.1 T. Best-fit spectra were simulated using WSolids (traces (f) and (h)) using the parameters given in Table 4.1.

A small range in $C_Q(^{11}B)$ is observed ranging from 2.68 MHz for compounds **17**, **20**, and **25** to 3.40 MHz for compound **13**. An analogous statement can be made for the span, which ranged from 20 ppm in compounds **11** and **15**, to 26 ppm in compound **23**.

Similarly, there is also very little variation in the measured $\delta_{iso}(^{11}B)$ values, which range from 28.0 ppm (compound **14**) to 31.9 ppm (compound **25**), only about 3.5 % of the total known range for tricoordinate boron. For compounds **11** – **25**, the chemical shift range is even smaller than that of the compounds studied in Chapter 2. Due to this increasingly small range, it is difficult to conclusively relate $\delta_{iso}(^{11}B)$ to any single structural feature. There is only a small variation in magnetic shielding between compounds, meaning that there is little change in the electron density around the boron nucleus. In addition, there is a lack of correlation between the experimental isotropic chemical shift values and the calculated isotropic magnetic shielding values (*vide infra*).

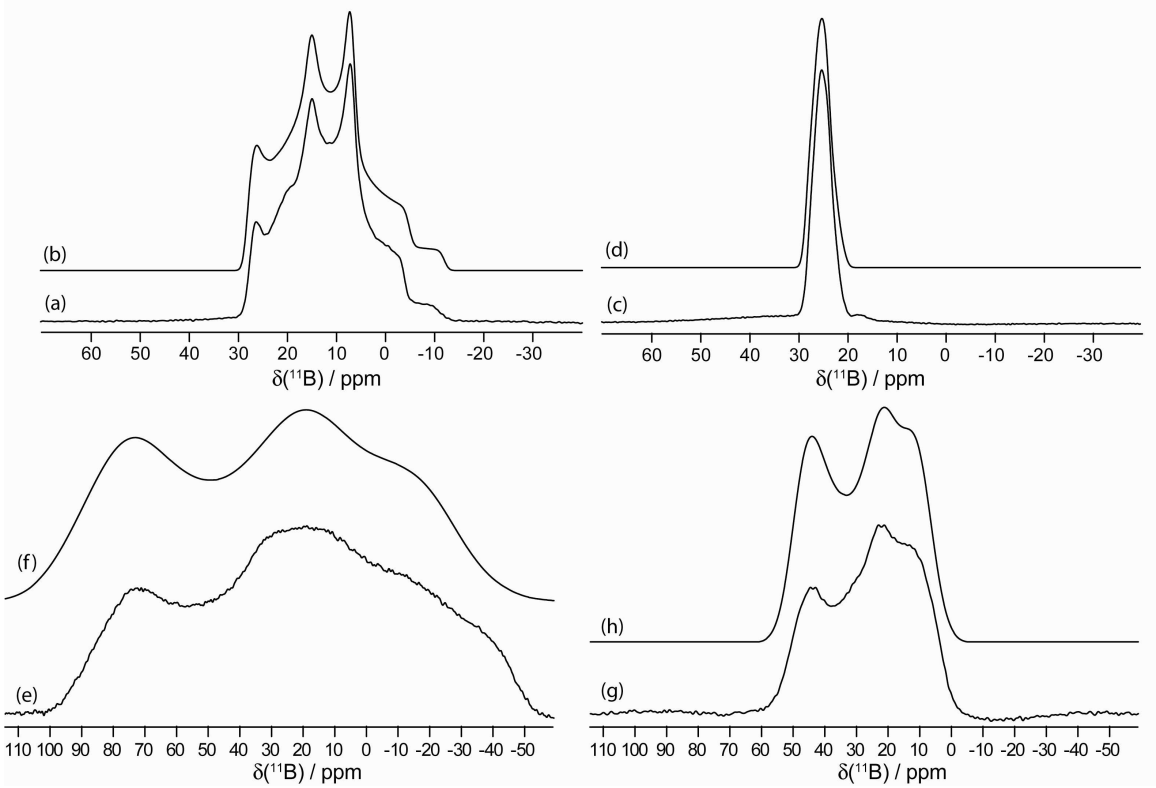

Figure 4.6: Solid-state boron-11 NMR spectroscopy of **15**. Experimental spectra of a powdered sample undergoing MAS are shown in (a) ^{11}B at 9.40 T and (c) ^{11}B at 21.1 T. Best-fit spectra were simulated using WSolids (traces (b) and (d)) using the parameters given in Table 4.1. Experimental spectra of stationary powdered samples are shown in (e) ^{11}B at 9.40 T and (g) ^{11}B at 21.1 T. Best-fit spectra were simulated using WSolids (traces (f) and (h)) using the parameters given in Table 4.1.

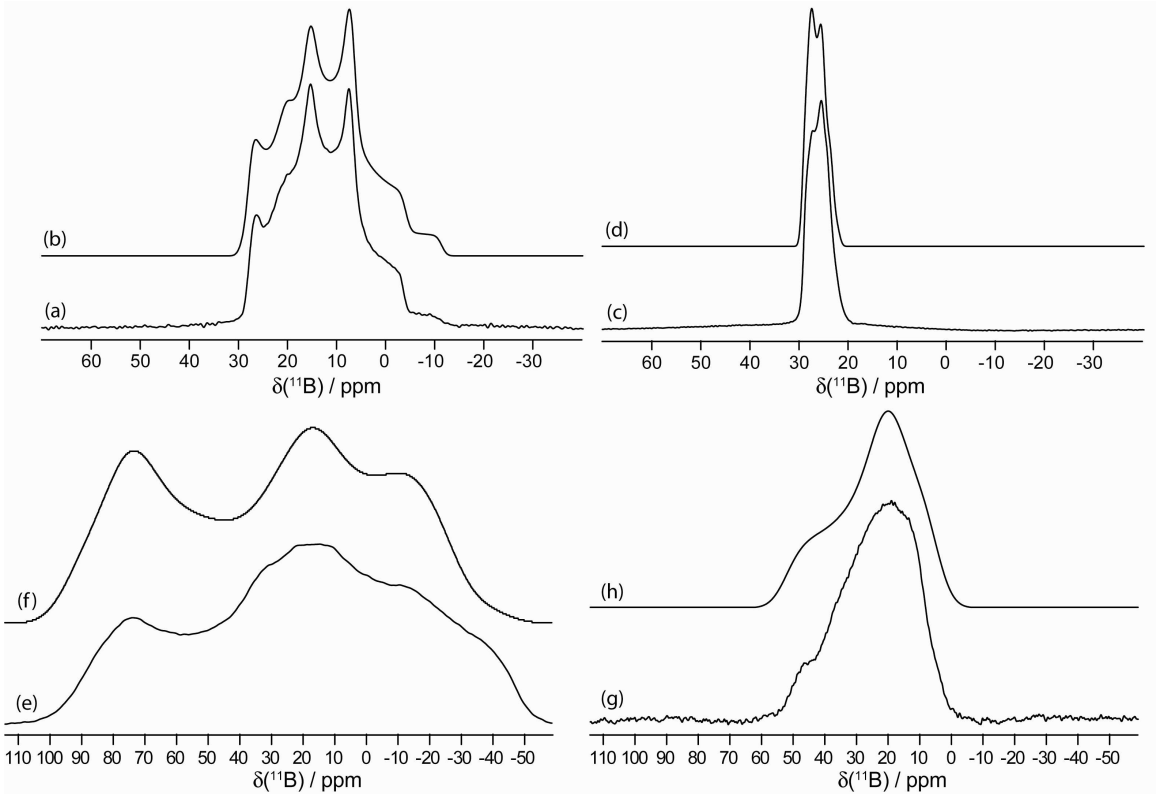

Figure 4.7: Solid-state boron-11 NMR spectroscopy of **16**. Experimental spectra of a powdered sample undergoing MAS are shown in (a) ^{11}B at 9.40 T and (c) ^{11}B at 21.1 T. Best-fit spectra were simulated using WSolids (traces (b) and (d)) using the parameters given in Table 4.1. Experimental spectra of stationary powdered samples are shown in (e) ^{11}B at 9.40 T and (g) ^{11}B at 21.1 T. Best-fit spectra were simulated using WSolids (traces (f) and (h)) using the parameters given in Table 4.1.

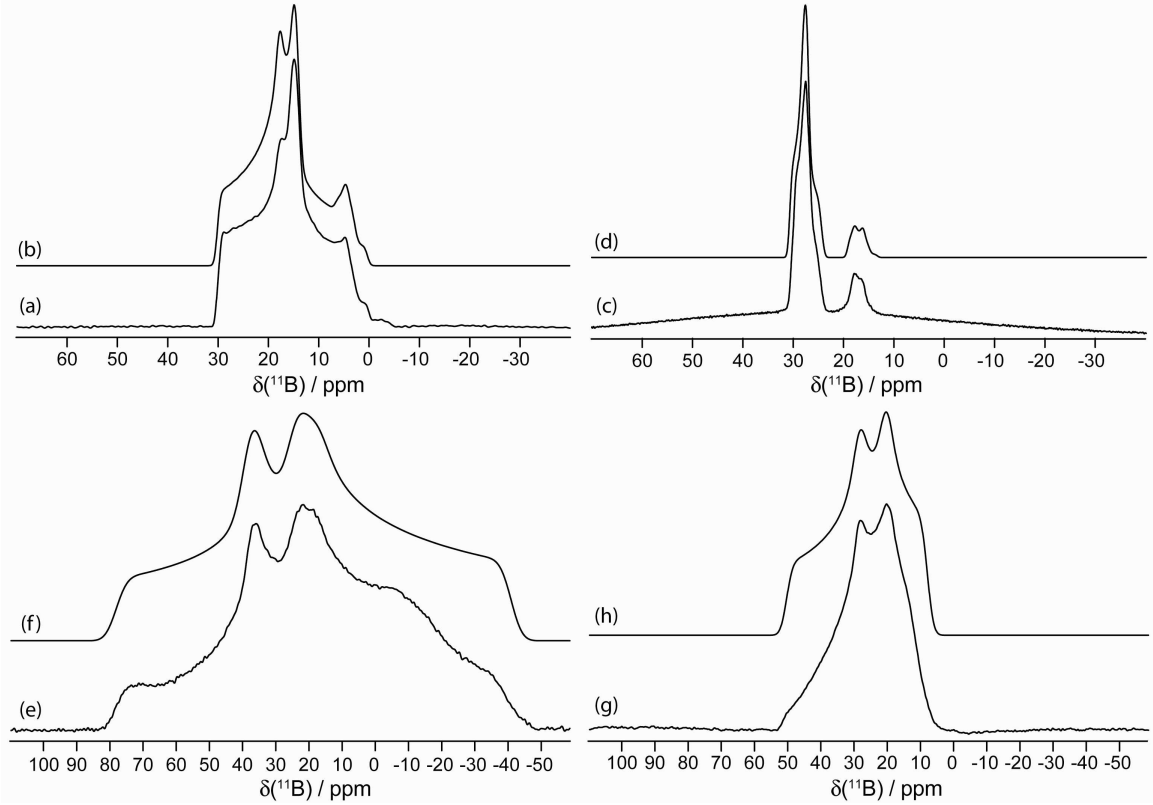

Figure 4.8: Solid-state boron-11 NMR spectroscopy of **17**. Experimental spectra of a powdered sample undergoing MAS are shown in (a) ^{11}B at 9.40 T and (c) ^{11}B at 21.1 T. Best-fit spectra were simulated using WSolids (traces (b) and (d)) using the parameters given in Table 4.1. Experimental spectra of stationary powdered samples are shown in (e) ^{11}B at 9.40 T and (g) ^{11}B at 21.1 T. Best-fit spectra were simulated using WSolids (traces (f) and (h)) using the parameters given in Table 4.1. The small lineshape in spectra (a) – (d) at ~ 19.6 ppm is due to boric acid, and its ^{11}B SSNMR spectral parameters may be found in Table 4.1.

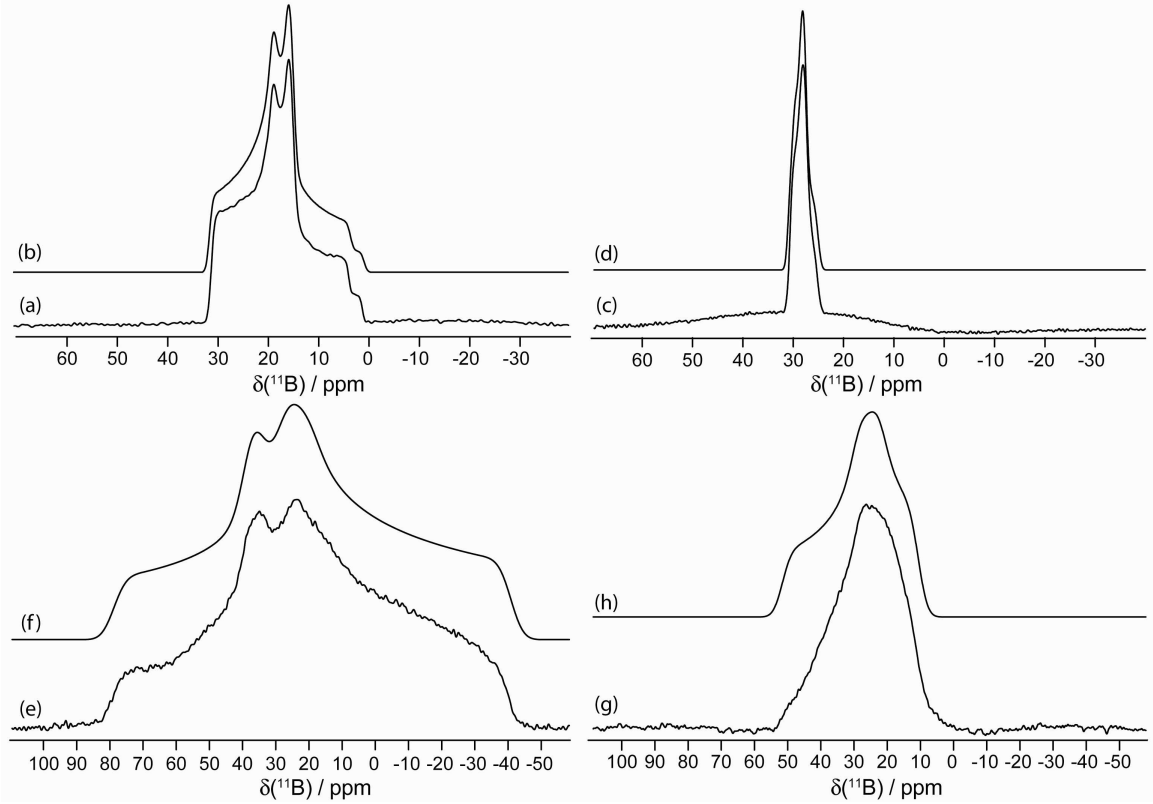

Figure 4.9: Solid-state boron-11 NMR spectroscopy of **18**. Experimental spectra of a powdered sample undergoing MAS are shown in (a) ^{11}B at 9.40 T and (c) ^{11}B at 21.1 T. Best-fit spectra were simulated using WSolids (traces (b) and (d)) using the parameters given in Table 4.1. Experimental spectra of stationary powdered samples are shown in (e) ^{11}B at 9.40 T and (g) ^{11}B at 21.1 T. Best-fit spectra were simulated using WSolids (traces (f) and (h)) using the parameters given in Table 4.1.

In general, the directions of the eigenvectors corresponding to V_{33} and δ_{33} are coincident within experimental error, as the Euler angle $\beta = 0$. When considering compounds **1** – **10**, the span was the most sensitive NMR parameter to changes in the molecular and electronic structure, with a range of 30 ppm (10 ppm for compound **9** to 40 ppm for compound **2**). However, the range in span for compounds **11** – **25** is much smaller; only 6 ppm. Although the range in Ω is much smaller here, it still has the largest relative variation among the NMR parameters for compounds **11** - **25**. For this reason it remains the primary focus and its relationship with the local boron electronic and molecular structure will be discussed later in this chapter.

As a representative sample with a good fit, shown in Figure 4.15 are ^{11}B SSNMR spectra of boronic acid catechol cyclic ester **24** obtained at 9.40 and 21.1 T. The $C_Q(^{11}B)$ value obtained for **24** is 2.76 ± 0.02 MHz and $\eta_Q = 0.81 \pm 0.01$. Boron CSA is apparent in this sample as a span value of 25 ± 2 ppm was required to obtain a good fit. The isotropic chemical shift of 30.7 ± 0.8 ppm falls within the expected range for a boronic ester.[14]

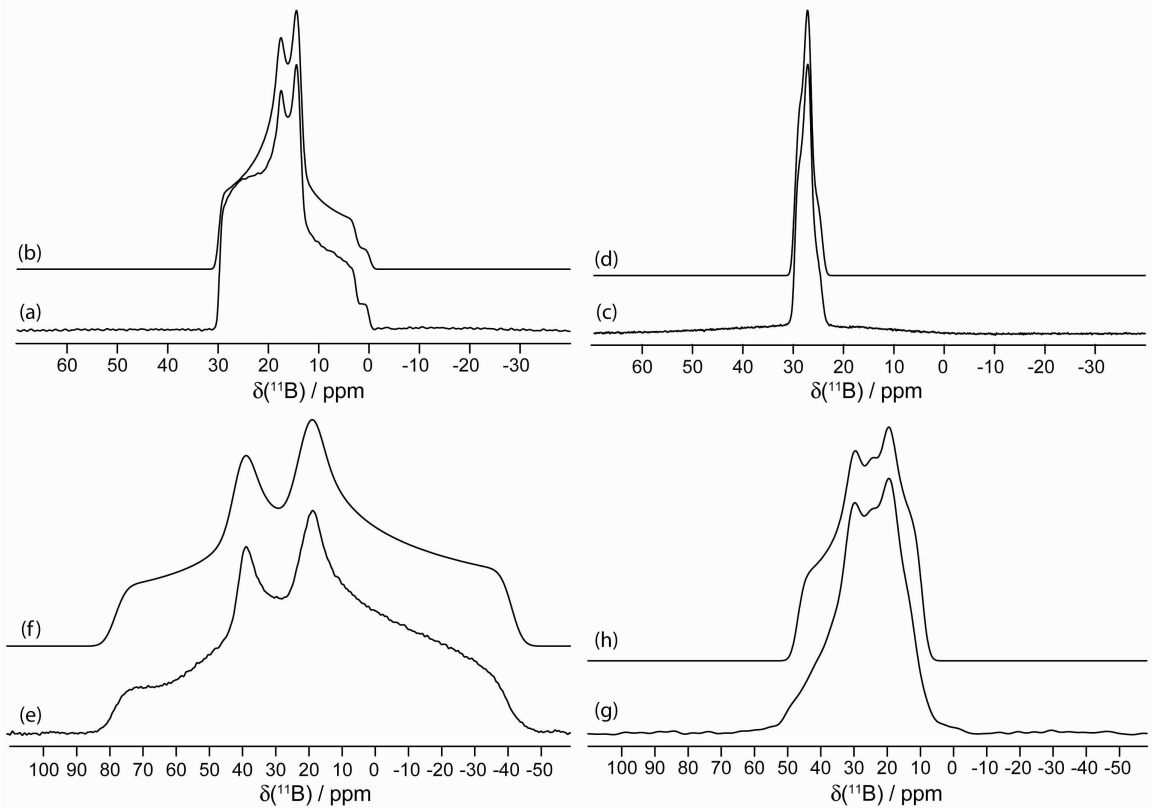

Figure 4.10: Solid-state boron-11 NMR spectroscopy of **19**. Experimental spectra of a powdered sample undergoing MAS are shown in (a) ^{11}B at 9.40 T and (c) ^{11}B at 21.1 T. Best-fit spectra were simulated using WSolids (traces (b) and (d)) using the parameters given in Table 4.1. Experimental spectra of stationary powdered samples are shown in (e) ^{11}B at 9.40 T and (g) ^{11}B at 21.1 T. Best-fit spectra were simulated using WSolids (traces (f) and (h)) using the parameters given in Table 4.1.

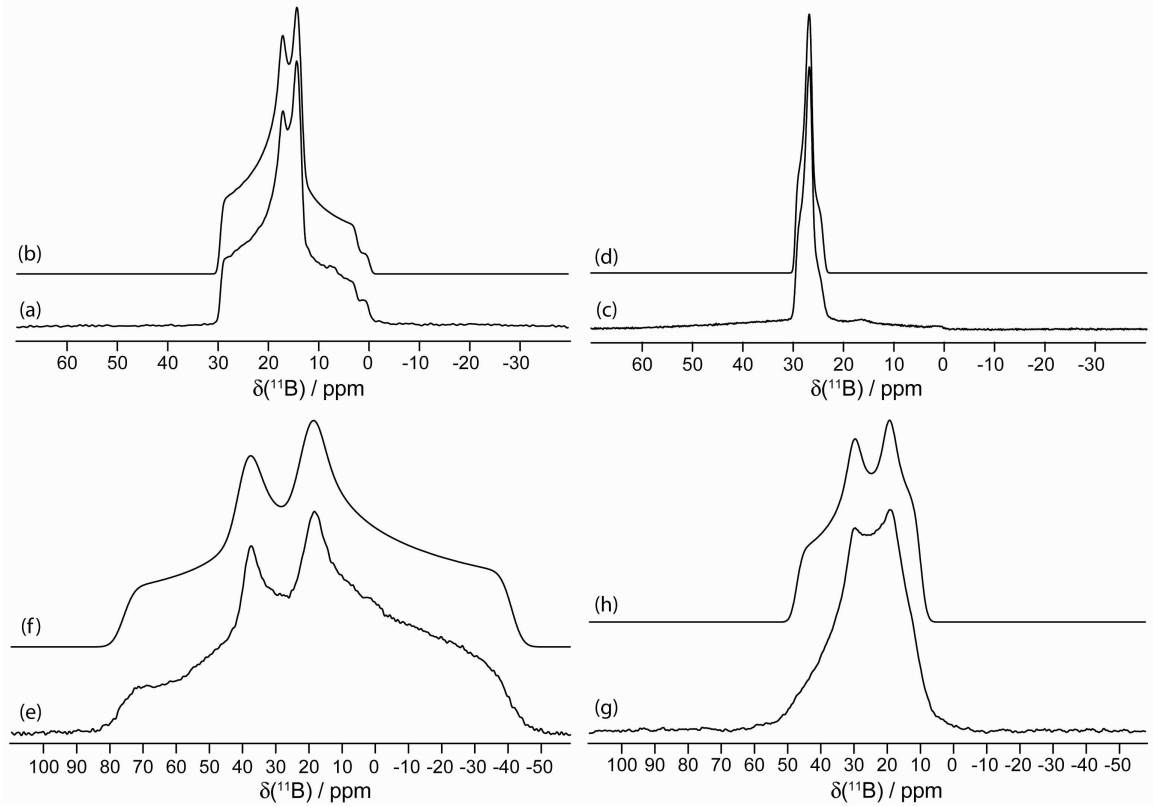

Figure 4.11: Solid-state boron-11 NMR spectroscopy of **20**. Experimental spectra of a powdered sample undergoing MAS are shown in (a) ^{11}B at 9.40 T and (c) ^{11}B at 21.1 T. Best-fit spectra were simulated using WSolids (traces (b) and (d)) using the parameters given in Table 4.1. Experimental spectra of stationary powdered samples are shown in (e) ^{11}B at 9.40 T and (g) ^{11}B at 21.1 T. Best-fit spectra were simulated using WSolids (traces (f) and (h)) using the parameters given in Table 4.1.

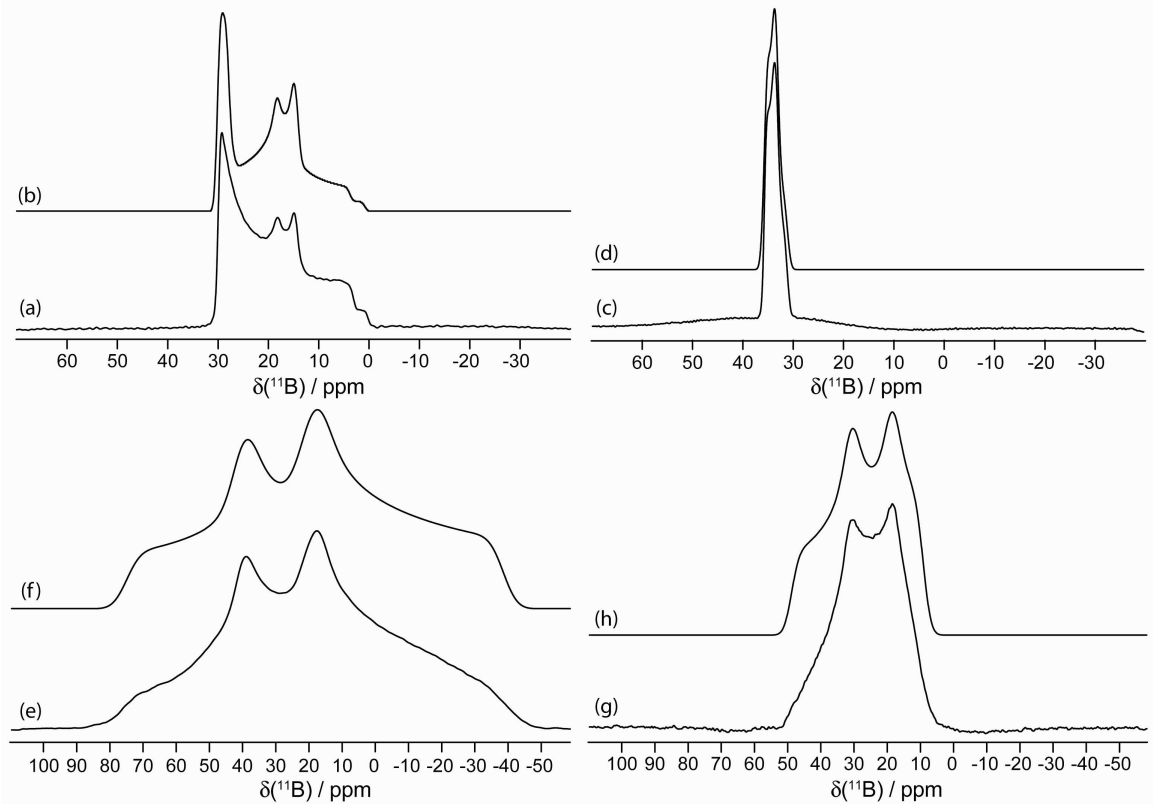

Figure 4.12: Solid-state boron-11 NMR spectroscopy of **21**. Experimental spectra of a powdered sample undergoing MAS are shown in (a) ^{11}B at 9.40 T and (c) ^{11}B at 21.1 T. Best-fit spectra were simulated using WSolids (traces (b) and (d)) using the parameters given in Table 4.1. Experimental spectra of stationary powdered samples are shown in (e) ^{11}B at 9.40 T and (g) ^{11}B at 21.1 T. Best-fit spectra were simulated using WSolids (traces (f) and (h)) using the parameters given in Table 4.1.

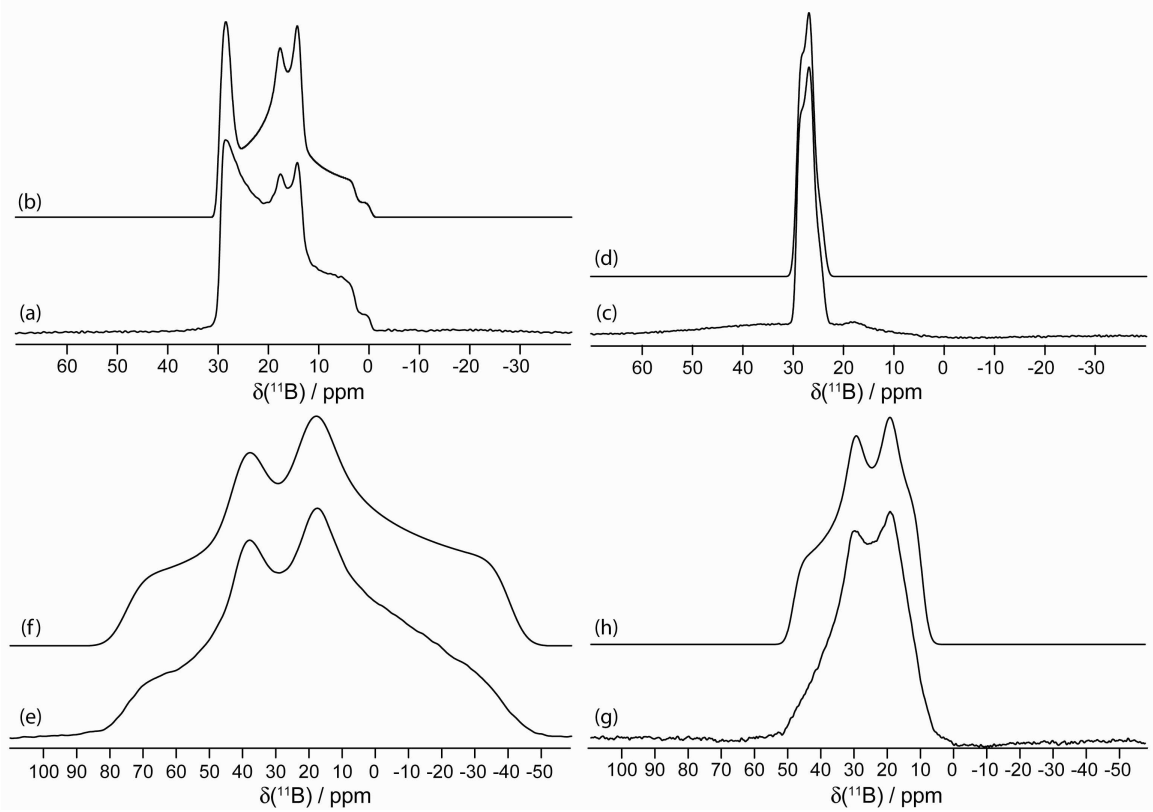

Figure 4.13: Solid-state boron-11 NMR spectroscopy of **22**. Experimental spectra of a powdered sample undergoing MAS are shown in (a) ^{11}B at 9.40 T and (c) ^{11}B at 21.1 T. Best-fit spectra were simulated using WSolids (traces (b) and (d)) using the parameters given in Table 4.1. Experimental spectra of stationary powdered samples are shown in (e) ^{11}B at 9.40 T and (g) ^{11}B at 21.1 T. Best-fit spectra were simulated using WSolids (traces (f) and (h)) using the parameters given in Table 4.1.

Depicted in Figures 4.2 to 4.14, and 4.16 are the ^{11}B SSNMR spectra of compounds **11** to **23**, and **25** respectively. Upon examination of the spectra, one should note that the ^{11}B line shapes associated with the boronic acids tend to be broader than the spectra of the boronic acid catechol cyclic esters. This observation is associated with the fact that the boronic acids tend to have larger relative $C_Q(^{11}B)$ values. In Chapter 2 there was a large variation in **Ω** which allowed for a differentiation of the boronic acids from the esters since the values for the acids were typically larger. However, the compounds studied in this chapter have only a small variation in **Ω**; hence it is not possible for differentiation between the boronic acids and boronic acid catechol cyclic esters using this NMR parameter. It should be noted that the experimental C_Q values are always larger for the boronic acids (3.00 to 3.40 MHz) than for the boronic acid catechol cyclic esters (2.68 to 2.76 MHz). This is shown below in Figure 4.17. Unlike the compounds studied in Chapter 2, there is no region of overlap between the two classes of compounds here; the C_Q values are distinctly different for the acids than for the catechol cyclic esters.

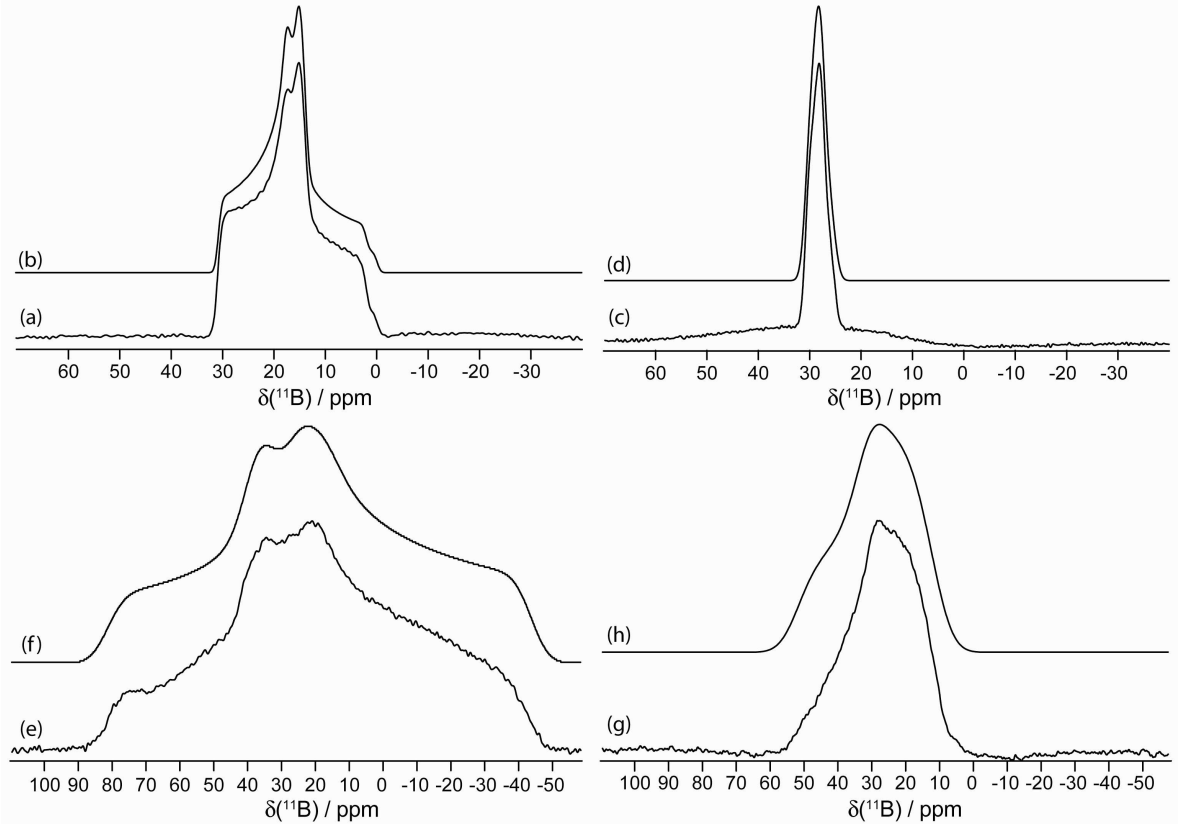

Figure 4.14: Solid-state boron-11 NMR spectroscopy of **23**. Experimental spectra of a powdered sample undergoing MAS are shown in (a) ^{11}B at 9.40 T and (c) ^{11}B at 21.1 T. Best-fit spectra were simulated using WSolids (traces (b) and (d)) using the parameters given in Table 4.1. Experimental spectra of stationary powdered samples are shown in (e) ^{11}B at 9.40 T and (g) ^{11}B at 21.1 T. Best-fit spectra were simulated using WSolids (traces (f) and (h)) using the parameters given in Table 4.1.

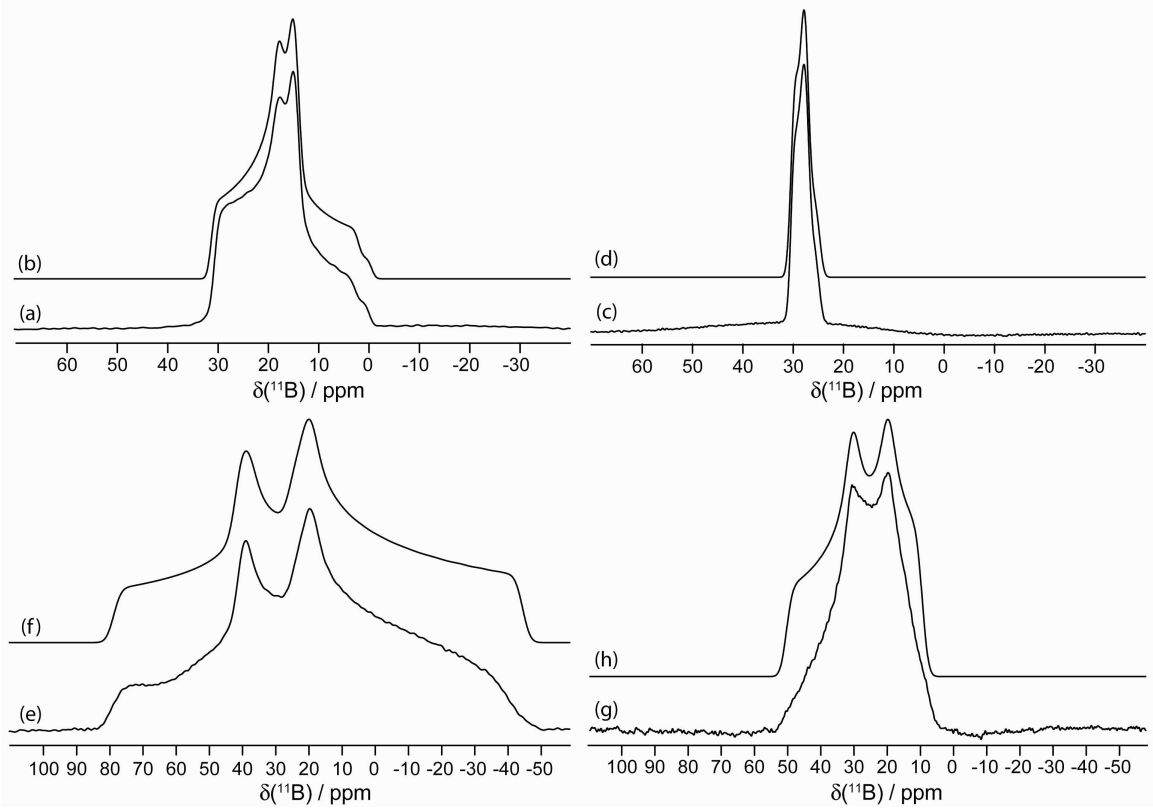

Figure 4.15: Solid-state boron-11 NMR spectroscopy of **24**. Experimental spectra of a powdered sample undergoing MAS are shown in (a) ^{11}B at 9.40 T and (c) ^{11}B at 21.1 T. Best-fit spectra were simulated using WSolids (traces (b) and (d)) using the parameters given in Table 4.1. Experimental spectra of stationary powdered samples are shown in (e) ^{11}B at 9.40 T and (g) ^{11}B at 21.1 T. Best-fit spectra were simulated using WSolids (traces (f) and (h)) using the parameters given in Table 4.1.

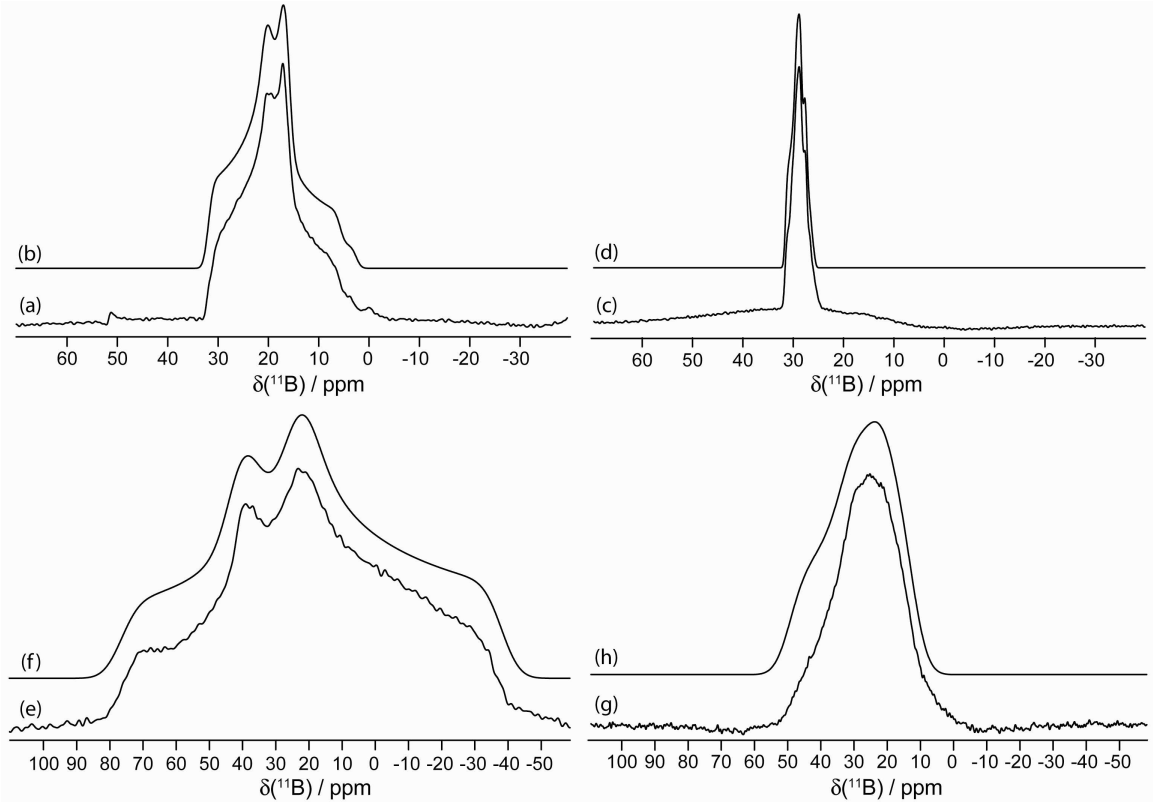

Figure 4.16: Solid-state boron-11 NMR spectroscopy of **25**. Experimental spectra of a powdered sample undergoing MAS are shown in (a) ^{11}B at 9.40 T and (c) ^{11}B at 21.1 T. Best-fit spectra were simulated using WSolids (traces (b) and (d)) using the parameters given in Table 4.1. Experimental spectra of stationary powdered samples are shown in (e) ^{11}B at 9.40 T and (g) ^{11}B at 21.1 T. Best-fit spectra were simulated using WSolids (traces (f) and (h)) using the parameters given in Table 4.1.

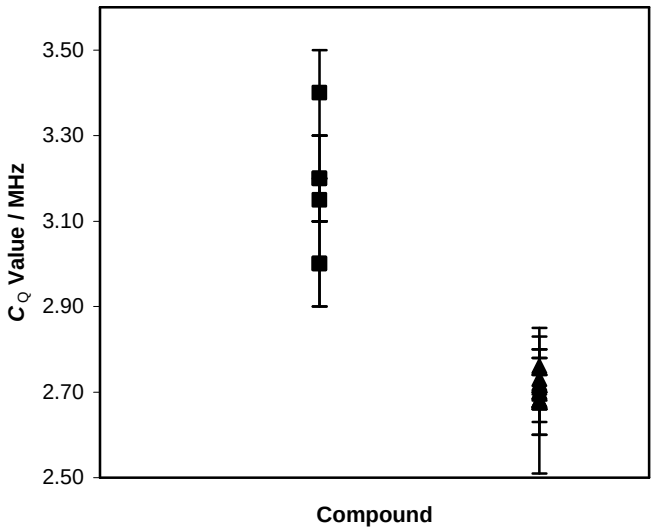

Figure 4.17: A plot of experimental C_Q values versus the type of compound being studied. The boronic acid compounds are plotted on the left, as squares, and the boronic acid catechol cyclic esters are plotted on the right, as triangles.

The fact that the C_Q values are all consistently larger for the boronic acids (3.00 – 3.40 MHz) than for the boronic acid catechol cyclic esters (2.68 – 2.76 MHz) is a useful observation that demonstrates the benefits of ^{11}B SSNMR experiments on these types of compounds. When performing NMR experiments in the liquid state, the rapid motion of the molecules leads to an averaging of the molecular orientations, thus averaging anisotropic interactions. A disadvantage to this is that a great deal of the fine structure of the lineshape is lost along with the data it contains. The averaging of molecular orientations will only lead to an isotropic chemical shift with no CSA. Likewise, the C_Q value cannot typically be measured simply by spectral simulation under these conditions. With only δ_{iso} information available, it limits the comparison of compounds to one another using only NMR data. However, in the case of the boron compounds being

studied here, there is little variation in the δ_{iso} values. The very narrow range of δ_{iso} is too small for it to be used to compare these compounds to each other, and it is not sufficient to distinguish between the boronic acids and the boronic acid catechol cyclic esters. However, in the solid-state, there are many other NMR parameters that may be used to compare compounds to one another. Fortunately, in the case of the compounds in Chapter 4, the C_Q allows us to distinguish between the two classes of compounds. Thus, the SSNMR experiments can distinguish between the boronic acids and boronic acid catechol cyclic esters. In Chapter 2, the span value was the most characteristic NMR parameter amongst the compounds but there was still a region of overlap between the span values for both sets. It is likely the most characteristic NMR parameter since the compounds were structurally dissimilar and there was such a large range in the experimental span values with little error. Here, the compounds are very similar to one another, and there exists an NMR parameter (C_Q) that clearly distinguishes between the acids and esters with no region of overlap. This is likely due to the fact that the structural similarity amongst compounds will result in a very similar C_Q value for each compound in a given structure class (boronic acids, for example). However, since boronic acids and boronic acid catechol cyclic esters are structurally different, C_Q values which are notably different from one another are observed. This is not the case for other SSNMR parameters since the relative range is much smaller and the error is much larger.

It was noted in Chapter 2 for compounds **1 – 10** that experimental boron span values varied significantly amongst different tricoordinate boron compounds. This trend was rationalized by considering the molecular orbitals for each species involved. However, since compounds **11 – 25** all have Ω values which are approximately equal to

one another, it is not useful to perform a molecular orbital analysis to distinguish amongst the compounds. This observation does not render the study of these compounds uninformative but rather provides a handle as to how much electronic variation is necessary in order for there to be an impact on the ^{11}B NMR span. When there are no variations in structure except for the substituent bound to the aromatic ring, which is distant from the boron nucleus, the variation in the simulated NMR tensor span is negligible. This is the case for the boronic acid catechol cyclic esters.

Upon examination of the ^{11}B SSNMR spectra acquired for compounds **11** – **25** (Figures 4.2 to 4.16), one may notice that several of them do not have an ideal lineshape, and it appears as though multiple boron sites may be present in the sample. Multiple quantum magic angle spinning (MQMAS) experiments were performed on several compounds as a means of determining if multiple sites were present. MQMAS can improve resolution and hence if multiple sites are present, they can be observed in the isotropic dimension. Although MQMAS experiments did not reveal multiple boron sites, based on the lineshapes observed, there is the possibility that a distribution in the C_Q values exist for each compound.

Because MQMAS was unable to conclusively determine if multiple sites were present, four of the compounds studied in this Chapter were re-crystallized so that a crystal structure could be solved, in order to elucidate the atomic structure and determine how many crystallographically unique boron sites are present. In order to obtain pure samples, the compounds were recrystallized using tetrahydrofuran (THF). Long needle-like crystals were obtained for each compound and their crystal structures were solved.

Four crystal structures were solved by I. Korobkov (University of Ottawa) using single crystal X-ray diffraction for compounds **11**, **12**, **21**, and **22**. If one simply looks at the SSNMR spectra for any of these compounds, particularly those of **21** and **22**, it is obvious that there are multiple boron sites, or an impurity present. Figure 4.18 shows an example of a spectrum that was acquired before purification and after recrystallization. Presented in Figures 4.19 – 4.22 are the asymmetric units for compounds **11**, **12**, **21**, and **22**.

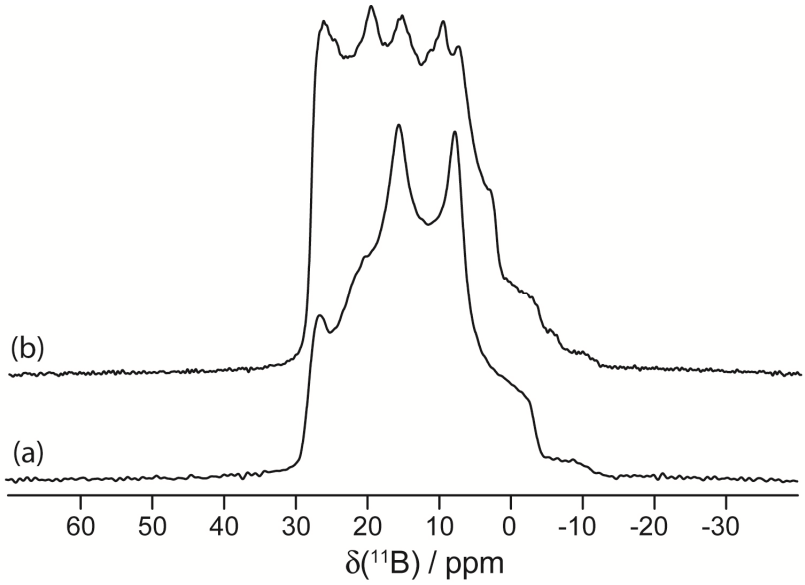

Figure 4.18: Solid-state boron-11 NMR spectroscopy of **16**. Experimental spectra of a powdered sample undergoing MAS are shown in (a) ^{11}B at 9.40 T for the compound after recrystallization and (b) ^{11}B at 9.4 T for the compound before purification.

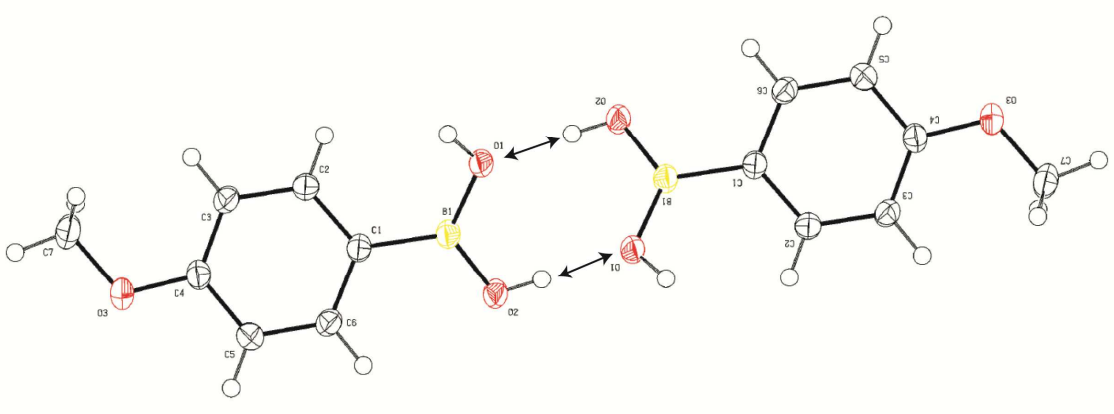

Figure 4.19: ORTEP diagram depicting the crystal structure for compound **11**. Hydrogen positions were calculated using geometry optimization calculations and plotted relative to the heavier atom positions. Arrows represent the hydrogen bonding interaction between two adjacent units.

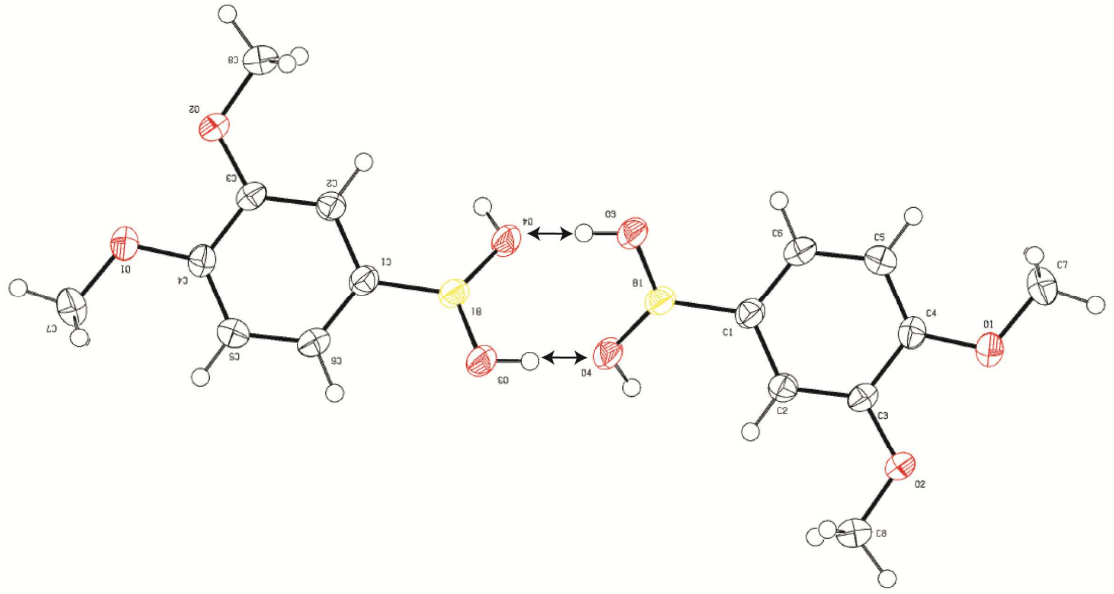

Figure 4.20: ORTEP diagram depicting the crystal structure for compound **12**. Hydrogen positions were calculated using geometry optimization calculations and plotted relative to the heavier atom positions. Arrows represent the hydrogen bonding interaction between two adjacent units.

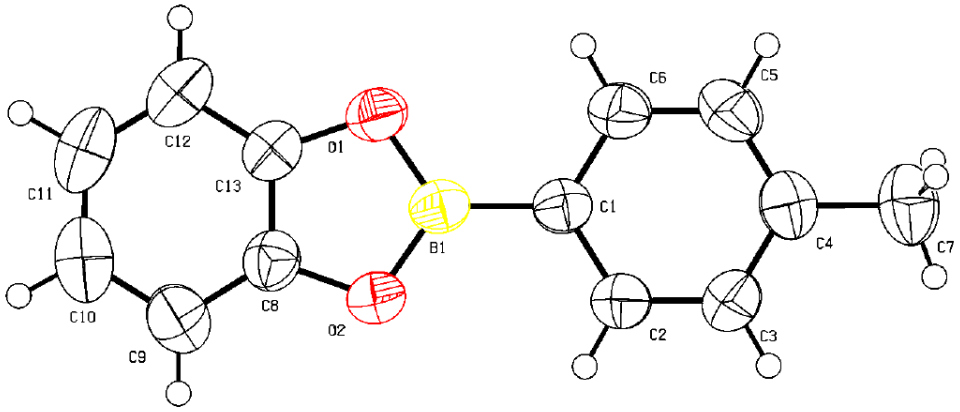

Figure 4.21: ORTEP diagram depicting the crystal structure for compound **21**. Hydrogen positions were calculated using geometry optimization calculations and plotted relative to the heavier atom positions.

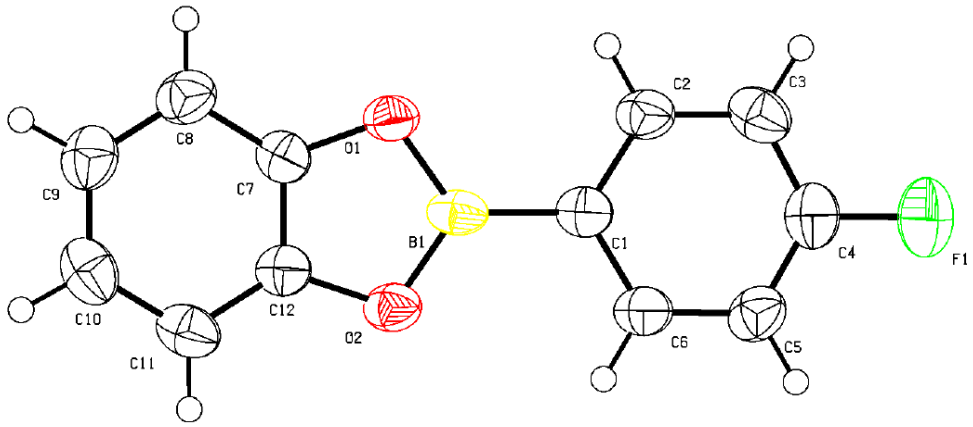

Figure 4.22: ORTEP diagram depicting the crystal structure for compound **22**. Hydrogen positions were calculated using geometry optimization calculations and plotted relative to the heavier atom positions.

These crystal structures and recrystallization verifies that ^{11}B SSNMR spectra are being acquired of the boron-containing compounds in question and not some form of

decomposition product(s). Once the pure compound has crystallized, these crystals can be used to collect the SSNMR spectrum, ensuring only the pure sample is responsible for the observed signal. After recrystallization there still appears to be multiple boron sites present. Consider Figure 4.21 for compound **21**: this compound was synthesized with the intent that it possess a Cl atom at the para position of the aromatic ring bound to the boron atom. However, the ORTEP diagram indicates that a methyl group is present in that position (see C7). There is one possible situation that could explain these observations. It is possible that, in the case of compound **21**, there are two boron compounds present: one that has a chlorine atom in the para position, and another that has a methyl group in that same position. If this is the case, when the sample was recrystallized, both compounds would have crystallized out of the solvent and formed the needle-like crystals that were collected. By chance, the single crystal chosen for analysis happened to be that of the compound with the methyl group at the para position. However, when the ^{11}B SSNMR spectrum was collected, both compounds were present, each possessing a unique boron site; hence the spectrum yielded a lineshape that indicates multiple boron sites. In spectra where it appears that there are multiple sites or there are distortions in the lineshape, it is likely that other compounds are present which give rise to another boron site, as is the case in compound **21**. Other low intensity peaks in the spectra, such as that boric acid at δ_{iso} = 19.6 ppm are due to decomposition products.

4.2.2 Computational Results

Shown in Table 4.2 are the boron EFG and CS tensors calculated using the DFT B3LYP method for compounds **11** to **25**. Table 4.3 contains the analogous information for calculations using the GGA-revPBE method for compounds **11** to **25**.

Table 4.2: Calculated EFG and CS tensor parameters for compounds **11** to **25**.[a]

		B3LYP							
	Sample	C_Q / MHz	η_Q	σ_{calc}	Ω / ppm	κ	α / º	β / º	γ / º
Boronic Acid	**11**	3.085	0.671	75.0650	21.935	0.786	65	0	294
	11†	3.062	0.590	74.8248	27.561	-0.232	39	2	295
	12	3.101	0.645	75.5440	21.315	0.918	284	1	152
	12†	3.066	0.581	74.6033	28.016	-0.241	316	7	70
	13	3.113	0.659	74.9182	21.503	0.927	269	0	92
	13†	3.085	0.579	74.6553	27.608	-0.251	43	4	109
	14	3.081	0.662	74.5749	21.021	0.929	165	0	277
	14†	3.076	0.560	73.2256	27.870	-0.153	313	18	74
	15	3.101	0.635	75.5495	21.580	0.824	276	0	174
	15†	3.073	0.564	74.9972	26.971	-0.251	137	5	253
	16	3.105	0.628	75.3490	21.905	0.805	59	0	31
	16†	3.075	0.558	74.9981	27.258	-0.243	138	4	252
Catechol Cyclic Ester	**17**	2.710	0.915	70.7293	25.936	-0.921	270	90	90
	18	2.725	0.888	71.0327	24.415	-0.959	88	21	272
	19	2.738	0.897	70.5789	24.518	-0.995	270	50	90
	20	2.705	0.914	70.5250	23.906	-0.947	90	0	270
	21	2.725	0.862	71.0350	23.494	-0.856	308	0	52
	22	2.723	0.871	71.0167	23.083	-0.897	90	0	270
	23	2.782	0.945	69.2654	27.915	-0.762	272	90	90
	24	3.017	0.754	69.0977	44.340	-0.308	323	0	37
	25	2.720	0.889	70.4424	23.661	-0.936	90	31	270
Boric Acid		2.465	0.304	78.4019	13.326	-0.694	241	0	112

† Corresponds to boronic acid dimer

[a] Calculated values for boronic acid dimers which take hydrogen bonding interactions into account are included where applicable. Hybrid DFT calculations were performed using the B3LYP functional and the 6-311+G* basis set on all elements. Boric acid is included as the impurity present at 19.6 ppm in compounds **11** and **17**.

Table 4.3: Calculated EFG and CS tensor parameters for compounds **11** to **25**.[a]

		GGA revPBE				
	Sample	C_Q / MHz	η_Q	σ_{calc}	Ω / ppm	ϕ_{CCBO} / °
Boronic Acid	**11**	2.80	0.693	72.243	21.260	0
	11†	2.78	0.599	71.471	24.205	2
	12	2.82	0.668	72.553	22.559	0
	12†	2.79	0.590	71.513	25.017	6
	13	2.84	0.677	72.118	22.522	0
	13†	2.82	0.585	71.365	24.911	3
	14	2.84	0.678	71.103	22.203	6
	14†	2.81	0.564	70.296	25.513	14
	15	2.82	0.656	72.584	23.089	0
	15†	2.81	0.572	71.729	24.421	4
	16	2.83	0.648	72.426	23.713	0
	16†	2.81	0.566	71.646	24.754	3
Catechol Cyclic Ester	**17**	2.41	0.933	67.497	21.492	0
	18	2.43	0.905	67.822	21.188	0
	19	2.45	0.910	67.391	21.322	0
	20	2.41	0.930	67.281	20.697	0
	21	2.43	0.875	67.798	20.475	0
	22	2.43	0.884	67.837	19.958	0
	23	2.50	0.955	66.000	23.094	0
	24	2.74	0.742	65.327	22.636	90
	25	2.42	0.905	67.017	20.173	1
Boric Acid		2.24	0.300	78.598	11.4	0

† Corresponds to calculations which used a boronic acid dimer.

[a] Calculated values for boronic acid dimers which take hydrogen bonding interactions into account are included where applicable. These ADF calculations were performed using the GGA-revPBE functional and the TZP basis set on all elements. ϕ_{CCBO} is defined in Figure 2.25. Boric acid is included as it was the impurity present at 19.6 ppm in compounds **11** and **17**.

The above ADF calculations were performed using the GGA rev-PBE functional and the TZP basis set on all elements shown in Table 4.3. These calculations yielded results that were comparable to experimental results however, calculations employing a larger basis set (TZ2P) and using the VWN LDA method were also carried out in an attempt to achieve calculated NMR parameters that were in better agreement with the experimental data. Logically, computations which use a higher level basis set should provide more accurate results. These results are shown in Table 4.4. In addition, the inclusion of the VWN LDA should yield results that more closely reflect the experimental data. This is indeed the case for the results discussed here. Although calculations using the TZP basis set and the X-alpha LDA provided results that were not in agreement to the same degree as when the TZ2P basis set and VWN LDA were used, those data are still useful and can be used to obtain approximate values for the NMR parameters being calculated. The improved accuracy comes at the cost of having to expend more computational resources. These results are consistent with recent work by Autschbach et. al., who showed that GGA revPBE calculations using the TZ2P basis set and the VWN LDA did a much better job at calculating the CS and EFG tensor information than the TZP basis set with the X-alpha LDA for various ^{27}Al systems.[84] All discussion of calculated NMR parameters beyond this point refer to the GGA rev-PBE calculations where the TZ2P basis set and VWN LDA were used unless specified otherwise.

Table 4.4: Calculated EFG and CS tensor parameters for compounds **11** to **25**.[a]

		GGA revPBE				
	Sample	C_Q / MHz	η_Q	σ_{calc}	Ω / ppm	ϕ_{CCBO} / °
Boronic Acid	**11**	2.95	0.621	72.321	21.848	0
	11†	2.94	0.548	71.531	24.342	2
	12	2.97	0.597	72.635	23.083	0
	12†	2.94	0.540	71.569	25.135	6
	13	2.98	0.606	72.197	23.091	0
	13†	2.97	0.536	71.427	25.097	3
	14	2.97	0.588	71.245	23.778	6
	14†	2.96	0.515	70.338	25.636	14
	15	2.97	0.585	72.670	23.617	0
	15†	2.96	0.523	71.801	24.632	4
	16	2.97	0.576	72.527	24.252	0
	16†	2.96	0.516	71.733	24.973	3
Catechol Cyclic Ester	**17**	2.57	0.867	67.640	21.974	0
	18	2.59	0.841	67.958	21.614	0
	19	2.61	0.846	67.526	21.792	0
	20	2.57	0.863	67.450	21.171	0
	21	2.59	0.811	67.954	20.956	0
	22	2.59	0.821	67.982	20.440	0
	23	2.66	0.891	66.129	22.265	0
	24	2.89	0.694	65.541	43.239	90
	25	2.58	0.840	67.090	20.648	1
Boric Acid		2.27	0.288	78.605	12.3	0

† Corresponds to calculations which used a boronic acid dimer

[a] Calculated values for boronic acid dimers which take hydrogen bonding interactions into account are included where applicable. These ADF calculations were performed using the VWN LDA, GGA-revPBE functional, and the TZ2P basis set on all elements. ϕ_{CCBO} is defined in Figure 2.25. Boric acid is included as it was the impurity present at 19.6 ppm in compounds **11** and **17**.

The GGA-revPBE calculated σ_{iso} values are plotted against the experimental values of δ_{iso} in Figure 4.23. Although there is only a weak correlation between the experimental and calculated data, one should note that there are two separate clusters of data points on the plot. The data points towards the top of the graph are those for the boronic acids and they all have larger calculated σ_{iso} values. The data points towards the bottom right are those for the boronic acid catechol cyclic esters and they all have smaller calculated σ_{iso} values. It is important to point out that although there is a distinct difference between the calculated σ_{iso} values for each set of compounds, there is a large region of overlap between the δ_{iso} values, which implies that the experimental δ_{iso} values do not differentiate the two sets of compounds. Differently, in Chapter 2, an analogous plot (Figure 2.24) shows a good correlation between σ_{iso} and δ_{iso}. This can be explained by the fact that compounds **1** – **10** are all structurally very different from one another hence, the electronic environment has sufficient variation to cause the σ_{iso} (and δ_{iso}) values to be more distinct between compounds. This also led to a larger range of experimental δ_{iso} values for compounds **1** – **10**. However, the range and relative error of the experimental δ_{iso} values is much smaller than it was for compounds **1** – **10**. It is this small range and large error which may lead to the poor correlation between calculated and experimental values. The general trend however, is correct in that the slope is negative, implying that σ_{iso} and δ_{iso} values are inversely related to one another. When considering the boronic acids and boronic esters in Chapter 2, there was no distinction in σ_{iso} (and δ_{iso}) values between the two sets of compounds due to the vast structural differences. When considering compounds **11** – **25**, the boronic acids are all very similar to one another, as are the boronic acid catechol cyclic esters. This is likely what led to

the two distinct regions of data points observed in the plot below. This implies that there are distinct shielding contributions in these systems that push the σ_{iso} values for the acids to larger values.

Shown in Figure 2.27 are the diamagnetic contributions that play an important role in the magnetic shielding tensor for these compounds. Figure 2.27 shows that σ_{33} (and possibly σ_{22}) are shifting to a more positive value, which causes an increase in σ_{iso} and hence, the calculated σ_{iso} values for the boronic acids tend to be larger than those of the boronic acid cyclic catechol esters.

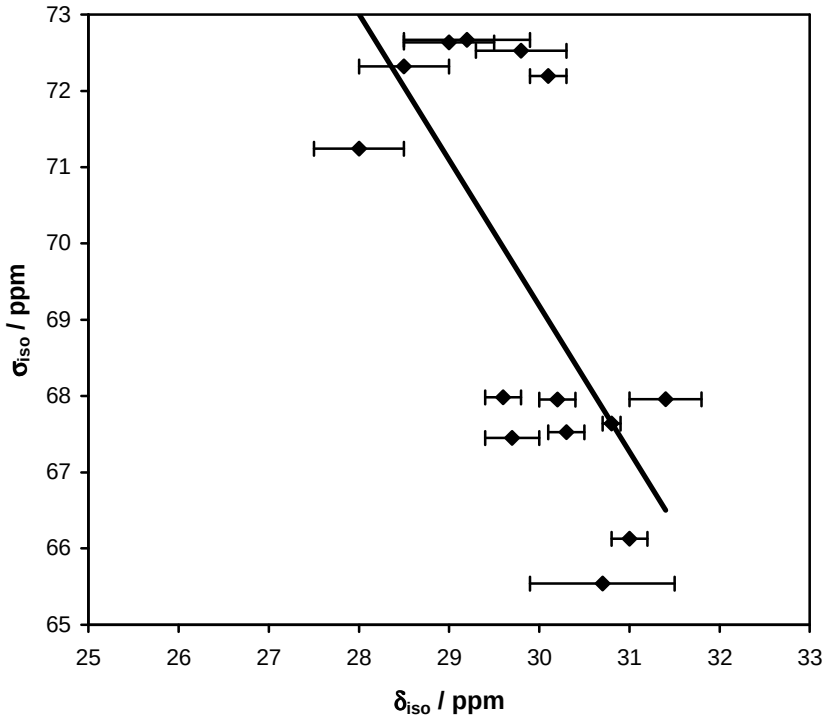

Figure 4.23: Correlation between the calculated (ADF/GGA revPBE) total isotropic shielding and experimental and isotropic chemical shift values measured in the solid state for each boronic acid and boronic acid catechol cyclic ester studied in Chapter 4. Experimental isotropic chemical shift is plotted against the calculated total isotropic

shielding values for the dimer where applicable. These data have a R^2 value of 0.4808 with a trend line given by y = -1.913x + 126.57.

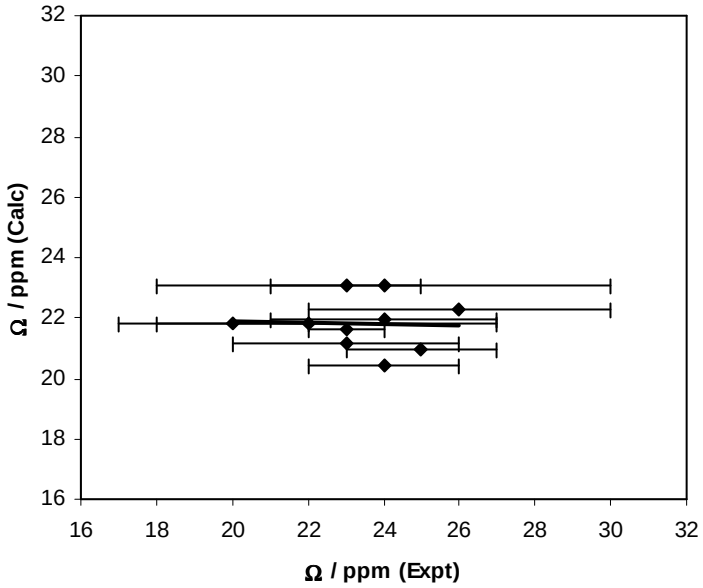

Figure 4.24: Correlation between the calculated (ADF/GGA revPBE) and experimental span values measured in the solid state for each boronic acid and boronic acid catechol cyclic ester studied. Experimental span is plotted against the calculated span values for the dimer where applicable.

Figure 4.24 shows a very poor correlation between the experimental and calculated Ω values. This poor agreement is likely due to the small range of spans observed for the compounds studied in this chapter, which is just 6 ppm. In addition, the error associated with the experimental span values ranges from 1 to 6 ppm. Thus, in some cases, the error is exactly equal to the entire range of the span values. With such a small Ω range and such large measurement error, it is not practical to try and relate Ω

values with the molecular or electronic environment. What can be said however, is that for compounds such as the boronic acid catechol cyclic esters, simply altering the substituent on the aromatic ring system, which is relatively distant from the boron nucleus, is not enough electronic variation to have a significant impact on the observed CS NMR parameters.

The GGA revPBE-calculated values for compounds **11** – **25** cannot be used to discuss the impact of hydrogen bonding or electronic substituents on the span as was done in Chapter 2. There is simply not enough electronic variation amongst the compounds.

Once again, the impact of ϕ_{CCBO} (see Figure 2.25 for angle definition) upon calculated Ω values was studied. Shown in Figure 4.24 are the calculated Ω values versus the calculated GGA-revPBE optimized dihedral angles for the optimized structure of each boronic acid and boronic acid catechol cyclic ester.

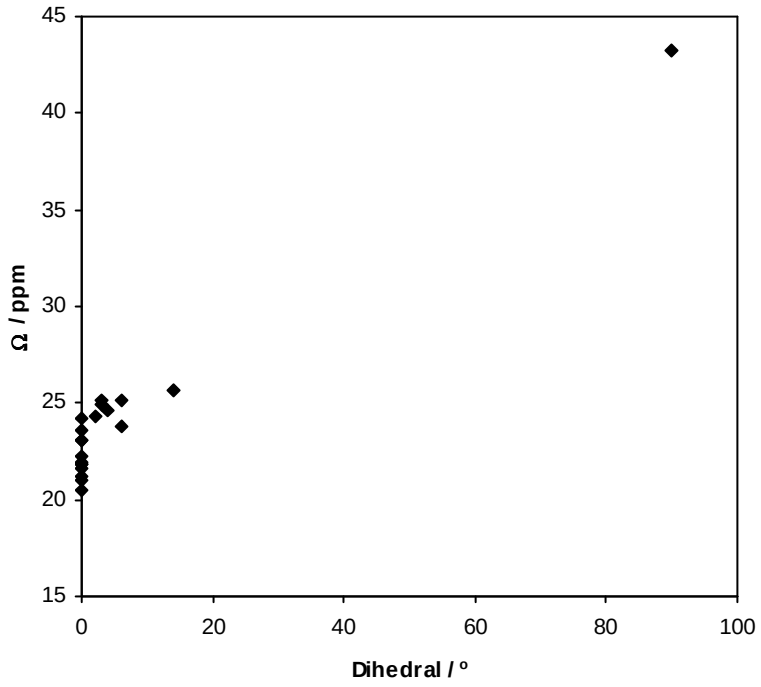

Figure 4.25: Correlation between the calculated Ω values and ϕ_{CCBO} for compounds **11** - **25**.

As noted earlier, ϕ_{CCBO} is altered primarily by sterics, and hence depends on the bulkiness of nearby substituents on the aromatic ring. As discussed in Chapter 2, the ϕ_{CCBO} values discussed here are referring to those calculated using the GGA-revPBE functional. Figure 4.25 reveals no clear and direct correlation between ϕ_{CCBO} and Ω, which is not surprising since the dihedral angle for the vast majority of the compounds is either equal to zero or has a value close to zero. Nevertheless, the general trend of increasing Ω with increasing ϕ_{CCBO} can be observed. The reason that the ϕ_{CCBO} values are so small amongst these compounds is due to there being bulky groups adjacent to the ring system which would cause the angle to increase. The general relationship between Ω and

ϕ_{CCBO} discussed earlier tells us that at small ϕ_{CCBO} values, one can expect to see smaller Ω values. In the case of compounds **11 - 25**, most have ϕ_{CCBO} values that are close to one another, similar to their spans. Therefore the data in Figure 4.25 are consistent with the span values observed; most of the compounds listed here have small and similar ϕ_{CCBO} values as well as small and similar Ω values. In the case of the large angle for compound **24**, the Ω value is large as expected.

4.2.3 Effect of Varying the Ring System Bound to the Boron Atom

One main difference between the two sets of compounds **1 – 10** and **11 – 25** is that each of the compounds **1 – 10** have the boron atom contained in completely different environments. To investigate what effects the ring system bound to the boron atom have on the NMR parameters, a computational study was performed on a series of compounds where the ring system was systematically varied. The compounds studied are shown in Figure 4.26.

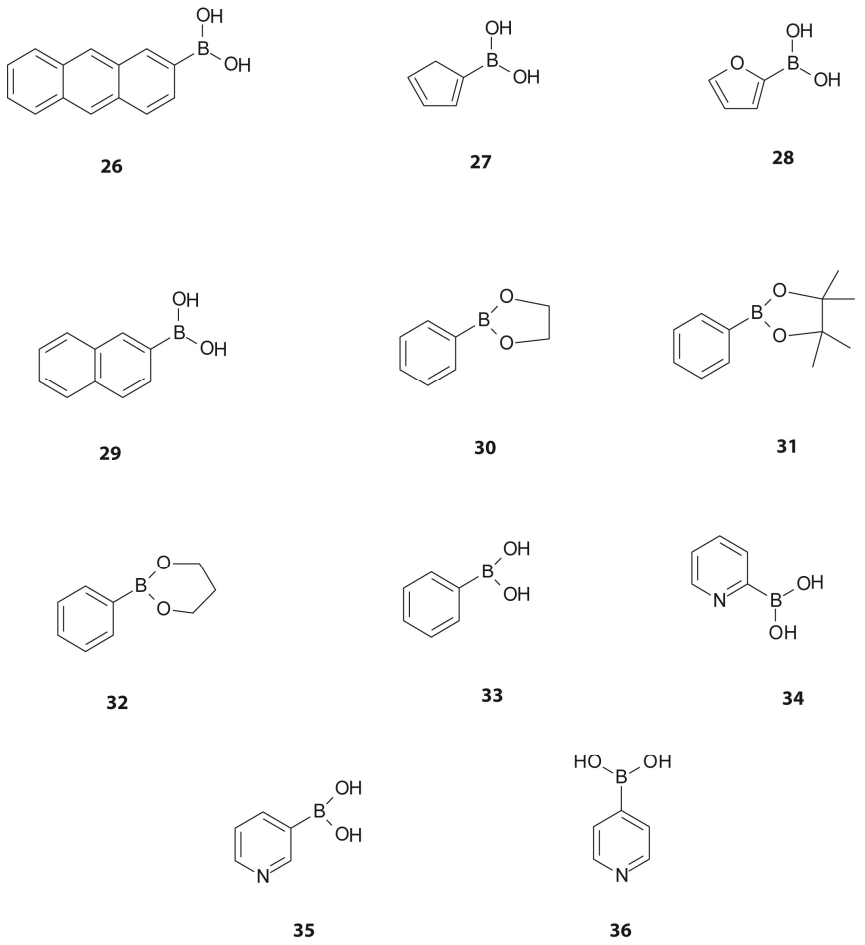

Figure 4.26: Structures of the boron compounds with varying ring systems (**26 – 36**) used in section 4.2.3.

Each compound was constructed in Gaussview and a hybrid DFT geometry optimization calculation using the B3LYP functional with the 6-311+G* basis set on all atoms was performed. ADF calculations using the GGA-revPBE method and TZP basis set on all atoms were used to calculate magnetic shielding and EFG tensor information on the optimized structures. Shown in Table 4.5 are the boron EFG and CS tensors calculated using the B3LYP and GGA-revPBE methods for compounds **26** to **36**.

The observed results follow the conclusions made earlier relating the CCBO dihedral angle, the span, and the paramagnetic shielding contributions. In cases where the compounds have a dihedral angle of nearly zero, the contributions to paramagnetic shielding are small and therefore small spans are observed. In the case of compound **34**, a large dihedral angle is calculated, which correspondingly has a large calculated span. No experimental data were acquired for these compounds. In conclusion, varying the ring system bound to the boron atom will have a notable impact on the calculated NMR parameters. When the ring system leads to the compound having a large dihedral angle, the contributions to paramagnetic shielding increase and a larger span value is observed.

Table 4.5: Calculated EFG and CS tensor parameters for compounds **26** to **36**.[a]

	B3LYP								GGA revPBE				
Sample	C_Q / MHz	η_Q	σ_{calc}	Ω / ppm	κ	α	β	γ	C_Q / MHz	η_Q	σ_{calc}	Ω / ppm	ϕ_{CCBO} / º
26	3.101	0.645	74.975	21.027	0.848	12	0	295	2.821	0.665	71.985	21.563	0
27	3.096	0.634	76.676	23.232	0.551	280	0	185	2.815	0.645	73.779	24.809	0
28	3.036	0.597	75.761	22.238	0.896	193	0	264	2.751	0.615	72.782	23.766	0
29	3.110	0.645	74.659	20.320	0.885	174	0	306	2.832	0.665	71.921	21.797	0
30	2.996	0.693	71.526	14.430	-0.815	149	0	211	2.697	0.715	68.124	9.624	0
31	3.037	0.624	72.547	19.867	-0.370	0	1	360	2.740	0.627	69.447	15.634	2
32	2.950	0.642	76.552	23.440	0.683	269	2	181	2.644	0.677	73.331	24.494	0
33	3.123	0.646	75.108	21.709	0.917	176	0	275	2.848	0.664	72.120	23.449	0
34	3.305	0.528	73.572	34.834	0.991	302	0	58	3.045	0.536	70.052	37.191	90
35	3.103	0.605	75.058	24.358	0.676	211	0	254	2.874	0.623	71.587	26.946	0
36	3.221	0.564	75.840	31.775	0.509	179	16	279	2.944	0.544	72.291	34.202	32

[a] Hybrid DFT calculations were performed using the B3LYP functional and the 6-311+G* basis set on all elements. ADF calculations were performed using the GGA-revPBE functional and the TZP basis set on all elements. ϕ_{CCBO} is defined in Figure 2.25.

In this chapter, a series of six boronic acids and nine boronic acid catechol cyclic esters were studied by ^{11}B SSNMR, their spectra were simulated to extract experimental EFG and CS tensor information, and their NMR parameters were calculated at various levels of theory. It has been shown that the C_Q is the most characteristic NMR parameter amongst these compounds. However, since they are all quite structurally similar to one another, there does not appear to be a clear correlation between calculated and experimental span values. The structural similarities as well as the non-negligible role of diamagnetic shielding make it difficult to correlate calculated σ_{iso} values to observed δ_{iso} values. The effects of various ring systems were studied, and several crystal structures were determined and helped to explain what appears to be multiple boron sites in several of the ^{11}B SSNMR spectra. These compounds, however, follow the trend where when a large calculated ϕ_{CCBO} is observed, the calculated Ω value is correspondingly large. Although no substantial variation was seen in the ^{11}B NMR parameters, these compounds remain an extremely important and useful class of compounds which should be studied and characterized. They possess a wide range of practical applications including hydrogen storage and catalysis.

4.3 Experimental

Solid-State NMR Spectroscopy

400 MHz Data: The six boronic acids (4-methoxyphenylboronic acid (**11**), 3,4-dimethoxyphenylboronic acid (**12**), p-tolylboronic acid (**13**), o-tolylboronic acid (**14**), 4-fluorophenylboronic acid (**15**), and 4-chlorophenylboronic acid (**16**)), and nine boronic catechol cyclic esters (4-methoxyphenylboronic acid catechol cyclic ester (**17**), 3,4-dimethoxyphenylboronic acid catechol cyclic ester (**18**), p-tolylboronic acid catechol cyclic ester (**19**), o-tolylboronic acid catechol cyclic ester (**20**), 4-chlorophenylboronic acid catechol cyclic ester (**21**), 4-fluorophenylboronic acid catechol cyclic ester (**22**), 4-methoxyphenylboronic acid catechol cyclic ester (**23**), phenylboronic acid catechol cyclic ester (**24**), and phenylboronic acid catechol cyclic ester trimer (**25**)) studied in this chapter (Figure 4.1) were synthesized and provided by the laboratory of Dr. Kenneth Maly, Wilfrid Laurier University, Waterloo, ON. Some samples were used without further purification, while others required re-crystallization. Solution state ^{1}H NMR experiments were performed on all of the compounds studied in this chapter. The experimental data verify the purity of the compounds since all of the resonance peaks are located at appropriate chemical shift values which represent the chemical environment of the different protons. For those compounds which appeared to have multiple sites in the ^{11}B SSNMR spectrum, re-crystallization was performed by dissolving the compound in a small amount of liquid THF, and then slowly allowing the solvent to evaporate. In these cases, a single crystal was collected for X-ray analysis and the remaining crystals were powdered and packed into a 4mm rotor. The corresponding ^{11}B SSNMR spectra were then acquired for each re-crystallized compound. All experimental details concerning the

SSNMR spectroscopy of the compounds listed above are identical to those used for compounds **1** – **10** and are as outlined in Chapter 2.3.

900 MHz Data: All experimental details concerning the SSNMR spectroscopy of the compounds listed above are identical to those used for compounds **1** – **10** and are as outlined in Chapter 2.3.

Spectral Processing and Simulation: Data were processed and simulated in the same manner as compounds **1** – **10** and are as outlined in Chapter 2.3. Of the compounds studied, X-ray crystal structures are available for compounds **11**, **12**, **21**, and **22**; these structures indicate a single crystallographically unique boron site. Boron-11 NMR spectra acquired strongly suggest that there is a single unique boron site for all other compounds studied as well. As such, all spectra were simulated using a single boron site for each compound except where noted.

Quantum Chemical Calculations

All computational details for the compounds listed above are identical to those used for compounds **1** – **10** and are as outlined in Chapter 2.3. Calculations employing the RHF method were not performed on these compounds. Analogous calculations were also carried out using ADF[72] employing the GGA-revPBE DFT method, TZ2P basis set on all atoms, and the VWN LDA.[84]

Crystallography

Crystals of compounds **11**, **12**, **21**, and **22** were grown from slow evaporation of saturated solutions of THF. Single crystals were mounted on a glass fiber or plastic mesh

with viscous oil and flash cooled to the data collection temperature. Unit cell measurements and intensity data collections were performed on a Bruker-AXS SMART 1k or APEX CCD diffractometer using graphite monochromated Mo-Kα radiation (λ = 0.71073 Å). Unit cell parameters were obtained from 60 data frames, 0.3° ω, from three different sections of the Ewald sphere. The unit cell parameters, equivalent reflections, and systematic absences in the diffraction data are consistent with space groups *P*21/*n* for **11**, *P*21/*c* for **12**, *P*21/*c* for **21**, and *P*21/*n* for **22**. The data-sets were treated with SADABS absorption corrections based on redundant multiscan data.[85] The crystal data and refinement parameters for compounds **11**, **12**, **21**, and **22** are listed in Appendix A. The structures were solved using direct methods and refined with full-matrix, least-squares procedures on *F*2. All non-hydrogen atoms were refined with anisotropic displacement parameters. All hydrogen atoms were treated as idealized contributions. The C–C and C–O bond distances of the THF solvent molecule were restrained with the commands DFIX and SADI and the thermals were restrained with the command SIMU. Atomic scattering factors and anomalous dispersion coefficients are contained in various versions of the SHELXTL program library.[85]

Chapter 5

Conclusions

In this study, ^{11}B CS and EFG tensor information was successfully measured from the ^{11}B SSNMR spectra acquired for twenty-five boron compounds: eleven boronic acids, five boronic esters, and nine boronic acid catechol cyclic esters. Signal enhancement techniques were successfully applied and enhancement factors of up to 1.42 were achieved for modified-QCPMG, whereas factors of 1.80 to 2.95 were achieved for DFS modified-QCPMG, relative to the QCPMG sequence alone. The C_Q and Ω values were found to be larger, on average, for boronic acids (**1** – **5**) than for esters (**6** – **10**) for the compounds studied in Chapter 2. For the compounds studied in Chapter 4, the C_Q values were always larger for the boronic acids (**11** – **16**) than for the boronic acid catechol cyclic esters (**17** – **25**). For boronic acids **1** - **5**, the span has an average value of 30.8 ppm, while for the five boronic esters **6** - **10**, the average value is 17.8 ppm. In the case of ^{11}B quadrupolar coupling constants, the average value is 3.0 MHz for boronic acids **1** - **5** and 2.8 MHz for boronic esters **6** - **10**. For boronic acids **11** - **16**, the span has an average value of 22.8 ppm, while for the boronic acid catechol cyclic esters **17** - **25**, the average value is 23.7 ppm. In the case of ^{11}B quadrupolar coupling constants, the average value is 3.2 MHz for boronic acids **11** - **16** and 2.7 MHz for boronic acid catechol cyclic esters **17** - **25**. The ranges associated with C_Q and δ_{iso} are small relative to their absolute magnitudes from compound to compound. However, for compounds **1** – **10**, the CS tensor span exhibits a significant relative range (75 %), and is the most characteristic NMR parameter to relate the molecular and electronic structure. For compounds **11** – **25**, there is little variation in the NMR parameters. This is due to the

fact that there is little structural variation between the compounds. The change in substituents on the aromatic ring is too distant from the boron nucleus to be felt. Because there is no bulky group near the boron nucleus to alter the dihedral angle, it is similarly small from compound to compound and all of the Ω values are similar. It has been advantageous to acquire data at a high magnetic field strength as the effects of CSA could be more precisely quantified.

Good correlation between experimental and GGA revPBE calculated spans, as well as between the calculated isotropic shielding and experimental chemical shift values was observed for compounds **1** – **10**, but not for compounds **11** - **25**. The span was shown to be positively correlated with ϕ_{CCBO} in a model boronic acid over the range of 0 to 90 degrees. This is true regardless of whether hydrogen bonding is taking place, although Ω does not increase as steeply with ϕ_{CCBO} when hydrogen bonding is occurring. The hydrogen bonding interaction is correlated with a decrease in the total paramagnetic contribution to the isotropic magnetic shielding and a decrease in the span. Contrary to the situation typically seen for larger spans, the diamagnetic part of the shielding tensor was shown to play a key role in explaining the observed trends in CSA. The presence of an electron-withdrawing group substituted on a model boronic acid resulted in an increase in the calculated Ω. Finally, the type of ring system that the boron atom is located in will have an impact on the simulated NMR parameters. There must be adequate structural variation for a change in the NMR parameters to be observed.

It has been shown that the boron chemical shift tensor in boronic acids, and particularly the span of the CS tensor, is governed by a delicate interplay of several competing factors, including hydrogen bonding, dihedral angle, and the various electron-

donating or withdrawing substituents bound to the aromatic ring. It is therefore speculated that future ^{11}B SSNMR experiments performed on similar materials will be most beneficial in comparative studies, where specific individual changes in structure may be probed and characterized.

Perhaps the most important point to be made is that SSNMR is an invaluable tool that can be applied to boron (and other) systems to provide important structural information and to learning important data about the local boron environment which can provide insights into the molecular and electronic environment. Consider a case where crystallographic data is not available for a particular compound which cannot be crystallized or it is impractical to do so. The structure is not known but the results here show that predictions can be made to relate the type of compound being studied to a particular NMR parameter. Chapter 2 shows that span can distinguish between boronic acids and boronic esters when they are structurally different, and Chapter 4 shows that the C_Q can distinguish the type of compound, i.e. boronic acid vs. boronic acid catechol cyclic ester, when they are structurally similar.

As outlined in Chapter 4, the boronic acid and ester compounds studied in this thesis can be utilized as building blocks in supramolecular systems including COFs and MOFs. More specifically, boron serves as an important component in COFs that can be used for applications such as hydrogen storage or in catalytic transformations. This being the case, characterizing SSNMR tensors of potential building blocks in the COFs, namely the compounds studied in this thesis, is a very useful endeavor. In fact, it is ^{11}B SSNMR that is used to identify the local environment of the boron nucleus and to assist in identifying the structure of such COFs and the units of which they are composed.

If studying a system where the abundance of boron is not an issue, routine pulse sequences such as a Hahn-echo can be used to acquire both static and MAS spectra which can be used to probe the structure. If, however, a dilute system of low abundance is being studied, signal enhancement techniques such as DFS or QCPMG can be applied to the system to achieve greater signal in fewer scans. The use of SSNMR, as opposed to liquid NMR can provide much more useful data about the nucleus being studied. For example, one can learn important information about the magnetic shielding or EFG tensor. In the context of this thesis, SSNMR parameters such as span can be simulated from the experimental spectrum. This NMR parameter can be related to calculated NMR interactions such as paramagnetic shielding. It is this contribution to paramagnetic shielding that can be used to relate the NMR parameters to electronic properties such as the bonding environment or MO orientations. In general, SSNMR is an extremely important technique which can be used to gain a vast amount of data for many different nuclei and this information can be used to explain structural and electronic features present in the compound. SSNMR was successfully applied to the boron systems studied here and continues to grow as an important field for studying "more difficult" nuclei such as those with a low gyromagnetic ratio, large quadrupole moment, or low natural abundance.

Future work on the boron compounds discussed in this thesis includes acquisition techniques that would improve resolution. One such example is acquiring data at higher magnetic field strengths. In cases where there are impurities present, or where there are two overlapping boron sites with similar chemical shifts, better resolution would be beneficial in that it would allow for separation of the two sites in question and their

respective NMR parameters could be determined with a smaller experimental error. Acquiring MQMAS spectra of all compounds at both high and low magnetic field strengths may also provide adequate resolution to separate, in the isotropic dimension, any distribution in NMR parameters present within a given boron-containing compound. In addition, all of the compounds in this study should be recrystallized and their crystal structures determined. Of all the compounds where the crystal structure does exist, there is only one boron site. However, that does not necessarily mean that all of the compounds in this study possess one site. There is a possibility that there are multiple sites present which overlap each other and have similar NMR parameters to one another. In addition, procedures to develop these boron-containing compounds into supramolecules such as COFs should be developed. If this is a possibility for any or all of the compounds studied in this thesis, they could be functionalized to carry out a desired action in such a framework.

In the broader context of SSNMR in general, there is still much to be done. There are many "more difficult" nuclei that have not been studied yet due to their low natural abundance, large quadrupole moment, or low gyromagnetic ratio. However, as time goes on, higher magnetic fields are becoming accessible, therefore increasing the number of NMR active nuclei which can be routinely studied. Higher magnetic field strengths reduce the broadening originating from the quadrupolar interaction since this broadening scales inversely with magnetic field strength. In cases where the system is dominated by the QI, but CSA is also present, this is extremely beneficial. Also, new signal enhancement techniques are constantly being developed which will allow for acquisition of difficult spectra in less time. Systems that were previously deemed impractical due to

their low receptivity are becoming more and more practical. Characterizing the magnetic shielding and EFG tensors in such systems is becoming increasingly realistic as this field continues to grow and flourish.

Appendix A – Crystal Structure Data

Table A1: Crystal data and structure refinement for **11**.

Identification code	**11**
Empirical formula	$C_7H_9BO_3$
Formula weight	151.95
Temperature	200(2) K
Wavelength	0.71073 Å
Crystal system, space group	Monoclinic, *P*2(1)/n
Unit cell dimensions	a = 11.0935(9) Å alpha = 90 deg. b = 5.0442(3) Å beta = 111.133(5) deg. c = 13.8754(10) Å gamma = 90 deg.
Volume	724.22(9) $Å^3$
Z, Calculated density	4, 1.394 mg/m^3
Absorption coefficient	0.105 mm^{-1}
F(000)	320
Crystal size	0.21 x 0.18 x 0.16 mm
Theta range for data collection	2.03 to 28.33 deg.
Limiting indices	-12<=h<=14, -6<=k<=6, -18<=l<=18
Reflections collected / unique	6426 / 1778 [R(int) = 0.0269]
Completeness to theta = 28.33	98.3 %
Absorption correction	Semi-empirical from equivalents
Max. and min. transmission	0.9834 and 0.9783
Refinement method	Full-matrix least-squares on F^2
Data / restraints / parameters	1778 / 0 / 100

Goodness-of-fit on F^2	1.026
Final R indices [$I>2\sigma(I)$]	R1 = 0.0436, wR2 = 0.1181
R indices (all data)	R1 = 0.0592, wR2 = 0.1300
Largest diff. peak and hole	0.426 and -0.249 e. $Å^{-3}$

Table A2: Atomic coordinates (x 10^4) and equivalent isotropic displacement parameters ($Å^2$ x 10^3) for **11**.
U(eq) is defined as one third of the trace of the orthogonalized Uij tensor.

	x	y	z	U(eq)
B(1)	2956(2)	-617(3)	-915(1)	23(1)
O(1)	2421(1)	1417(2)	-1593(1)	28(1)
O(2)	3058(1)	-3045(2)	-1308(1)	29(1)
O(3)	4752(1)	352(2)	3501(1)	33(1)
C(1)	3419(1)	-278(2)	281(1)	22(1)
C(2)	2991(1)	1794(3)	747(1)	26(1)
C(3)	3397(2)	2067(2)	1815(1)	26(1)
C(4)	4277(1)	263(3)	2444(1)	24(1)
C(5)	4730(1)	-1809(3)	2004(1)	26(1)
C(6)	4299(1)	-2071(3)	942(1)	24(1)
C(7)	4318(2)	2487(3)	3970(1)	38(1)

Table A3: Bond lengths [Å] and angles [deg] for **11**.

B(1)-O(2)	1.3616(16)
B(1)-O(1)	1.3736(17)
B(1)-C(1)	1.5602(17)
O(3)-C(4)	1.3694(14)
O(3)-C(7)	1.4287(17)
C(1)-C(2)	1.3987(17)
C(1)-C(6)	1.4020(18)
C(2)-C(3)	1.3913(17)
C(3)-C(4)	1.3883(19)

C(4)-C(5)	1.3919(18)
C(5)-C(6)	1.3818(16)
O(2)-B(1)-O(1)	118.42(11)
O(2)-B(1)-C(1)	118.77(11)
O(1)-B(1)-C(1)	122.80(11)
C(4)-O(3)-C(7)	116.76(11)
C(2)-C(1)-C(6)	116.86(11)
C(2)-C(1)-B(1)	122.49(12)
C(6)-C(1)-B(1)	120.65(11)
C(3)-C(2)-C(1)	122.18(12)
C(4)-C(3)-C(2)	119.24(12)
O(3)-C(4)-C(3)	124.30(11)
O(3)-C(4)-C(5)	115.70(11)
C(3)-C(4)-C(5)	120.00(11)
C(6)-C(5)-C(4)	119.86(12)
C(5)-C(6)-C(1)	121.84(12)

Symmetry transformations used to generate equivalent atoms:

Table A4: Anisotropic displacement parameters ($Å^2$ x 10^3) for **11**.
The anisotropic displacement factor exponent takes the form:
$-2\pi^2$ [$h^2 a^{*2}$ U11 + ... + 2 h k a* b* U12]

	U11	U22	U33	U23	U13	U12
B(1)	31(1)	20(1)	19(1)	-1(1)	10(1)	-3(1)
O(1)	48(1)	18(1)	19(1)	0(1)	10(1)	2(1)
O(2)	50(1)	18(1)	19(1)	-1(1)	11(1)	0(1)
O(3)	47(1)	32(1)	18(1)	-2(1)	9(1)	5(1)
C(1)	30(1)	18(1)	19(1)	-1(1)	10(1)	-3(1)
C(2)	37(1)	18(1)	22(1)	1(1)	11(1)	2(1)
C(3)	38(1)	19(1)	22(1)	-1(1)	13(1)	2(1)
C(4)	32(1)	23(1)	19(1)	-1(1)	9(1)	-4(1)
C(5)	32(1)	24(1)	22(1)	1(1)	8(1)	2(1)
C(6)	32(1)	20(1)	23(1)	-2(1)	12(1)	0(1)
C(7)	60(1)	31(1)	23(1)	-6(1)	16(1)	2(1)

Table A5: Hydrogen coordinates (x 10^4) and isotropic displacement parameters ($Å^2$ x 10^3) for **11**.

	x	y	z	U(eq)
H(1A)	2540	2858	-1268	43
H(2B)	2780	-2964	-1956	44
H(2A)	2404	3056	320	31
H(3A)	3076	3471	2110	31
H(5A)	5334	-3041	2434	32
H(6A)	4607	-3506	652	29
H(7A)	4719	2345	4724	57
H(7B)	3376	2402	3765	57
H(7C)	4562	4178	3744	57

Table A6: Torsion angles [deg] for **11**.

O(2)-B(1)-C(1)-C(2)	-158.83(13)
O(1)-B(1)-C(1)-C(2)	19.6(2)
O(2)-B(1)-C(1)-C(6)	21.3(2)
O(1)-B(1)-C(1)-C(6)	-160.25(13)
C(6)-C(1)-C(2)-C(3)	-0.9(2)
B(1)-C(1)-C(2)-C(3)	179.25(13)
C(1)-C(2)-C(3)-C(4)	1.4(2)
C(7)-O(3)-C(4)-C(3)	-1.2(2)
C(7)-O(3)-C(4)-C(5)	178.98(13)
C(2)-C(3)-C(4)-O(3)	179.36(12)
C(2)-C(3)-C(4)-C(5)	-0.9(2)
O(3)-C(4)-C(5)-C(6)	179.59(12)
C(3)-C(4)-C(5)-C(6)	-0.2(2)
C(4)-C(5)-C(6)-C(1)	0.8(2)
C(2)-C(1)-C(6)-C(5)	-0.2(2)
B(1)-C(1)-C(6)-C(5)	179.65(13)

Table A7: Crystal data and structure refinement for **12**.

Identification code	**12**
Empirical formula	$C_8H_{11}BO_4$
Formula weight	181.98
Temperature	200(2) K
Wavelength	0.71073 Å
Crystal system, space group	Monoclinic, *P*2(1)/c
Unit cell dimensions	a = 5.5550(18) Å alpha = 90 deg. b = 9.532(3) Å beta = 95.269(4) deg. c = 17.406(5) Å gamma = 90 deg.
Volume	917.8(5) $Å^3$
Z, Calculated density	4, 1.317 mg/m^3
Absorption coefficient	0.103 mm^{-1}
F(000)	384
Crystal size	0.27 x 0.22 x 0.22 mm
Theta range for data collection	2.35 to 26.43 deg.
Limiting indices	-6<=h<=5, -11<=k<=4, -17<=l<=21
Reflections collected / unique	3331 / 1836 [R(int) = 0.0122]
Completeness to theta = 26.43	97.4 %
Absorption correction	Semi-empirical from equivalents
Max. and min. transmission	0.9778 and 0.9728
Refinement method	Full-matrix least-squares on F^2
Data / restraints / parameters	1836 / 0 / 119
Goodness-of-fit on F^2	1.047

Final R indices [I>2σ(I)]	R1 = 0.0354, wR2 = 0.1046
R indices (all data)	R1 = 0.0394, wR2 = 0.1088
Extinction coefficient	0.037(6)
Largest diff. peak and hole	0.275 and -0.188 e. $Å^{-3}$

Table A8: Atomic coordinates (x 10^4) and equivalent isotropic displacement parameters ($Å^2$ x 10^3) for **12**.
U(eq) is defined as one third of the trace of the orthogonalized Uij tensor.

	x	y	z	U(eq)
B(1)	7984(3)	6574(1)	4413(1)	29(1)
O(1)	933(2)	10277(1)	2875(1)	35(1)
O(2)	3932(2)	9045(1)	2074(1)	34(1)
O(3)	8605(2)	6753(1)	5178(1)	38(1)
O(4)	9024(2)	5490(1)	4045(1)	36(1)
C(1)	6072(2)	7597(1)	3998(1)	29(1)
C(2)	5878(2)	7810(1)	3194(1)	27(1)
C(3)	4191(2)	8728(1)	2846(1)	26(1)
C(4)	2556(2)	9423(1)	3286(1)	28(1)
C(5)	2718(3)	9222(2)	4076(1)	37(1)
C(6)	4481(3)	8326(2)	4424(1)	37(1)
C(7)	-769(2)	11009(2)	3299(1)	39(1)
C(8)	5745(3)	8538(2)	1616(1)	42(1)

Table A9: Bond lengths [Å] and angles [deg] for **12**.

B(1)-O(3)	1.3554(16)
B(1)-O(4)	1.3705(17)
B(1)-C(1)	1.5686(18)
O(1)-C(4)	1.3672(15)
O(1)-C(7)	1.4329(16)
O(2)-C(3)	1.3714(14)

O(2)-C(8)	1.4257(16)
C(1)-C(6)	1.3912(18)
C(1)-C(2)	1.4088(16)
C(2)-C(3)	1.3810(17)
C(3)-C(4)	1.4071(17)
C(4)-C(5)	1.3822(18)
C(5)-C(6)	1.3951(19)

O(3)-B(1)-O(4)	118.27(11)
O(3)-B(1)-C(1)	118.32(11)
O(4)-B(1)-C(1)	123.39(11)
C(4)-O(1)-C(7)	117.06(10)
C(3)-O(2)-C(8)	117.20(10)
C(6)-C(1)-C(2)	117.62(11)
C(6)-C(1)-B(1)	120.11(11)
C(2)-C(1)-B(1)	122.26(11)
C(3)-C(2)-C(1)	120.92(11)
O(2)-C(3)-C(2)	125.12(11)
O(2)-C(3)-C(4)	114.53(10)
C(2)-C(3)-C(4)	120.35(10)
O(1)-C(4)-C(5)	125.64(11)
O(1)-C(4)-C(3)	114.98(10)
C(5)-C(4)-C(3)	119.36(11)
C(6)-C(5)-C(4)	119.73(12)
C(5)-C(6)-C(1)	121.94(12)

Symmetry transformations used to generate equivalent atoms:

Table A10: Anisotropic displacement parameters ($Å^2$ x 10^3) for **12**.
The anisotropic displacement factor exponent takes the form:
$-2\pi^2 [h^2 a^{*2} U11 + ... + 2 h k a^* b^* U12]$

	U11	U22	U33	U23	U13	U12
B(1)	34(1)	29(1)	24(1)	0(1)	-1(1)	1(1)
O(1)	36(1)	34(1)	34(1)	2(1)	-1(1)	10(1)
O(2)	42(1)	38(1)	22(1)	5(1)	4(1)	11(1)
O(3)	52(1)	39(1)	23(1)	-2(1)	-5(1)	15(1)
O(4)	46(1)	36(1)	23(1)	-4(1)	-8(1)	11(1)
C(1)	35(1)	28(1)	24(1)	0(1)	-2(1)	2(1)
C(2)	32(1)	26(1)	25(1)	-2(1)	2(1)	2(1)

C(3)	32(1)	26(1)	21(1)	1(1)	-1(1)	-3(1)
C(4)	30(1)	25(1)	30(1)	1(1)	-2(1)	2(1)
C(5)	41(1)	41(1)	29(1)	-3(1)	6(1)	10(1)
C(6)	46(1)	42(1)	22(1)	2(1)	2(1)	9(1)
C(7)	36(1)	33(1)	49(1)	-3(1)	2(1)	8(1)
C(8)	47(1)	53(1)	28(1)	6(1)	9(1)	10(1)

Table A11: Hydrogen coordinates (x 10^4) and isotropic displacement parameters ($Å^2$ x 10^3) for **12**.

	x	y	z	U(eq)
H(3A)	9633	6146	5333	58
H(4A)	8265	5360	3611	53
H(2A)	6923	7315	2886	33
H(5A)	1635	9693	4380	44
H(6A)	4597	8210	4968	44
H(7A)	-1828	11583	2944	59
H(7B)	100	11615	3685	59
H(7C)	-1745	10329	3557	59
H(8A)	5365	8835	1079	63
H(8B)	5796	7511	1641	63
H(8C)	7321	8919	1813	63

Table A12: Torsion angles [deg] for **12**.

O(3)-B(1)-C(1)-C(6)	-21.61(19)
O(4)-B(1)-C(1)-C(6)	157.08(13)
O(3)-B(1)-C(1)-C(2)	158.85(12)
O(4)-B(1)-C(1)-C(2)	-22.46(19)
C(6)-C(1)-C(2)-C(3)	1.04(18)
B(1)-C(1)-C(2)-C(3)	-179.41(11)
C(8)-O(2)-C(3)-C(2)	-8.97(18)
C(8)-O(2)-C(3)-C(4)	171.16(11)
C(1)-C(2)-C(3)-O(2)	177.27(11)
C(1)-C(2)-C(3)-C(4)	-2.87(18)
C(7)-O(1)-C(4)-C(5)	-1.05(18)
C(7)-O(1)-C(4)-C(3)	-179.95(11)

O(2)-C(3)-C(4)-O(1)	1.48(15)
C(2)-C(3)-C(4)-O(1)	-178.40(11)
O(2)-C(3)-C(4)-C(5)	-177.49(11)
C(2)-C(3)-C(4)-C(5)	2.63(18)
O(1)-C(4)-C(5)-C(6)	-179.45(12)
C(3)-C(4)-C(5)-C(6)	-0.6(2)
C(4)-C(5)-C(6)-C(1)	-1.2(2)
C(2)-C(1)-C(6)-C(5)	1.0(2)
B(1)-C(1)-C(6)-C(5)	-178.54(13)

Table A13: Crystal data and structure refinement for **21**.

Identification code	**21**
Empirical formula	$C_{13}H_{11}BO_2$
Formula weight	210.03
Temperature	296(2) K
Wavelength	0.71073 Å
Crystal system, space group	Monoclinic, *P*2(1)/c
Unit cell dimensions	a = 17.881(3) Å alpha = 90 deg. b = 5.0462(9) Å beta = 100.382(9) deg. c = 12.544(2) Å gamma = 90 deg.
Volume	1113.4(3) $Å^3$
Z, Calculated density	4, 1.253 mg/m^3
Absorption coefficient	0.082 mm^{-1}
F(000)	440
Crystal size	0.12 x 0.11 x 0.05 mm
Theta range for data collection	2.32 to 24.77 deg.
Limiting indices	-21<=h<=21, -5<=k<=5, -14<=l<=14
Reflections collected / unique	15231 / 1872 [R(int) = 0.0460]
Completeness to theta = 24.77	98.6 %
Absorption correction	Semi-empirical from equivalents
Max. and min. transmission	0.9959 and 0.9902
Refinement method	Full-matrix least-squares on F^2
Data / restraints / parameters	1872 / 0 / 145
Goodness-of-fit on F^2	1.061

Final R indices [I>2σ(I)]	R1 = 0.0485, wR2 = 0.1251
R indices (all data)	R1 = 0.0692, wR2 = 0.1413
Largest diff. peak and hole	0.152 and -0.140 e. $Å^{-3}$

Table A14: Atomic coordinates (x 10^4) and equivalent isotropic displacement parameters ($Å^2$ x 10^3) for **21**.
U(eq) is defined as one third of the trace of the orthogonalized Uij tensor.

	x	y	z	U(eq)
B(1)	7645(1)	1027(5)	548(2)	51(1)
O(1)	7649(1)	-70(3)	1562(1)	58(1)
O(2)	8210(1)	-76(3)	67(1)	60(1)
C(1)	7083(1)	3159(4)	33(2)	50(1)
C(2)	7077(1)	4069(5)	-1016(2)	60(1)
C(3)	6559(1)	5943(5)	-1489(2)	64(1)
C(4)	6025(1)	6980(4)	-933(2)	59(1)
C(5)	6030(1)	6089(5)	110(2)	68(1)
C(6)	6548(1)	4218(5)	584(2)	62(1)
C(7)	5464(1)	9029(5)	-1446(2)	80(1)
C(8)	8561(1)	-1937(4)	800(2)	56(1)
C(9)	9141(1)	-3633(6)	700(2)	80(1)
C(10)	9373(2)	-5342(5)	1563(2)	85(1)
C(11)	9036(2)	-5320(5)	2457(2)	82(1)
C(12)	8450(1)	-3614(5)	2544(2)	71(1)
C(13)	8226(1)	-1920(4)	1696(2)	54(1)

Table A15: Bond lengths [Å] and angles [deg] for **21**.

B(1)-O(2)	1.383(3)
B(1)-O(1)	1.387(3)
B(1)-C(1)	1.533(3)
O(1)-C(13)	1.380(2)
O(2)-C(8)	1.383(2)
C(1)-C(6)	1.386(3)

C(1)-C(2)	1.391(3)
C(2)-C(3)	1.381(3)
C(3)-C(4)	1.382(3)
C(4)-C(5)	1.382(3)
C(4)-C(7)	1.503(3)
C(5)-C(6)	1.379(3)
C(8)-C(13)	1.365(3)
C(8)-C(9)	1.369(3)
C(9)-C(10)	1.388(4)
C(10)-C(11)	1.367(4)
C(11)-C(12)	1.376(4)
C(12)-C(13)	1.367(3)

O(2)-B(1)-O(1)	110.89(18)
O(2)-B(1)-C(1)	124.99(18)
O(1)-B(1)-C(1)	124.12(18)
C(13)-O(1)-B(1)	105.17(15)
B(1)-O(2)-C(8)	105.20(15)
C(6)-C(1)-C(2)	117.1(2)
C(6)-C(1)-B(1)	121.31(18)
C(2)-C(1)-B(1)	121.53(18)
C(3)-C(2)-C(1)	121.5(2)
C(2)-C(3)-C(4)	120.9(2)
C(5)-C(4)-C(3)	117.8(2)
C(5)-C(4)-C(7)	121.3(2)
C(3)-C(4)-C(7)	120.8(2)
C(6)-C(5)-C(4)	121.4(2)
C(5)-C(6)-C(1)	121.2(2)
C(13)-C(8)-C(9)	122.1(2)
C(13)-C(8)-O(2)	109.29(18)
C(9)-C(8)-O(2)	128.6(2)
C(8)-C(9)-C(10)	116.2(2)
C(11)-C(10)-C(9)	121.4(2)
C(10)-C(11)-C(12)	121.8(2)
C(13)-C(12)-C(11)	116.7(2)
C(8)-C(13)-C(12)	121.8(2)
C(8)-C(13)-O(1)	109.44(17)
C(12)-C(13)-O(1)	128.7(2)

Symmetry transformations used to generate equivalent atoms:

Table A16: Anisotropic displacement parameters ($Å^2$ x 10^3) for **21**.
The anisotropic displacement factor exponent takes the form:
$-2\pi^2$ [$h^2 a^{*2}$ U11 + ... + 2 h k a* b* U12]

	U11	U22	U33	U23	U13	U12
B(1)	56(1)	50(1)	46(1)	-4(1)	11(1)	-7(1)
O(1)	67(1)	62(1)	46(1)	2(1)	15(1)	1(1)
O(2)	70(1)	68(1)	45(1)	4(1)	17(1)	12(1)
C(1)	54(1)	49(1)	48(1)	-5(1)	10(1)	-5(1)
C(2)	65(1)	61(1)	57(1)	4(1)	19(1)	5(1)
C(3)	72(1)	60(1)	59(1)	11(1)	13(1)	4(1)
C(4)	59(1)	43(1)	71(1)	-8(1)	4(1)	-3(1)
C(5)	69(1)	65(2)	72(2)	-13(1)	19(1)	9(1)
C(6)	72(1)	64(1)	53(1)	-3(1)	17(1)	4(1)
C(7)	81(2)	58(1)	95(2)	-4(1)	1(1)	10(1)
C(8)	60(1)	54(1)	51(1)	-2(1)	3(1)	1(1)
C(9)	77(2)	84(2)	81(2)	-1(2)	16(1)	19(1)
C(10)	77(2)	67(2)	104(2)	3(2)	-4(2)	14(1)
C(11)	87(2)	62(2)	86(2)	20(1)	-14(2)	-8(1)
C(12)	81(2)	70(2)	58(1)	14(1)	1(1)	-11(1)
C(13)	59(1)	50(1)	50(1)	0(1)	3(1)	-8(1)

Table A17: Hydrogen coordinates (x 10^4) and isotropic displacement parameters ($Å^2$ x 10^3) for **21**.

	x	y	z	U(eq)
H(2A)	7430	3401	-1407	72
H(3A)	6569	6514	-2191	77
H(5A)	5678	6765	501	81
H(6A)	6537	3656	1287	75
H(7A)	4958	8447	-1413	120
H(7B)	5513	9272	-2189	120
H(7C)	5563	10676	-1064	120

H(9A)	9367	-3640	88	97
H(10A)	9767	-6528	1532	102
H(11A)	9206	-6490	3021	99
H(12A)	8217	-3613	3150	85

Table A18: Torsion angles [deg] for **21**.

O(2)-B(1)-O(1)-C(13)	-0.8(2)
C(1)-B(1)-O(1)-C(13)	178.69(18)
O(1)-B(1)-O(2)-C(8)	1.1(2)
C(1)-B(1)-O(2)-C(8)	-178.40(19)
O(2)-B(1)-C(1)-C(6)	-178.06(19)
O(1)-B(1)-C(1)-C(6)	2.5(3)
O(2)-B(1)-C(1)-C(2)	3.4(3)
O(1)-B(1)-C(1)-C(2)	-176.00(19)
C(6)-C(1)-C(2)-C(3)	-0.2(3)
B(1)-C(1)-C(2)-C(3)	178.4(2)
C(1)-C(2)-C(3)-C(4)	0.0(3)
C(2)-C(3)-C(4)-C(5)	0.2(3)
C(2)-C(3)-C(4)-C(7)	179.7(2)
C(3)-C(4)-C(5)-C(6)	-0.2(3)
C(7)-C(4)-C(5)-C(6)	-179.7(2)
C(4)-C(5)-C(6)-C(1)	0.0(4)
C(2)-C(1)-C(6)-C(5)	0.2(3)
B(1)-C(1)-C(6)-C(5)	-178.4(2)
B(1)-O(2)-C(8)-C(13)	-1.0(2)
B(1)-O(2)-C(8)-C(9)	177.9(2)
C(13)-C(8)-C(9)-C(10)	0.0(4)
O(2)-C(8)-C(9)-C(10)	-178.8(2)
C(8)-C(9)-C(10)-C(11)	0.2(4)
C(9)-C(10)-C(11)-C(12)	0.2(4)
C(10)-C(11)-C(12)-C(13)	-0.6(4)
C(9)-C(8)-C(13)-C(12)	-0.5(3)
O(2)-C(8)-C(13)-C(12)	178.47(18)
C(9)-C(8)-C(13)-O(1)	-178.4(2)
O(2)-C(8)-C(13)-O(1)	0.5(2)
C(11)-C(12)-C(13)-C(8)	0.8(3)
C(11)-C(12)-C(13)-O(1)	178.3(2)
B(1)-O(1)-C(13)-C(8)	0.2(2)
B(1)-O(1)-C(13)-C(12)	-177.6(2)

Symmetry transformations used to generate equivalent atoms:

Table A19: Hydrogen bonds for **21** [Å and deg.].

D-H...A	d(D-H)	d(H...A)	d(D...A)	<(DHA)

Table A20: Crystal data and structure refinement for **22**.

Identification code	**22**
Empirical formula	$C_{12}H_8BFO_2$
Formula weight	213.99
Temperature	200(2) K
Wavelength	0.71073 Å
Crystal system, space group	Monoclinic, *P*2(1)/n
Unit cell dimensions	a = 12.362(8) Å alpha = 90 deg. b = 4.735(3) Å beta = 98.611(7) deg. c = 17.487(11) Å gamma = 90 deg.
Volume	1012.0(11) $Å^3$
Z, Calculated density	4, 1.405 mg/m^3
Absorption coefficient	0.105 mm^{-1}
F(000)	440
Crystal size	0.27 x 0.25 x 0.11 mm
Theta range for data collection	2.36 to 24.99 deg.
Limiting indices	-14<=h<=14, -5<=k<=5, -20<=l<=20
Reflections collected / unique	8091 / 1767 [R(int) = 0.0855]
Completeness to theta = 24.99	98.8 %
Absorption correction	Semi-empirical from equivalents
Max. and min. transmission	0.9885 and 0.9722
Refinement method	Full-matrix least-squares on F^2
Data / restraints / parameters	1767 / 0 / 146
Goodness-of-fit on F^2	1.012

Final R indices [I>2σ(I)]	R1 = 0.0558, wR2 = 0.1198
R indices (all data)	R1 = 0.1177, wR2 = 0.1502
Extinction coefficient	0.008(3)
Largest diff. peak and hole	0.194 and -0.183 e. $Å^{-3}$

Table A21: Atomic coordinates (x 10^4) and equivalent isotropic displacement parameters ($Å^2$ x 10^3) for **22**.
U(eq) is defined as one third of the trace of the orthogonalized Uij tensor.

	x	y	z	U(eq)
O(1)	4192(2)	2339(4)	703(1)	43(1)
O(2)	2721(2)	1549(4)	1335(1)	44(1)
F(1)	6199(2)	-7289(4)	3230(1)	71(1)
B(1)	3796(3)	789(7)	1282(2)	40(1)
C(1)	4463(2)	-1396(6)	1804(2)	40(1)
C(2)	5535(2)	-2095(6)	1722(2)	46(1)
C(3)	6128(3)	-4057(7)	2197(2)	52(1)
C(4)	5620(3)	-5336(6)	2757(2)	50(1)
C(5)	4573(3)	-4743(6)	2862(2)	49(1)
C(6)	4002(3)	-2771(6)	2385(2)	46(1)
C(7)	3329(2)	4059(6)	391(2)	41(1)
C(8)	3299(3)	6025(7)	-193(2)	51(1)
C(9)	2327(3)	7473(7)	-384(2)	54(1)
C(10)	1440(3)	7013(7)	-10(2)	55(1)
C(11)	1482(3)	5024(7)	583(2)	50(1)
C(12)	2444(2)	3595(6)	767(2)	40(1)

Table A22: Bond lengths [Å] and angles [deg] for **22**.

O(1)-C(7)	1.387(3)
O(1)-B(1)	1.397(4)
O(2)-B(1)	1.393(4)
O(2)-C(12)	1.393(3)

F(1)-C(4)	1.369(3)
B(1)-C(1)	1.535(5)
C(1)-C(2)	1.394(4)
C(1)-C(6)	1.399(4)
C(2)-C(3)	1.382(4)
C(3)-C(4)	1.380(5)
C(4)-C(5)	1.363(4)
C(5)-C(6)	1.375(4)
C(7)-C(12)	1.376(4)
C(7)-C(8)	1.379(4)
C(8)-C(9)	1.380(4)
C(9)-C(10)	1.376(5)
C(10)-C(11)	1.397(4)
C(11)-C(12)	1.364(4)

C(7)-O(1)-B(1)	105.2(2)
B(1)-O(2)-C(12)	105.6(2)
O(2)-B(1)-O(1)	110.7(3)
O(2)-B(1)-C(1)	124.6(3)
O(1)-B(1)-C(1)	124.7(3)
C(2)-C(1)-C(6)	117.5(3)
C(2)-C(1)-B(1)	122.2(3)
C(6)-C(1)-B(1)	120.3(3)
C(3)-C(2)-C(1)	121.7(3)
C(4)-C(3)-C(2)	117.7(3)
C(5)-C(4)-F(1)	118.6(3)
C(5)-C(4)-C(3)	123.2(3)
F(1)-C(4)-C(3)	118.2(3)
C(4)-C(5)-C(6)	118.1(3)
C(5)-C(6)-C(1)	121.9(3)
C(12)-C(7)-C(8)	121.8(3)
C(12)-C(7)-O(1)	109.7(3)
C(8)-C(7)-O(1)	128.5(3)
C(7)-C(8)-C(9)	116.1(3)
C(10)-C(9)-C(8)	122.3(3)
C(9)-C(10)-C(11)	121.1(3)
C(12)-C(11)-C(10)	116.3(3)
C(11)-C(12)-C(7)	122.4(3)
C(11)-C(12)-O(2)	128.8(3)
C(7)-C(12)-O(2)	108.8(3)

Symmetry transformations used to generate equivalent atoms:

Table A23: Anisotropic displacement parameters ($Å^2$ x 10^3) for **22**.
The anisotropic displacement factor exponent takes the form:
$-2\pi^2$ [$h^2 a^{*2}$ U11 + ... + 2 h k a* b* U12]

	U11	U22	U33	U23	U13	U12
O(1)	42(1)	36(1)	54(1)	2(1)	19(1)	-1(1)
O(2)	46(1)	35(1)	54(1)	-2(1)	18(1)	-4(1)
F(1)	86(2)	50(1)	72(1)	4(1)	-2(1)	13(1)
B(1)	39(2)	31(2)	53(2)	-11(2)	17(2)	-10(2)
C(1)	45(2)	28(2)	50(2)	-8(2)	14(2)	-4(1)
C(2)	47(2)	35(2)	60(2)	-1(2)	19(2)	-3(2)
C(3)	45(2)	40(2)	73(2)	-10(2)	14(2)	0(2)
C(4)	61(2)	32(2)	55(2)	-6(2)	2(2)	1(2)
C(5)	60(2)	37(2)	54(2)	2(2)	17(2)	-3(2)
C(6)	47(2)	36(2)	56(2)	-3(2)	20(2)	-2(2)
C(7)	41(2)	29(2)	53(2)	-6(2)	9(2)	-3(1)
C(8)	56(2)	42(2)	58(2)	2(2)	17(2)	-5(2)
C(9)	61(2)	38(2)	61(2)	2(2)	4(2)	-5(2)
C(10)	50(2)	39(2)	74(2)	-9(2)	-1(2)	2(2)
C(11)	44(2)	40(2)	70(2)	-11(2)	17(2)	-3(2)
C(12)	45(2)	29(2)	49(2)	-6(2)	12(2)	-4(2)

Table A24: Hydrogen coordinates (x 10^4) and isotropic displacement parameters ($Å^2$ x 10^3) for **22**.

	x	y	z	U(eq)
H(2A)	5866	-1199	1329	56
H(3A)	6861	-4510	2140	63
H(5A)	4248	-5666	3253	59
H(6A)	3272	-2329	2453	55
H(8A)	3911	6363	-450	61
H(9A)	2269	8835	-787	65

H(10A)	788	8066	-158	66
H(11A)	874	4685	845	61

Table A25: Torsion angles [deg] for **22**.

C(12)-O(2)-B(1)-O(1)	0.7(3)
C(12)-O(2)-B(1)-C(1)	179.3(3)
C(7)-O(1)-B(1)-O(2)	-0.7(3)
C(7)-O(1)-B(1)-C(1)	-179.2(3)
O(2)-B(1)-C(1)-C(2)	179.5(3)
O(1)-B(1)-C(1)-C(2)	-2.2(4)
O(2)-B(1)-C(1)-C(6)	-0.5(4)
O(1)-B(1)-C(1)-C(6)	177.9(3)
C(6)-C(1)-C(2)-C(3)	-0.3(4)
B(1)-C(1)-C(2)-C(3)	179.7(3)
C(1)-C(2)-C(3)-C(4)	0.5(4)
C(2)-C(3)-C(4)-C(5)	-0.3(5)
C(2)-C(3)-C(4)-F(1)	179.8(2)
F(1)-C(4)-C(5)-C(6)	179.8(3)
C(3)-C(4)-C(5)-C(6)	-0.1(5)
C(4)-C(5)-C(6)-C(1)	0.3(4)
C(2)-C(1)-C(6)-C(5)	-0.1(4)
B(1)-C(1)-C(6)-C(5)	179.9(3)
B(1)-O(1)-C(7)-C(12)	0.4(3)
B(1)-O(1)-C(7)-C(8)	179.1(3)
C(12)-C(7)-C(8)-C(9)	-0.7(4)
O(1)-C(7)-C(8)-C(9)	-179.3(3)
C(7)-C(8)-C(9)-C(10)	0.6(4)
C(8)-C(9)-C(10)-C(11)	-0.3(5)
C(9)-C(10)-C(11)-C(12)	0.1(4)
C(10)-C(11)-C(12)-C(7)	-0.2(4)
C(10)-C(11)-C(12)-O(2)	178.9(3)
C(8)-C(7)-C(12)-C(11)	0.5(4)
O(1)-C(7)-C(12)-C(11)	179.4(2)
C(8)-C(7)-C(12)-O(2)	-178.8(2)
O(1)-C(7)-C(12)-O(2)	0.1(3)
B(1)-O(2)-C(12)-C(11)	-179.7(3)
B(1)-O(2)-C(12)-C(7)	-0.5(3)

Symmetry transformations used to generate equivalent atoms:

Table A26: Hydrogen bonds for **22** [Å and deg.].

D-H...A	d(D-H)	d(H...A)	d(D...A)	<(DHA)

Appendix B – Calculation Input Information

Sample ADF calculation input file for **16**.

```
#!/bin/sh

$ADFBIN/adf << eor
Title PF3 - scf

Basis
 Type TZP
End

Symmetry NOSYM

Atoms
1. C              1.05849800    1.21342100   -0.00000600
2. C             -0.33345900    1.20232900   -0.00000100
3. C             -1.05770800    0.00000300    0.00001200
4. C             -0.33345900   -1.20232600    0.00001500
5. C              1.05849600   -1.21341900    0.00000800
6. H              1.60923700    2.14679100   -0.00001300
7. H             -0.86853000    2.14598600   -0.00000300
8. H             -0.86853300   -2.14598100    0.00002400
9. H              1.60923700   -2.14678800    0.00001100
10. B            -2.61693200    0.00000000    0.00002300
11. O            -3.26513300   -1.21163800    0.00000000
12. H            -4.22742900   -1.19381400   -0.00001100
13. O            -3.26513700    1.21163500   -0.00000700
14. H            -4.22743400    1.19380900   -0.00003600
15. C             1.74038200    0.00000100   -0.00000200
16. Cl            3.50022200   -0.00000200   -0.00001100
End

Integration 6.0

qtens

XC
  GGA revPBE
End

locorb
end
```

```
End Input
eor

$ADFBIN/epr << eor
CLGEPR
  NUCLEI ALL
  OUTPUT
    SIZE LARGE
  SUBEND
END
END INPUT
eor

cp TAPE21 chloro4nmr.t21
```

Appendix C – MQMAS Spectra

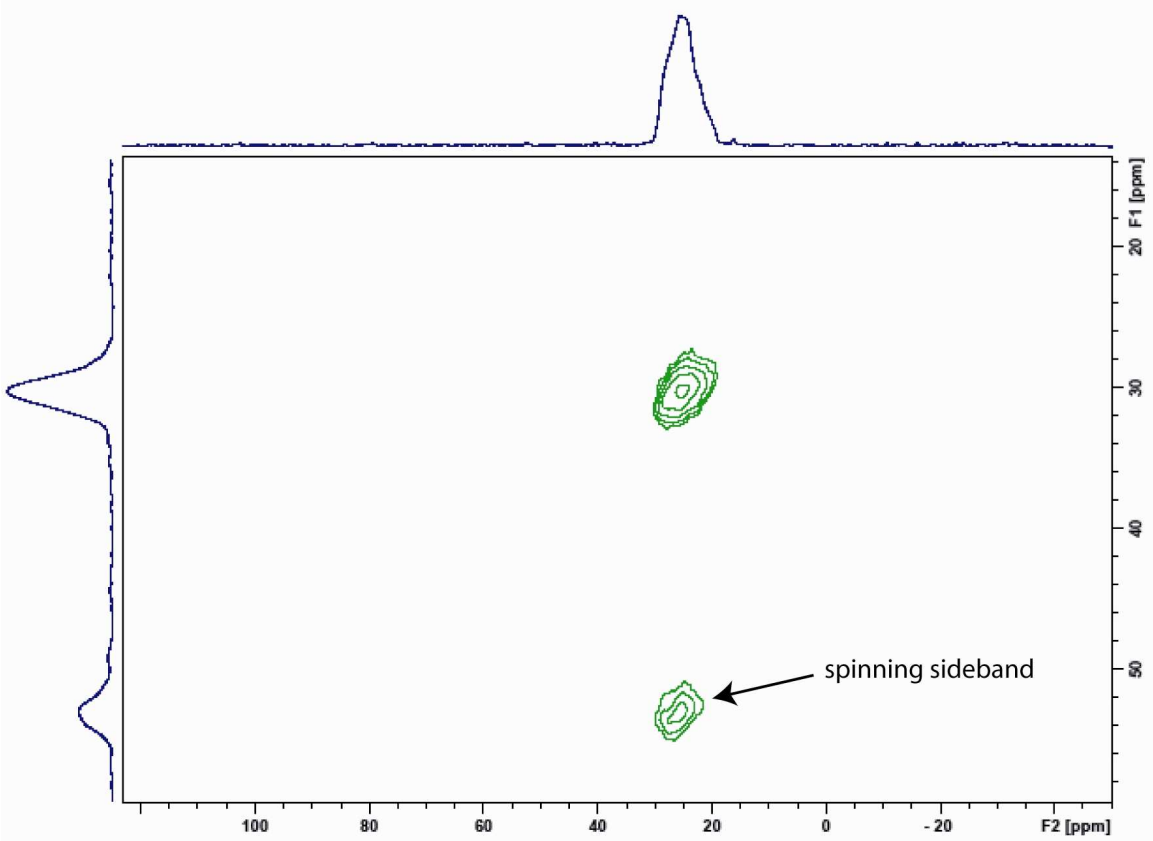

Figure A1: Two-dimensional ^{11}B MQMAS spectrum of compound **21**. The signal for this compound can be seen in the isotropic dimension along the F1 axis. Shown at ~ 54 ppm along the F1 axis is a spinning sideband.

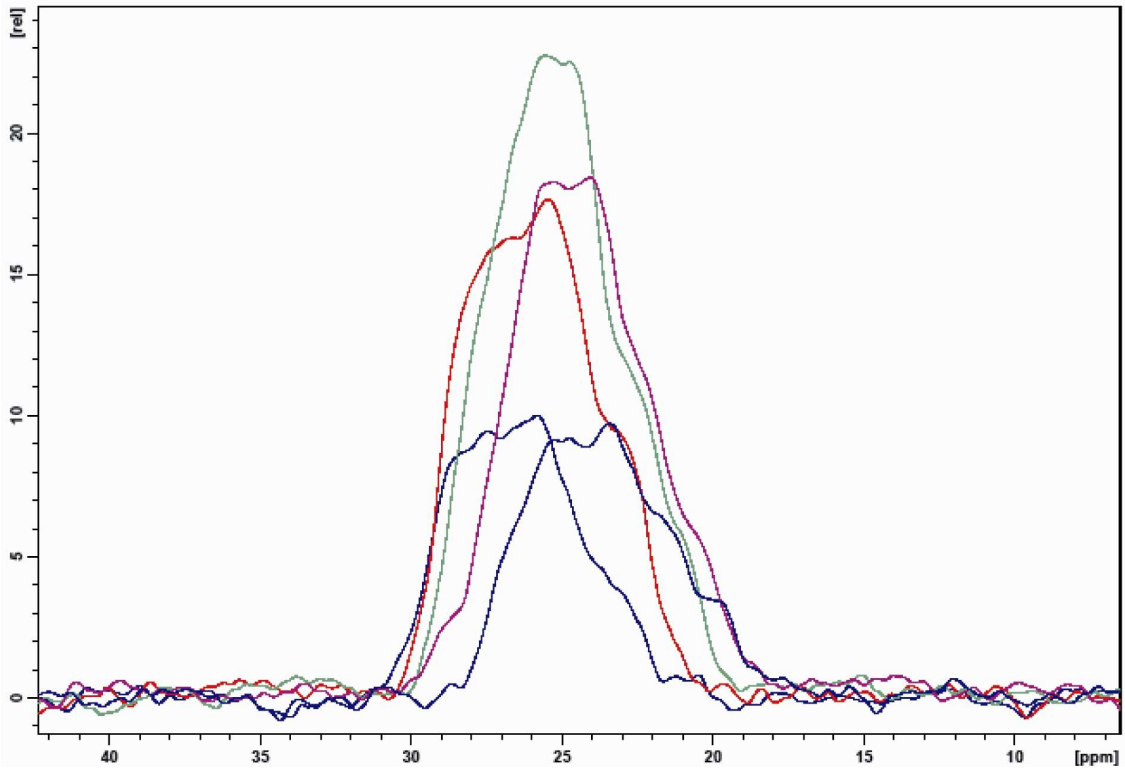

Figure A2: One-dimensional slices of the ^{11}B MQMAS spectrum of compound **21**. These slices are running through the lineshape observed in the isotropic dimension along the F1 axis. Each slice running through the lineshape observed along the isotropic dimension is shown in a different colour. Note that there appears to be a slight change in C_Q values between each slice.

References

1. Haeberlen, U. In *High Resolution NMR in Solids: Selective Averaging,* Advances in Magnetic Resonance, Supplement 1; Waugh, J. S., Ed.; Academic Press: New York, 1976.

2. Mehring, M. *Principles of High Resolution NMR in Solids*, 2nd ed.; Springer-Verlag: Berlin, 1983.

3. Mason, J. *Solid State Nucl. Magn. Reson.* **1993**, *2*, 285-288.

4. Ramsey, N. F. *Phys. Rev.* **1950**, *77,* 567.

5. Ramsey, N. F. *Phys. Rev.* **1950**, *78,* 699-703.

6. Grutzner, J. B. In *Recent Advances in Organic NMR Spectroscopy,* Lambert, J. B.; Rittner, R., Eds., Norell Press: Landisville, 1987; chapter 2.

7. Cohen, M. H.; Reif, F. In *Solid State Physics*, Volume 5; Seitz, F. and Turnbull, D. Eds.; Academic Press: New York, 1957; p. 321.

8. Samoson, A., Lippmaa, E., *J. Magn. Reson.,* **1989**, 84, 410-416.

9. Adiga, S.; Aebi, D.; Bryce, D. L. *Can. J. Chem.* **2007**, *85*, 496-505.

10. Bryce, D. L. Tensor Interplay In *NMR Crystallography*; Harris, R. K., Wasylishen, R. E., Duer, M. J., Eds.; John Wiley and Sons Ltd.: Chichester, 2009; pp 289-301.

11. Amoureux, J. P.; Fernandez, C.; Granger, P. In *Multinuclear Magnetic Resonance in Liquids and Solids – Chemical Applications*, NATO ASI Series C, Vol. 322; Granger, P.; Harris, R. K., Eds.; Kluwer Academic Publishers: Dordrecht, 1990; chapter XXII.

12. Harris, R. K.; Becker, E. D.; Cabral de Menezes, S. M.; Granger, P.; Hoffman, R. E.; Zilm, K. W. *Pure Appl. Chem.* **2008**, *80,* 59-84.

13. Pyykkö, P. *Mol. Phys.* **2008**, *106,* 1965-1974.

14. Nöth, H.; Wrackmeyer, B. *Nuclear Magnetic Resonance Spectroscopy of Boron Compounds*, Springer-Verlag: Berlin, 1978.

15. Andrew, E. R.; Bradbury, A.; Eades, R. G. *Nature (London)* **1959**, *182*, 1659-1660.

16. Andrew, E. R.; Bradbury, A.; Eades, R. G. *Nature (London)* **1959**, *182*, 1802-1803.

17. Lowe, I. J. *Phys. Rev. Lett.* **1959**, *2*, 285-287.

18. Andrew, E. R.; Newing, R. A. *Proc. Phys. Soc.* **1958**, *72*, 959-972.

19. Andrew, E. R. In *Encyclopedia of Nuclear Magnetic Resonance*; Grant, D. M. and Harris, R. K., Eds.; John Wiley & Sons: Chinchester, UK, 1996; p. 5891.

20. Andrew, E. R. *Phil. Trans. R. Soc. Lond.* **1981**, *A299*, 505-520.

21. Abraham, R.; Marsden, J. E.; and Ratiu, T. S. In *Manifolds, Tensor Analysis, and Applications*, 2nd ed.; Springer-Verlag: New York, 1991.

22. Purcell, E. M.; Torrey, H. C.; Pound, R. V. *Phys. Rev.* **1946**, *69,* 37-38.

23. Hall, D. G. *Boronic Acids. Preparation and Applications in Organic Synthesis and Medicine*, Wiley-VCH: Weinheim, 2005.

24. Sakai, M.; Hayashi, H.; Miyaura, N. *Organometallics* **1997**, *16,* 4229-4231.

25. Takaya, Y.; Ogasawara, M.; Hayashi, T.; Sakai, M.; Miyaura, N. *J. Am. Chem. Soc.* **1998**, *120*, 5579–5580.

26. Kettner, C.; Mersinger, L.; Knabb, R. *J. Biol. Chem.* **1990**, *265*, 18289-18297.

27. Spencer, J.; Burd, A. P.; Goodwin, C. A.; Mérette, S. A. M.; Scully, M. F.; Adatia, T.; Deadman, J. J. *Tetrahedron* **2002**, *58*, 1551-1556.

28. Strynadka, N. C. J.; Adachi, H.; Jensen, S. E.; Johns, K.; Sielecki, A.; Betzel, C.; Sutoh, K.; James, M. N. G. *Nature* **1992**, *359*, 700-705.

29. Flentke, G. R.; Munoz, E.; Huber, B. T.; Plaut, A. G.; Kettner, C. A.; Bachovchin, W. W. *Proc. Natl. Acad. Sci. U. S. A.* **1991**, *88*, 1556-1559.

30. Dunsdon, R. M.; Greening, J. R.; Jones, P. S.; Jordan, S.; Wilson, F. X. *Bioorg. Med. Chem. Lett.* **2000**, *10*, 1577-1579.

31. Bukhtiyarova, M.; Rizzo, C. J.; Kettner, C. A.; Korant, B. D.; Scarnati, H. T.; King, R. W. *Antiviral Chem. Chemother.* **2002**, *12*, 367-373.

32. Hiratake, J.; Oda, J. *Biosci. Biotech. Biochem.* **1997**, *61*, 211-218.

33. Yang, W.; Gao, X.; Wang, B. *Med. Res. Rev.* **2003**, *23*, 346-368.

34. Miyaura, N.; Suzuki, A. *Chem. Rev.* **1995**, *95*, 2457-2483.

35. Suzuki, A. *J. Organomet. Chem.* **1999**, *576*, 147-168.

36. Al-Zoubi, R. M.; Marion, O.; Hall, D. G. *Angew. Chem. Int. Ed.* **2008**, *47*, 2876-2879.

37. Côté, A. P.; Benin, A. I.; Ockwig, N. W.; O'Keeffe, M.; Matzger, A. J.; Yaghi, O. M. *Science* **2005**, *310*, 1166-1170.

38. El-Kaderi, H. M.; Hunt, J. R.; Mendoza-Cortés, J. L.; Côté, A. P.; Taylor, R. E.; O'Keeffe, M.; Yaghi, O. M. *Science* **2007**, *316*, 268-272.

39. Rambo, B. M.; Lavigne, J. J. *Chem. Mater.* **2007**, *19*, 3732-3739.

40. Korich, A. L.; Iovine, P. M. *Dalton Trans.* **2010**, *39*, 1423-1431.

41. Adamczyk-Woźniak, A.; Cyrański, M. K.; Jakubczyk, M.; Klimentowska, P.; Koll, A.; Kołodziejczak, J.; Pojmaj, G.; Żubrowska, A.; Żukowska, G. Z.; Sporzyński, A. *J. Phys. Chem. A* **2010**, *114*, 2324-2330.

42. Sweet, W. H.; Javid, M. *J. Neurosurg.* **1952**, *9*, 200-209.

43. Srivastava, R. R.; Kabalka, G. W. *J. Org. Chem.* **1997**, *62*, 8730-8734.

44. Hawthorne, M. F. *Mol. Med. Today* **1998**, *4*, 174-181.

45. Valliant, J. F.; Schaffer, P. *J. Inorg. Biochem.* **2001**, *85*, 43-51.

46. Kennedy, J. D. In *Multinuclear NMR*, Mason, J., Ed., Plenum Press: New York, 1987; chapter 8.

47. Ananthanarayanan, A.; Kothiyal, G. P.; Montagne, L.; Revel, B. *J. Solid State Chem.* **2010**, *183*, 1416-1422.

48. Lee, S. K.; Mibe, K.; Fei, Y.; Cody, G. D.; Mysen, B. O. *J. Phys. Rev. Lett.* **2005**, *94*, 165507.

49. Qiu, D.; Guerry, P.; Ahmed, I.; Pickup, D. M.; Carta, D.; Knowles, J. C.; Smith, M. E., Newport, R. J. *J. Mater. Chem. Phys.* **2008**, *111*, 455-462.

50. Goswami, M.; Kothiyal, G. P.; Montagne, L.; Delevoye, L. *J. Solid State Chem.* **2008**, *181*, 269-275.

51. Ananthanarayanan, A.; Kothiyal, G. P.; Montagne, L.; Revel, B. *J. Solid State Chem.* **2010**, *183*, 120-127.

52. Sehlleier, Y. H.; Verhoeven, A.; Jansen, M. *J. Mater. Chem.* **2007**, *17*, 4316-4319.

53. Gervais, C.; Babonneau, F.; Ruwisch, L.; Hauser, R.; Riedel, R. *J. Can. J. Chem.* **2003**, *81*, 1359-1369.

54. Gervais, C.; Framery, E.; Duriez, C.; Maquet, J.; Vaultier, M.; Babonneau, F. *J. Eur. Ceram. Soc.* **2005**, *25*, 129-135.

55. Gervais, C.; Babonneau, F. *J. Organomet. Chem.* **2002**, *657*, 75-82.

56. Marchetti, P. S.; Kwon, D.; Schmidt, W. R.; Interrante, L. V.; Maciel, G. E. *Chem. Mater.* **1991**, *3*, 482-486.

57. Kameda, T.; Ishii, T.; Matsunaga, T.; Ashida, J. *Anal. Sci.* **2006**, *22*, 321-323.

58. Bryce, D. L.; Wasylishen, R. E.; Gee, M. *J. Phys. Chem. A* **2001**, *105*, 3633-3640.

59. Zhdankin, V. V.; Persichini III, P. J.; Zhang, L.; Fix, S.; Kiprof, P. *Tetrahedron Lett.* **1999**, *40*, 6705-6708.

60. Maly, K. E.; Malek, N.; Fournier, J.-H.; Rodríguez-Cuamatzi, P.; Maris, T.; Wuest, J. D. *Pure Appl. Chem.* **2006**, *78*, 1305-1321.

61. Maly, K. E.; Maris, T.; Wuest, J. D. *CrystEngComm* **2006**, *8*, 33-35.

62. Zhang, J.; Cai, S.; Chen, Z. *Magn. Reson. Chem.* **2009**, *47*, 629-634.

63. Hayashi, S.; Hayamizu, K. *Bull. Chem. Soc. Jpn.* **1989**, *62*, 2429-2430.

64. Freude, D.; Haase, J. *NMR Basic Princ. Prog.* **1993**, *29*, 1.

65. Hahn, E. L. *Phys. Rev.* **1950**, *80*, 580-594.

66. Massiot, D.; Fayon, F.; Capron, M.; King, I.; Le Calvé, S.; Alonso, B.; Durand, J.-O.; Bujoli, B.; Gan, Z.; Hoatson, G. *Magn. Reson. Chem.* **2002**, *40*, 70-76.

67. Eichele, K.; Wasylishen, R.E. *WSOLIDS NMR Simulation Package, version 1.17.30*, Dalhousie University: Halifax, 2001.

68. Alderman, D. W.; Solum, M. S.; Grant, D. M. *J. Chem. Phys.* **1986**, *84*, 3717-3725.

69. Becke, A. D. *J. Chem. Phys.* **1993**, *98*, 5648-5652.

70. Rettig, S. J.; Trotter, J. *Can. J. Chem.* **1977**, *55*, 3071-3075.

71. Frisch, M. J.; Trucks, G. W.; Schlegel, H. B.; Scuseria, G. E.; Robb, M. A.; Cheeseman, J. R.; Montgomery, Jr., J. A.; Vreven, T.; Kudin, K. N.; Burant, J. C.; Millam, J. M.; Iyengar, S. S.; Tomasi, J.; Barone, V.; Mennucci, B.; Cossi, M.; Scalmani, G.; Rega, N.; Petersson, G. A.; Nakatsuji, H.; Hada, M.; Ehara, M.; Toyota, K.; Fukuda, R.; Hasegawa, J.; Ishida, M.; Nakajima, T.; Honda, Y.; Kitao, O.; Nakai, H.; Klene, M.; Li, X.; Knox, J. E.; Hratchian, H. P.; Cross, J. B.; Bakken, V.; Adamo, C.; Jaramillo, J.; Gomperts, R.; Stratmann, R. E.; Yazyev, O.; Austin, A. J.; Cammi, R.; Pomelli, C.; Ochterski, J. W.; Ayala, P. Y.; Morokuma, K.; Voth, G.

A.; Salvador, P.; Dannenberg, J. J.; Zakrzewski, V. G.; Dapprich, S.; Daniels, A. D.; Strain, M. C.; Farkas, O.; Malick, D. K.; Rabuck, A. D.; Raghavachari, K.; Foresman, J. B.; Ortiz, J. V.; Cui, Q.; Baboul, A. G.; Clifford, S.; Cioslowski, J.; Stefanov, B. B.; Liu, G.; Liashenko, A.; Piskorz, P.; Komaromi, I.; Martin, R. L.; Fox, D. J.; Keith, T.; Al-Laham, M. A.; Peng, C. Y.; Nanayakkara, A.; Challacombe, M.; Gill, P. M. W.; Johnson, B.; Chen, W.; Wong, M. W.; Gonzalez, C.; Pople, J. A. *Gaussian 03*, rev. B.03 and C.02; Gaussian, Inc.: Wallingford, CT, 2004.

72. te Velde, G.; Bickelhaupt, F. M.; Baerends, E. J.; Fonseca Guerra, C.; van Gisbergen, S. J. A.; Snijders, J. G.; Ziegler, T. *J. Comp. Chem*, **2001**, *22*, 931-967.

73. Mills, I.; Cvitaš, T.; Homann, K.; Kallay, N.; Kuchitsu, K. *Quantities, Units and Symbols in Physical Chemistry*, 2nd ed.; International Union of Pure and Applied Chemistry Physical Chemistry Division, Blackwell Science: Oxford, 1993.

74. Siegel, R.; Nakashima, T. T.; Wasylishen, R. E. *J. Phys. Chem. B* **2004**, *108*, 2218-2226.

75. Schurko, R. W.; Hung, I.; Widdifield, C. W. *Chem. Phys. Lett.* **2003**, *379*, 1-10.

76. Siegel, R.; Nakashima, T. T.; Wasylishen, R. E. *Concepts Magn. Reson. Part A* **2005**, *26A*, 62-77.

77. Siegel, R.; Nakashima, T. T.; Wasylishen, R. E. *Concepts Magn. Reson. Part A* **2005,** *26A*, 47-61.

78. Ivanov, D.; Redfield, A. G. *J. Magn. Reson.* **2004**, *166*, 19-27.

79. Larsen, F. H.; Jakobsen, H. J.; Ellis, P. D.; Nielsen, N. C. *J. Phys. Chem. A* **1997**, *101*, 8597-8606.

80. Côté, A. P.; Benin, A. I.; Ockwig, N. W.; O'Keeffe, M.; Matzger, A. J.; Yaghi, O. M. *Science* **2005**, *310*, 1166-1170.

81. Thomas, K. M. *Dalton Trans.* **2009**, *9*, 1487-1505.

82. Srepusharawoot, P.; Scheicher, R. H.; Araújo, M.; Blomqvist, A.; Pinsook, U.; Ahuja, R. *J. Phys. Chem. C* **2009**, *113*, 8498-8504.

83. Seo, J. S.; Whang, D.; Lee, H.; Jun, S. I.; Oh, J.; Jeon, Y. J.; Kim, K. *Nature* **2000**, *404*, 982-986.

84. Autschbach, J.; Zheng, S.; Schurko, R. W. *Concepts Magn. Reson. Part A* **2010,** *36A(2)*, 84-126.

85. Sheldrick, G. M. *Acta Crystallogr. Sect. A: Found Crystallogr.* **2008**, *64*, 112-122.